2021

Detection of Circulating Biomarkers with Gold-Based Nanoparticles and Optical Spectroscopy

Raymond E. Wilson

DETECTION OF CIRCULATING BIOMARKERS WITH GOLD-BASED NANOPARTICLES AND OPTICAL SPECTROSCOPY

by

Raymond Edward Wilson, Jr.

A Dissertation

Submitted in Partial Fulfillment of the

Requirements for the Degree of

Doctor of Philosophy

Major: Chemistry

The University of Memphis

December 2021

DEDICATION

This dissertation is dedicated to my wife, Thang Pham. She has been a constant support in my life for over a decade. Thang's discipline and compassion have always been an inspiration to me, and I strive to be like her in these ways. She has pushed me throughout graduate school and encouraged me to overcome every obstacle. I would not be in a position to be completing my graduate program without her by my side.

ACKNOWLEDGEMENT

Firstly, I would like to express my utmost gratitude for my advisor, Dr. Xiaohua Huang. I first met Dr. Huang in 2010, when I was an undergraduate research volunteer in her lab. I became immediately fascinated by the work she was doing, and made an effort to understand the principles guiding her research. After making the decision to begin graduate school at the University of Memphis, I had no doubt I would join her lab and begin work right away. During my time in graduate school, Dr. Huang has taught me so much not only about how to approach science and experimentation, but also how to communicate, how to treat others, and so much more. I am incredibly thankful for her patience and support throughout my graduate program.

Secondly, I would like to thank my committee members for their enduring support throughout my graduate school experience. Each one has a unique set of expertise that has given me a great deal of insight into my research and allowed me to have a multidisciplinary perspective of my work. To this end, I would like to thank Dr. Paul Simone, Dr. Yongmei Wang, Dr. Tomoko Fujiwara, and Dr. Thang Hoang, for the time and effort put forth in guiding me through my graduate program.

Thirdly, I would like to show my appreciation for my fellow lab members. This includes Dr. Ryan T. O'Connor and Dr. Elyahb A. Kwizera, both of whom served as mentors to me and instructed me in countless matters pertaining to our research. I would like to thank Dr. Vojtěch Vinduška and Zechariah J. Avello, who began graduate school at the same time as me, and were a constant arm of support for me. I would also like to thank Kristopher D. Amrhein, Alberto Rodriguez, and Mitchell L. Taylor for their consistent help and friendship which as been a great aid.

Lastly, I would like to thank the Department of Chemistry at the University of Memphis for their tremendous support of their graduate students. I am greatly appreciative of the resources and time they have invested in me. Their support has allowed me to pursue my graduate studies uninterrupted by financial or other stress. To all of the faculty, staff, and students of this department, thank you for your continual contribution in making this department function.

PREFACE

The writing of this dissertation is based on three journal articles:

Chapter 1 is designed to give an overview of the role of gold nanoparticles in the biomedical field with an emphasis on biological detection. Some of their important physical and chemical qualities are discussed as a basis for their application to biodetection. Further, several important examples of their use in biodetection are presented for consideration.

Chapter 2 is devoted to an article that was published in the ACS Journal of Applied Materials and Interfaces: "Wilson Jr, R.E., O'Connor, R., Gallops, C.E., Kwizera, E.A., Noroozi, B., Morshed, B.I., Wang, Y. and Huang, X. Immunomagnetic capture and multiplexed surface marker detection of circulating tumor cells with magnetic multicolor surface-enhanced Raman scattering nanotags. ACS Applied Materials & Interfaces 2020, 12(42), 47220-47232." The tables, figures, schematics, and references from this article have been reformatted and renumbered to agree with this document. The references and style of this chapter fit the standards prescribed by the Journal of Applied Materials and Interfaces.

Chapter 3 is based on an article "Optimizing Cellular Binding of Ligand-Conjugated Gold Nanoparticles" that is currently being prepared by its authors.

Chapter 4 is based on an article "Development of a Gold Nanoparticle-Enhanced Enzyme-Linked Immunosorbent Assay for Detection of SARS-CoV-2 Spike Protein Antibodies" which is currently in preparation by its authors.

ABSTRACT

Raymond Edward Wilson, Jr. The University of Memphis. December 2021. Detection of Circulating Biomarkers with Gold-Based Nanoparticles and Optical Spectroscopy. Major Professor: Prof. Xiaohua Huang

Gold nanoparticles (AuNPs) are remarkable agents for biological detection due to their facile surface modification, optical enhancement, and biocompatibility. These characteristics encourage the development of new methods for biological detection. Of particular interest, in the field of biological detection, is the ability to detect, quantify, and characterize circulating biomarkers. Circulating biomarkers include classes of biological analytes such as cells, extracellular vesicles, proteins, DNAs, and RNAs. The ability to detect and characterize such analytes gives clinicians two significant advantages in diagnosing diseases. One advantage is diagnosis by means of a non-invasive biopsy, as circulating biomarkers may be isolated and detected from a patient's blood. A second major advantage is earlier detection than what is provided by a traditional tissue biopsy. For example, many cancers go undetected until the disease has metastasized, significantly limiting chances of a successful treatment outcome. However, biomarkers that reflect the molecular contents of the tumor are being released into the bloodstream, even in early stages of tumorigenesis. Hence, the ability to detect and characterize such biomarkers would lead to earlier detection and potentially a better treatment outcome. In this dissertation, we explore the unique properties of AuNPs that enable their use as agents for circulating biomarker detections. In addition, we highlight recent methods utilizing AuNPs for biological detection. Next, we report on our method for the isolation, detection and characterization of circulating tumor cells using core-shell iron oxide-gold nanoparticles (IO-Au NPs). This method combines magnetic capture, microfluidics, fluorescence and surface enhanced Raman scattering (SERS) spectroscopy for detection and multicolor characterization of

circulating tumor cells. Additionally, we report on a study to optimize the cellular binding of ligand-conjugated AuNPs. In this study we undertake a rigorous effort to design ligand-conjugated AuNPs that feature high degrees of specificity and reproducibility. Finally, we demonstrate a method of AuNP-enhanced enzyme-linked immunosorbent assay (ELISA) designed for detection of antibodies to the spike protein of severe acute respiratory syndrome coronavirus 2 (SARS-CoV-2). Our enhanced ELISA method gives an approximately 100-fold increase in sensitivity over traditional ELISA methods, and also shares the agility of traditional ELISA that allows detection of a multitude of analytes.

TABLE OF CONTENT

LIST OF FIGURES

LIST OF SYMBOLS AND ABBREVIATIONS

≈	Approximately
=	Equal to
<	Less than
>	Greater than
°C	Degrees Celsius
µg	Microgram
µL	Microliter
µM	Micromolar
λ	Wavelength
Ab	Antibody
ACE2	Angiotensin-converting enzyme 2
AFM	Atomic force microscopy
Ag	Silver
$AgNO_3$	Silver nitrate
AgNP	Silver nanoparticle
Au	Gold
$AuCl_4^-$	Chloroaurate ion
AuNP	Gold nanoparticle
AuNR	Gold nanorod
BC	Breast cancer
BPL	*beta*-Propiolactone
BSA	Bovine serum albumin

CLS	Classical least squares
COVID-19	Coronavirus disease 2019
CTAB	Hexadecyltrimethylammonium chloride
CTC	Circulating tumor cell
Da	Dalton
DLS	Dynamic light scattering
DMEM	Dulbecco’s Modified Eagle Medium
DNA	Deoxyribonucleic acid
DPBS	Dulbecco's phosphate-buffered saline
EGFR	Epidermal growth factor receptor
ELISA	Enzyme-linked immunosorbent assay
EMT	Epithelial to mesenchymal transition
EpCAM	Epithelial cell adhesion molecule
EPR	Enhanced permeability and retention
FBS	Fetal bovine serum
FL	Fluorescence
H_2SO_4	Sulfuric acid
HER2	Human epidermal growth factor receptor 2
HIV-1	Human immunodeficiency virus type 1
HRP	Horseradish peroxidase
HS-PEG-Ab	Antibody-linked polyethylene glycol thiols
HS-PEG-NHS	Thiol- polyethylene glycol- N-hydroxysuccinimide esters
IGF-1R	Insulin-like growth factor 1 receptor

IgG	Immunoglobulin G
IgM	Immunoglobulin M
IL-1β	Interleukin 1 beta
IO-Au NP	Iron oxide-gold nanoparticle
IO NP	Iron oxide nanoparticle
LOD	Limit of detection
LSPR	Localized surface plasmon resonance
M	Molarity
MERS-CoV	Middle East respiratory syndrome–related coronavirus
mg	Milligram
min	Minute
mL	Milliliter
mM	Millimolar
mPEG	Monomethoxypolyethylene glycol
mV	Millivolt
mW	Milliwatt
MW	Molecular weight
MWCO	Molecular weight cut-off
NH_2OH	Hydroxylamine
nm	Nanometer
NP	Nanoparticle
NPC	Nanopopcorn
NTA	Nanoparticle tracking analysis

PBS	Phosphate-buffered saline
PBST	Phosphate-buffered saline-tween
PEG	Polyethylene glycol
PEI	Polyethyleneimine
pI	Isoelectric point
RMSE	Root-mean-square error
ROS	Reactive oxygen species
RNA	Ribonucleic acid
RNS	Reactive nitrogen species
RT	Room temperature
RT-PCR	Reverse transcription polymerase chain reaction
SA	Streptavidin
SARS-CoV	Severe acute respiratory syndrome coronavirus 1
SARS-CoV-2	Severe acute respiratory syndrome coronavirus 2
SD	Standard deviation
SERS	Surface enhanced Raman scattering
SPR	Surface plasmon resonance
TEM	Transmission electron microscopy
TMB	3,3',5,5'-Tetramethylbenzidine
TNFα	Tumor necrosis factor alpha
TOAB	Tetraoctylammonium bromide
uv-vis	Ultraviolet-visible
vis-NIR	Visible-near infrared

WBC	White blood cell

Chapter 1. INTRODUCTION

1. History, Synthesis, and Properties of Gold Nanoparticles

1.1 History of Gold Nanoparticles

Gold is a rare and precious metal often associated with coins, jewelry, and other works of art. It is highly stable in its bulk form and, unlike some metals, is not susceptible to oxidation or deterioration, leading to its coveted use in sculptures, Olympic medals, and more.[2] Gold nanoparticles (AuNPs) are simply particles composed of gold with an effective diameter in the range of 1 – 100 nm. Uses for gold colloidal nanoparticles have been around for centuries. In one of the earliest known examples, the Lycurgus cup was created in the 4th century CE using AuNPs.[3] The Lycurgus cup is an ancient display showcasing AuNPs' unique optical properties in the form of dichroic glass, which appears red by transmitted light and appears green by reflected light.[4] Beyond their aesthetic merit, AuNPs are of great practical value due to properties unique to their size and composition. Scientific inquiry into the nature of AuNPs dates back to at least the 1850s, when Michael Faraday documented the synthesis of colloidal AuNPs.[5] Several years later, Gustav Mie made an important theoretical discovery when, in 1908, he presented a solution for Maxwell's equations of electromagnetism which accurately described the absorption and scattering spectra of spherical gold nanoparticles.[6-9] Advances in controlling the synthesis of gold nanoparticles continued with the work of Turkevich *et al.* in 1951 and Frens who, in 1973, reproducibly synthesized monodisperse spherical gold nanoparticles by using Turkevich's citrate-mediated growth procedure.[10,11]

In the latter part of the 20th century, many important discoveries paved the way for gold nanoparticles' use in medical diagnostics. One such discovery was that of surface-enhanced

Raman scattering (SERS), which occurred in 1973 when Fleischmann *et al.* observed the enhancement of the Raman spectrum of pyridine adsorbed onto a silver electrode.[12] Important efforts soon followed by Van Duyne and Jeanmaire, and separately by Albrecht and Creighton, to explain the mechanism seen in surface-enhanced Raman scattering.[13,14] In 1997, Nie and Emory published groundbreaking results purporting single molecule and single particle detection using silver nanoparticles (AgNPs) and SERS.[15] This important work demonstrated the potential of metallic nanoparticles for aiding detection of rare analytes. Near this time, AuNPs entered the field of biosensing in many different capacities.

One of the early studies pointing to AuNPs' potential for novel biological detection occurred in 1996, when it was reported that the reversible aggregation of small oligonucleotide-bound AuNPs could be observed while complementary target deoxyribonucleic acids (DNA) were present.[16] Furthermore, these oligonucleotide-bound AuNP aggregates exhibited extraordinarily sharp melting profiles. Both of these observations were results of unique properties of AuNPs; namely, a high surface-to-volume ratio and uncommon optical activities. This work spawned a flurry of research into designing nanomaterials for biological diagnostics and therapeutics.[17] (Figure 1.1) Further developments in the 21st century include the important work of Hirsch *et al.*, who documented the detection of proteins in serum and whole blood using antibody-bound gold nanoshells.[18] They were able to differentiate the extinction spectra of free gold nanoshells from the spectra of gold nanoshells bound to target proteins, reporting an analyte sensitivity below 1 ng/mL which is comparable to ELISA. Another important work occurred in 2006, when Huang *et al.* demonstrated the therapeutic value of AuNPs in addition to the diagnostic potential.[19] In this report, it is shown that anti-epidermal growth factor receptor (EGFR) conjugated to gold nanorods (AuNRs) express a high affinity to certain malignant-type

cells. Furthermore, once the AuNRs were bound to the malignant cells, they readily destroyed the cancer cells when shown by a near-infrared (NIR) laser, effectively converting the light into heat.[20] These works highlight the important advancements made to create a critical role for AuNPs in the biomedical field.

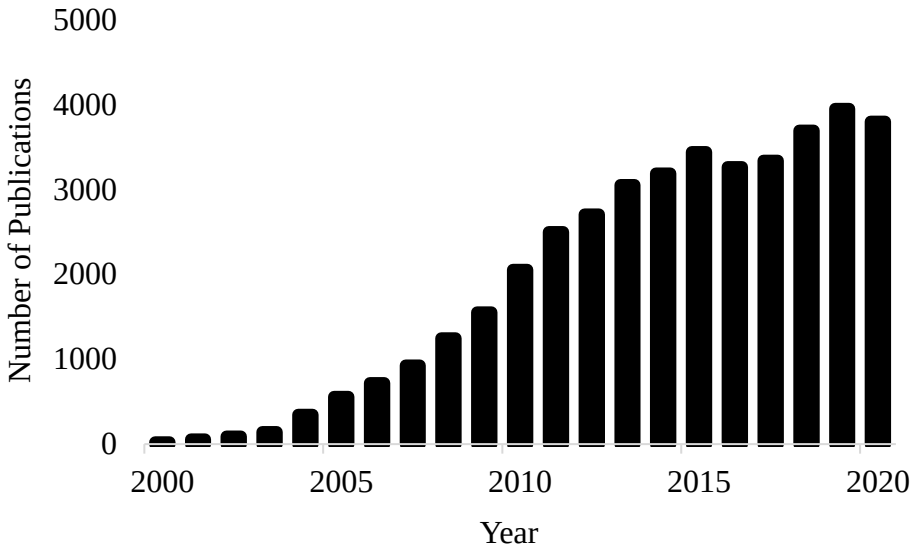

Figure 1.1. The significant growth of research publications regarding AuNPs in the biomedical sector in the 21st century.[1] Publication numbers are generated by a PubMed keyword search of "gold nanoparticles", which retrieves articles from the MEDLINE database cataloging works published in the areas of life science and biomedicine.

1.2 Synthesis Methods for Various Types of Gold Nanoparticles

In the previous section, it was mentioned that Faraday was one of the first scientists to document the synthesis of AuNPs.[5] In his work, he recorded the formation of a red solution of colloidal AuNPs upon the reduction of a gold salt by phosphorus in the presence of carbon disulfide. Even to this day, many protocols for synthesizing AuNPs follow a variation of Faraday's method, whereby a gold salt is reduced in the presence of a capping agent which helps to prevent the aggregation of particles.[2] The standard modern method for generating colloidal

gold nanospheres (AuNS) is performed by the reduction of the tetrachlorate ion ($AuCl_4^-$) by sodium citrate. In this reaction, nanoclusters of 5 nm diameter begin to form and branch into a network of nanowires.[21] As the reaction proceeds, the diameter of the nanowires begins to increase as more gold is deposited. Eventually the nanowires break into smaller segments which ultimately give way to a spherical nanoparticle. This reaction may be used to reliably produce colloidal AuNPs between 5 and 150 nm in diameter by controlling the sodium citrate to gold ion ratio, the reaction pH, and the solvent.[11,22,23] Gold nanospheres are the most basic synthetic shape of gold nanoparticles, but much effort has gone into designing AuNPs with various sizes and shapes.

One of the first shapes to be designed beyond the spherical gold nanoparticle was that of the gold nanorod (AuNR).[24,25] In one of their first iterations, AuNRs were generated by electrochemically depositing gold into the pores of microporous alumina membranes and dissolving the template membrane. This is an example of a hard template-directed method for AuNR synthesis, which may be of interest for generating high-purity AuNRs for the study or effect of higher-order surface plasmon resonances (SPR).[26] Another important work in the development of synthetic AuNRs was the discovery that upon electrochemical oxidation/reduction of a gold plate anode and platinum plate cathode in the presence of the cationic surfactant, hexadecyltrimethyl-ammonium bromide (CTAB), and a rod-inducing cosurfactant, tetraoctylammonium bromide (TOAB), AuNRs approximately 10 nm in diameter of varying aspect ratios could be discerned.[27] In this work, it was shown that two unique SPR modes occur for AuNRs due to the presence of a short axis (transverse mode) and long axis (longitudinal mode) of polarization. In the early 21st century, very important developments in the discovery of methods for the colloidal synthesis of AuNRs occurred.[28,29] These studies resulted

in a seed-mediated AuNR growth method, whereby small gold seeds are first generated upon the reduction of $AuCl_4^-$ by borohydride in the presence of CTAB, and later planted into a growth solution consisting of $AuCl_4^-$ reduced by ascorbic acid, silver nitrate ($AgNO_3$), and CTAB. The resulting particles are AuNRs with a rod diameter of 10 – 20 nm and an adjustable rod-length up to 300 nm. Parameters such as the gold seed/gold salt ratio and the added concentration of ion impurities may be utilized to vary the aspect ratio in this method. Figure 1.2 demonstrates how the aspect ratio, and thus the longitudinal SPR band, may be varied upon adding different amounts of $AgNO_3$. These particles, like other AuNPs, are highly desirable for their tunable shape-dependent optical properties, leading to their use in a variety of biomedical applications.[30]

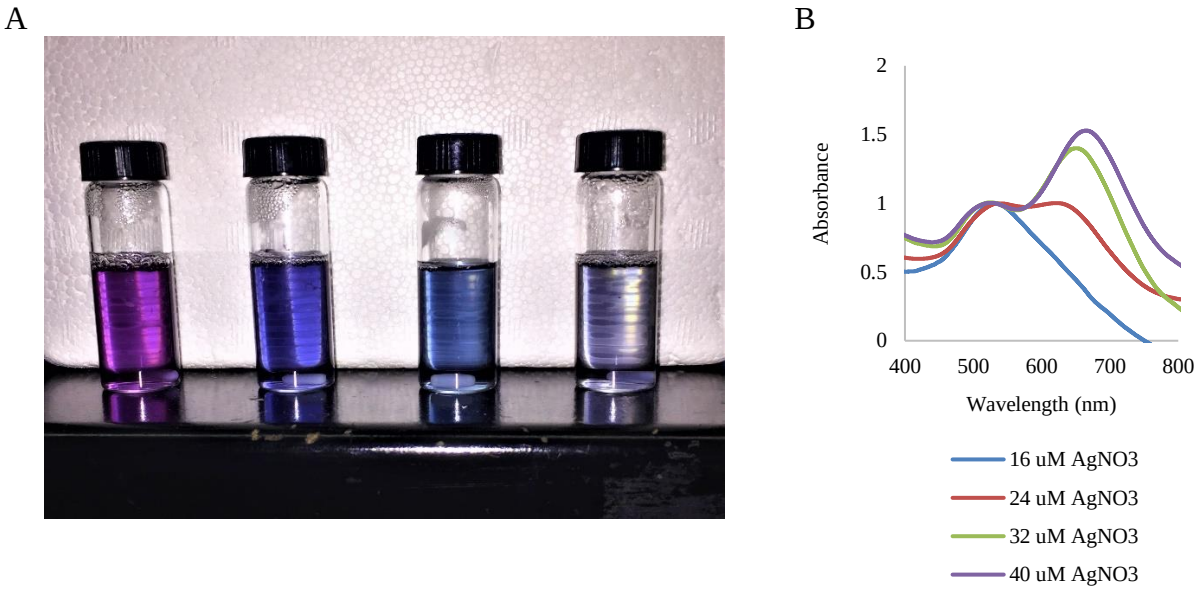

Figure 1.2. Demonstrating the tunable optical properties of gold nanorods. A) Gold nanorod solutions with increasing concentrations of silver nitrate from left to right. B) UV-vis absorbance spectra of gold nanorod solutions with varying concentrations of silver nitrate indicating the controlled adjustment of the longitudinal surface plasmon band.

AuNPs may be formed in a variety of geometries including gold-silver nanocages, hollow gold nanoshells, gold nanocubes, gold nanoprisms, and an assortment of other shapes. [31-34] Furthermore, AuNPs may be combined with another element or molecule for multiplex

nanoparticles. A common platform to deliver this multiplex approach is that of a core-shell nanoparticle, in which the core of this particle is comprised of one substance, and the shell is comprised of another. Magnetic-optical core-shell nanoparticles are a particularly useful type of core-shell particle as they utilize a magnetic core, typically composed of cobalt or iron or a compound thereof, and a plasmonic shell, usually composed of silver, gold, or platinum.[35] This class of particles has many biomedical applications from magnetic resonance imaging to photothermal therapy.[36-38] A popular core-shell composition consists of an iron oxide nanoparticle (IO NP) core inside of a gold shell. This is due to the straightforward methods for synthesis of IO NPs, as well as the tunable optical properties and biocompatibility characteristic of AuNPs. Core-shell IO-Au NPs may be synthesized by a direct deposition method where IO NPs are first prepared through the coprecipitation of a ferric chloride and ferrous chloride mixture under basic conditions. This is followed by the reduction of chloroauric acid by sodium citrate in the presence of IO NPs at boiling temperature.[39-41] In addition to direct deposition synthesis methods, IO-Au NPs may be created by gold-seeded growth methods, where electrostatically adsorbed small AuNPs on IO NP surface serve as nucleation sites for the growth of a gold shell. This may be accomplished by attaching small negatively-charged citrate-capped AuNPs to positively-charge polyethyleneimine (PEI)-coated IO NPs. This is followed by the reduction of chloroauric acid by hydroxylamine (NH_2OH) in the presence of gold-seeded IO NPs for gold shell formation.[42] A similar method can be used for the synthesis of anisotropic IO-Au NPs, where citrate-capped AuNPs are electrostatically adsorbed onto the surface of octahedral PEI-coated IO NPs. Next, Au-seeded IO NPs are planted into a growth solution consisting of $HAuCl_4$, CTAB, $AgNO_3$, and ascorbic acid.[43] By controlling the amount of ascorbic acid, as well as the presence or absence of $AgNO_3$, IO-Au NPs may be created into the shapes of spheres,

popcorn, or stars. Anisotropic IO-Au NPs may be desirable for the significant electromagnetic enhancement they yield compared to sphere-shaped nanoparticles.[44] These are a few of many important methods for creating IO-Au NPs, which combine the magnetic separability of magnetic nanoparticles with the optical enhancement and ready surface modification of AuNPs. Based on these properties, IO-Au NPs are a significant asset for the selective isolation and detection of circulating biomarkers.

1.3 Biological, Chemical, and Physical Properties of AuNPs

In the previous sections, it has been noted that AuNPs possess qualities desired for use in the biomedical field. One important criterion for biomedical application of AuNPs is biocompatibility. In one critical study, the potential for cytotoxic and immunogenic effects of lysine- and poly-L-lysine-capped AuNPs was explored through their effect on RAW264.7 macrophage cells.[45] In this case, it was determined that AuNPs are not cytotoxic to cells as measured by a 3-(4,5-dimethylazol-2-yl)-2,5-diphenyl-tetrazolium bromide (MTT) assay, which distinguishes living cells from dead cells.[46] Further, AuNPs do not promote an immunogenic response such as the stress-induced release of tumor necrosis factor alpha (TNFα) and interleukin 1 beta (IL-1β). Interestingly, it was actually shown AuNPs exhibit some therapeutic value by mitigating the production of reactive oxygen species (ROS) and reactive nitrite species (RNS). Of course, AuNPs' biocompatibility must be qualified by a number of parameters including capping agent and particle concentration.[47] Nevertheless, a number of AuNP platforms have been proven nontoxic and are even positioned for commercial use. Aurimune (CYT-6091), a polyethylene glycol-coated AuNP developed by Cytimmune, has shown to be safe for effectively delivering TNFα to tumor sites and is undergoing clinical trials.[48] This highlights AuNPs'

biocompatible character, and distinguishes them from other metallic nanoparticles such as AgNPs which have been shown to be cytotoxic.[49]

In addition to biocompatibility, AuNPs are sought after tools for biomedical application due to their readily modified surface and high surface-to-volume ratio. The high surface area with respect to the particle volume means efficient packing and delivery of therapeutics, probes, and biomolecules to a site of interest.[50-52] AuNPs also express an amendable surface capable of attaching to countless ligands, peptides, oligonucleotides, etc. Although AuNPs may be stabilized by various ligands, dendrimers, polymers, and surfactants, the preferred rout for modification centers around the strong gold-sulphur (Au-S) bond.[53,54] Any functional thiolate may be introduced to AuNPs to modify the particles' behavior. In this manner, AuNPs may be conjugated to antibodies for targeting, polymers for stabilizing, dyes for staining, and many more applications.

AuNPs also demonstrate a phenomenon unique to nanoscale materials known as localized surface plasmon resonance (LSPR). This occurs when a metallic nanoparticle is irradiated by light causing the conducting electrons to oscillate in a coherent fashion.[9] This oscillation is confined to the surface of the nanoparticle and generates an electromagnetic field in the vicinity of the nanoparticle.[55] A direct application of LSPR is for SERS, where a Raman scattering molecule adsorbed to the particle surface experiences a greatly enhanced local field upon excitation of the surface plasmon. Experimentally, it has been shown the Raman scattering signal may be enhanced by up to $10^{14} – 10^{15}$.[15] This remarkable enhancement combined with the sharp, fingerprint-like Raman spectra of Raman scattering molecules leads to methods for extremely sensitive and selective detection of rare analytes.

2. Methods for Functionalization of AuNPs

AuNPs often require modification after synthesis to ensure biocompatibility as well as to designate a function for the particle. The methods for modifying the surface of AuNPs mostly follow the work accomplished in understanding self-assembled monolayers of molecules on a gold surface.[56,57] There are many molecular linkers that may be attached to AuNPs for future functionalization, however, these linkers are generally attached to the particle by the same gold-reactive functional groups such as amines, carboxylates, thiolates, dithiolates, dithiocarbamates, etc.[53,58-60] The selection of a functional group to anchor molecular linkers depends on the application, but generally thiolates are selected for attachment of non-labile applications, while amine and carboxylate functional groups are chosen when labile application is desired. AuNPs are commonly functionalized to incorporate organic dyes, fluorescent dyes, PEG, amino acids, peptides, proteins, DNA, and RNA, or a combination thereof. The versatility to which AuNPs may be functionalized lend their application in a wide variety of biomedical roles.

2.1 PEGylation of AuNPs

For biological applications, it is often imperative that AuNPs be stabilized for protection against high levels of biomolecules and ions. For this purpose, it is standard for AuNPs to contain a layer of PEG on their surface. With this modification, PEGylated AuNPs demonstrate good hydrophilicity for ready diffusion in aqueous media. It has been shown that PEGylated tamoxifen-targeted AuNPs can be used to treat estrogen receptor positive breast cancer cells with enhanced drug potency *in vitro*.[61] Due to the effect of enhanced permeability and retention (EPR) characteristic of stable AuNPs, these PEGylated tamoxifen-targeted AuNPs preferentially accumulate at the tumor site.[62] Furthermore, it has been demonstrated that PEGylated AuNPs show an enhanced circulatory half-life.[63] This is accomplished by the PEG layer shielding the

AuNPs from circulating proteins and opsonins. In another study, PEGylated AuNPs have shown to be valuable X-ray contrast agents, overcoming many limitations common to X-ray imaging such as a short imaging window, renal toxicity, and low contrast in larger patients.[64]

2.2 AuNPs functionalized by Oligonucleotides

Oligonucleotide-modified AuNPs may demonstrate unique affinity for recognizing complementary sequences in DNA segments. In one study it was shown that AuNPs modified by 5'- or 3'-mercaptoalkyloligonucleotides showed excellent stability in the presence of high ionic strength solution (up to 1 M NaCl) and high DNA content (up to 2 mg/mL salmon sperm DNA) without suffering a decrease in function.[65] This work demonstrated the selective and sensitive detection of oligonucleotide (down to 10 femtomoles) upon the color-changing reaction created by the interaction between single-stranded target oligonucleotides and the mercaptoalkyl-oligonucleotide-modified AuNPs. The same group demonstrated the potential of mercapto-alkyloligonucleotide-modified AuNPs for controlled macro-assembly upon interaction of the oligonucleotide-modified AuNPs with complementary DNA.[16] In another study, a unique anchoring group was discovered for modifying AuNPs to incorporate oligonucleotides, and the resulting AuNPs were shown to be much more stable in the presence of reducing agents such as dithiothreitol.[66] The anchoring group consists of a cyclic disulfide derived from the condensation of 4,5-dihydroxy-1,2 dithiane and epiandrosterone and is shown to create much more stable conjugates than those modified by conventional mercaptohexyl groups or an acyclic disulfide group. These are some of the popular methods for creating oligonucleotide-modified AuNPs with applications in nucleotide detection as well as assembly of macro-structures using AuNPs as building blocks.

2.3 AuNPs functionalized by Amino Acids, Peptides, and Proteins

AuNPs may be functionalized by proteins or their building blocks for a variety of applications. AuNPs can be functionalized by amino acid-conjugated thiols to incorporate DNA for gene delivery.[67] By controlling the surface charge density of the amino acid-modified AuNPs, it is possible to optimize the modified AuNPs for controlled binding and subsequent condensation of DNA. For attaching peptides and proteins to AuNPs, there have been a number of covalent and non-covalent strategies deployed. For non-covalent attachment, conjugation of antibodies to citrate-capped AuNPs has been achieved by electrostatic and hydrophobic interaction between the antibody and citrate-capped AuNPs.[68] For this application, optimum binding occurs when the pH of antibody and AuNP solution is maintained at or slightly above the isoelectric point (pI) of the antibody. However, non-covalent attachment of antibodies to AuNPs does express some limitations such as requiring a large concentration of precious antibodies as well as randomized orientation of the adsorbed abtibody.[69] To address these concerns, several methods for covalent attachment of proteins to AuNPs have been developed. One method includes dative binding to form a covalent bond between the protein and the AuNP. This is made possible by the presence of free sulfhydryl groups on the protein.[70] In addition to dative binding, coupling reactions allow covalent attachment of peptides and proteins to functional linkers on the AuNP surface. A commonly employed strategy is the carbodiimide cross-coupling reaction where a carboxylic acid group on a protein is activated by 1-ethyl-3-(-3-dimethylaminopropyl) carbodiimide hydrochloride (EDC) to generate an active *O*-acylisourea intermediate that will further react with a primary amine-containing linker on the AuNP to form a covalent bond.[71] Furthermore, active ester compounds such as *N*-hydroxy-succinimide (NHS) may be used to react with primary amines for covalent amide bond formation.[72]

3. Current Applications of AuNPs in Biological Detection

3.1 Metal Ions

The potential for AuNPs to generate colorimetric reactions lends their application for detection of a wide range of analytes. For metal ions, detection of Pb(II) is critical due to the health disadvantages of lead exposure.[73] One interesting method utilizes AuNPs functionalized by deoxyribozymes to detect Pb(II).[74] Their lead biosensor consists of AuNPs, a deoxyribozyme and its substrate, and 5‘-thio-modified 12-mer DNA. The substrate was designed to hybridize specifically with the DNA on AuNP surface, causing aggregation of the AuNPs and the formation of a blue-colored solution. However, when Pb(II) is present, aggregation is prevented by the hydrolytic cleavage of the substrate catalyzed by the deoxyribozyme, maintaining a red-colored solution. The detection limit for this sensor can be tuned from 100 nM to 200 µM Pb(II).

A similar strategy has been applied to the detection of lithium ions depending on the aggregation of AuNPs to generate a colorimetric reaction.[75] In this method, AuNPs were conjugated to a ligand, 2,9-Dibutyl-1,10-phenanthroline-5,6-aminoethanethiol, which forms a ligand-lithium complex between two ligands and one lithium ion. This complex initiates the aggregation of AuNPs which exhibit a red-shift in their extinction spectra with increasing lithium ion concentration. It was demonstrated this method was effective for detecting lithium ions in the range of 10 to 100 mM.

3.2 Nucleic Acids

Detection of nucleic acids by AuNPs typically rely on the color-changing AuNP aggregation initiated by DNA hybridization as illustrated in previous sections.[16] Another group reports a rapid, label-free AuNP-based DNA detection method capable of detecting specific

sequences and single nucleotide polymorphisms with no detection instrumentation necessary and an assay time reported to be under 10 minutes.[76] For non-colorimetric assays, SPR methods may be employed for ultra-sensitive detection of DNA hybridization.[77] In such a study, oligonucleotide probes were created by the conjugation of AuNPs to thiol-labeled DNA. These oligonucleotide-conjugated AuNPs were then used to identify target DNA attached to a gold surface through a sequence-specific hybridization. The presence of AuNPs were found to drastically amplify the SPR response upon DNA hybridization. The limit of quantitation for this method was calculated to be 10 pM for 24-mer oligonucleotides. Another application for nucleic acid detection by AuNPs incorporates the use of molecular beacons. In one study, AuNPs attached to a DNA with a fluorophore were used to detect specific DNA sequences.[78] The AuNPs in this case served as a scaffold as well as a quencher.

3.3 Proteins

The use of antibody-conjugated AuNPs are a common method for detecting proteins. For example, a gold nanoshell-based aggregation immunoassay was developed for the detection of rabbit IgG in saline, bovine serum, and human whole blood.[18] The assay involved the use of anti-rabbit IgG conjugated to gold nanoshells which were subsequently mixed with different IgG-containing media. The mixture was monitored for changes in the optical extinction at 720 nm, where a proportional decrease in extinction was discovered to occur with increasing interaction between the anti-IgG AuNPs and the analyte IgG. Other approaches include a Raman-based assay with the use of a protein array along with targeted SERS AuNPs.[79] This technique is notable for its use of a protein array to allow multiplex screening of protein-small molecule and protein-protein interactions. And yet another novel approach for detecting proteins with AuNPs employs SERS core-shell AuNPs for the separation and detection of multiple proteins.[80] In this

sandwich-based immunoassay, an anti-IgG-coated silver substrate was used to capture analyte. The samples were then labeled by anti-IgG core-shell AuNPs with a Raman-active molecule affixed for selective detection of analyte. This method reports a remarkable sensitivity of detecting down to 800 ag/mL for mouse IgG and a detection limit of 5 fg/mL for human IgG.

3.4 Viruses

Some of the same methods for detection of nucleic acids and proteins can be applied to viruses. In one study, a method for detection of dengue virus was reported that combines circulating-flow quartz crystal microbalance analysis with DNA-conjugated AuNPs.[81] The modified AuNPs were used to enhance the sensitivity of the quartz crystal microbalance as well as to delegate the specificity of DNA hybridization. This proved to be a very sensitive method detecting down to 2 plaque forming units /ml of dengue virus serotype 2. Another study, developed a method for detecting human immunodeficiency virus type 1 (HIV-1) involving the use of an antibody array for viral P24 antigen capture and antibody-conjugated AuNPs to enhance atomic force microscopy (AFM) measurements.[82] This is yet another very sensitive assay capable of detecting down to 25 fg/mL P24 antigen which is approximately a 1000-fold increase in sensitivity compared to conventional ELISA.

3.5 Circulating Tumor Cells

Cancer cells can be shed from an original tumor and enter the bloodstream through an epithelial-mesenchymal transition (EMT) resulting in circulating tumor cells (CTCs). CTCs highlight the malignant behavior of cancer, playing a major role in metastasis.[83] Detection and molecular characterization of CTCs can facilitate early detection of cancer, help predict treatment response, and provide new therapeutic targets, all through minimally invasive

sampling.[84,85] Previous work has demonstrated the great potential for using multiplex core-shell iron oxide-gold nanoparticles (IO-Au NPs) for CTC capture and detection.[86] These particles combine the excellent specificity of immunomagnetic capture with the sensitivity of surface-enhanced Raman scattering (SERS) spectroscopy. This method showed a limit of detection (LOD) near 1 CTC in 1 mL of blood. It implemented a one-channel capillary tube through which IO-Au NP-labelled cancer cells passed. The cells were captured and concentrated by a series of magnetic fields and analyzed by a portable Raman spectrometer. In addition to sensitivity and reliability, this method offers significant opportunity for screening multiple cancer markers simultaneously.

4. Overview of Chapter Contents

In Chapter 2, we will demonstrate our novel method for using multicolor SERS IO-Au NPs to isolate, detect, and characterize the surface expression of CTCs. In this manner, we are able to simultaneously measure the expression of four separate cancer cell surface markers. First, we demonstrate the quality of our antibody-targeted Raman-tagged IO-AuNPs through darkfield imaging of labeled cancer cells. These functionalized IO-Au NPs show strong affinity and specificity for their antigen, as well as a strong Raman signal as measured in solution. Next, cancer cells are spike into various media, and labelled by our functionalized IO-Au NPs. The labeled cells are then passed through a microfluidic chip in the presence of a magnet for isolation of the cancer cells. Captured cells are subsequently stained by DAPI and anti-CD45/FITC to distinguish cancer cells from potential white blood cells, and probed by our Raman spectrometer to characterize surface marker expression. We conclude that our antibody-targeted Raman-tagged IO-AuNPs combine with the microfluidic device provide a fast, sensitive, multicolor method for detecting CTCs from whole blood.

In Chapter 3, we seek to optimize the cellular binding of streptavidin-conjugated AuNPs by observing the effects of ligand density, labeling media, and stabilizing polymer on the targeted AuNPs. We reproducibly observe the importance of optimizing ligand density by monitoring the size of streptavidin-conjugated AuNPs with varying ratios of coating density. We also observe the impact of common biological blocking agents and detergents at different steps in the cell labeling procedure. Furthermore, we sought to understand the impact of the common AuNP-stabilizing polymer on particle affinity. In conclusion, we developed detailed protocols for achieving optimum *in vitro* cellular binding of ligand-conjugated AuNPs for future applications.

In Chapter 4, we will take a look at how AuNPs may play role in responding the COVID-19 pandemic. We emphasize the importance of serological testing to determine the prevalence of SARS-CoV-2 as well as to monitor vaccine response. Thus, we develop a method for AuNP-enhanced ELISA for detection of SARS-CoV-2 IgG. We use the unique surface properties of AuNPs to deliver anti-IgG/HRP to spike protein IgG. This method shows promising sensitivity with up to a 100-fold enhancement over conventional ELISA. We also demonstrate this method may be deployed for detecting IgG in human blood plasma.

Chapter 2. IMMUNOMAGNETIC CAPTURE AND MULTIPLEXED SURFACE MARKER DETECTION OF CIRCULATING TUMOR CELLS WITH MAGNETIC MULTICOLOR SURFACE-ENHANCED RAMAN SCATERRING NANOTAGS

1. Introduction

Cancer remains a major health problem worldwide.[87] Metastasis is the main cause of death in cancer patients, accounting for 90% of the mortality.[88] Circulating tumor cells (CTCs), the malignant cells of epithelial origin circulating in blood, are the hallmark of metastasis.[89–91] Their detection and analysis can provide a powerful tool in the clinic for the diagnosis of metastasis at an early stage, prognosis of cancer patients, assessment of tumor stage, monitoring of therapeutic response, and ultimately helping the optimization of personalized treatment.[92-95]

CTC analysis, however, is very challenging because CTCs are rare events; approximately one to few CTCs were found to be mixed with about 10 million white blood cells (WBCs) and 5 billion red blood cells in 1 ml of blood of cancer patients.[92] To accomplish reliable results, CTC analysis generally requires a combination of enrichment and detection methods. During the last 2 decades, a variety of techniques have been developed for CTC isolation and detection,[96,97] including some commercialized products such as EPISPOT, AdnaTest, and CellSearch, the only technique that has been approved by the U.S. Food and Drug Administration (FDA) for clinical applications.[98–100]

However, most techniques can only detect CTCs of one specific population such as epithelial cell adhesion molecule (EpCAM)-positive CTCs.[101] It is known that CTCs are a heterogenous population. EpCAM is the most common marker for CTC recognition. However, EpCAM down-regulation has also been correlated with CTCs in peripheral blood.[102] Thus, CTCs

with low or no EpCAM expression go undetected leading to false negatives. A combination of EpCAM and other cancer-specific markers is needed to improve the detection accuracy. This requires a multiplexed approach to recognize and detect CTCs with different surface markers. Multiplexed detection was usually performed with fluorescence imaging coupled with CTC separation techniques.[103−106] In 2014, Nima reported a multiplexed imaging method based on surface-enhanced Raman scattering (SERS) mapping.[107] In their studies, silver−gold nanorods were coated with four different Raman reporters to detect four different surface markers with respective antibodies. Using the signature peak of each Raman reporter, the targeted surface marker was detected by SERS imaging. Compared to the fluorescence approach, SERS is advantageous in multiplexed detection because it gives narrow and fingerprint signals, have a low background, and excellent photostability.

In this work, we present a new multiplexed CTC assay that combines microchip-based immunomagnetic isolation with multicolor detection using magnetic-optical core−shell SERS nanotags. We use iron oxide−gold (IO−Au) core−shell SERS nanotags for the dual purpose of capturing cancer cells via immunomagnetic separation and subsequently detecting them via SERS spectroscopy in a microfluidic device. By varying the Raman reporter and the target antibody, we simultaneously capture and quantitatively detect four different surface protein markers on individual cells. The use of "all-in-one" IO−Au SERS nanotags in combination with a microfluidic device eliminates cumbersome sample processing and reduces the risk of CTC loss. Combining immunomagnetic enrichment with high specificity, multiplexed targeting for the capture of CTC subpopulations, multicolor SERS detection with high sensitivity and specificity, microfluidics for handling rare tumor cells and magnetic-optical nanoparticles (NPs) for dual

enrichment and detection, our integrated, yet simple and efficient platform shows strong potential to more sensitively detect and monitor cancer metastasis.

2. Materials and Methods

2.1 Materials

All chemicals were purchased from Sigma-Aldrich (St. Louis, MO) unless otherwise specified. All antibodies except HER2 from Sigma-Aldrich were purchased from BioLegend (San Diego, CA). QSY21 carboxylic acid-succinimidyl ester (QYS21- NHS), QXL680, BHQ3-COOH, and IR740 were purchased from Fisher Scientific (Waltham, MA), Anaspec (Fremont, CA), Biosearch Technologies (Dexter, MI), and Sigma-Aldrich, respectively. Isotype IgG was purchased from Fisher Scientific. Thiolated methoxy polyethylene glycol (mPEG-SH, MW = 5000) and thiolated polyethylene glycol N-hydroxy succinimide (HS-PEG-NHS, MW = 5000) were purchased from Nanocs (New York, NY). SKBR-3, MDA-MB-231, and MCF-7 breast cancer cells were purchased from ATCC (Manassas, VA). Dulbecco's modified Eagle's medium (DMEM) with high glucose (4.5 g/L), RPMI 1640 medium, 0.25% trypsin, and 100 U/mL HyClone penicillin−streptomycin (P/S) were purchased from VWR (Atlanta, GA). Fetal bovine serum (FBS), nonessential amino acids (NEAA), cell dissociation buffer, goat antimouse IgG conjugated with horseradish peroxidase (HRP), and bovine serum albumin (BSA) were purchased from Fisher Scientific (Waltham, MA). Human blood from healthy donors were purchased from Research Blood Components (Watertown, MA). 4′,6- Diamidino-2-phenylindole (DAPI), fluorescein isothiocyanate (FITC)-labeled CD45, 1-Step Ultra 3,3′,5,5′-tetramethylbenzidine (TMB)-enzyme-linked immunosorbent assay (ELISA) substrate solution, and Micro BCA reagent were purchased from Thermo Fisher Scientific.

2.2. Synthesis and Characterization of IO−Au Core−Shell NPs

Popcorn-shaped IO−Au core−shell NPs (IO−Au NPCs) were synthesized following the seed-mediated growth method developed by us previously.[43] Briefly, ferromagnetic octahedral IO NPs around 35 nm in edge length were synthesized as the core via precipitation of FeSO4 in a basic solution followed by oxidation in the presence of branched polyethyleneimine (PEI). Then, the PEI-stabilized IO NPs were coated with small Au NPs (<10 nm) via electrostatic adsorption to form seed particles. Popcorn IO−Au core−shell NPs were formed by anisotropic growth of the seed particles in a growth solution containing chloroauric acid, cetyl trimethyl ammonium bromide, ascorbic acid, and silver nitrate. The size and morphology of the IO core, Au-seeded IO NPs, and IO−Au NPCs were examined with a JEOL JEM1200EX II transmission electron microscope. The absorption spectra were collected using a visible−near-infrared (vis-NIR) absorption spectrometer (Ocean Optics, Dunedin, FL). Magnetic separation was performed with a Qiagen 12-tube magnet. The concentration of the NPs was determined via NP tracking analysis using a NanoSight LM10 microscope (Malvern Instruments). The size and zeta potential were measured by dynamic light scattering (DLS) using a Zetasizer Nano ZS (Malvern Instruments).

2.3. Preparation and Characterization of Multicolor IO−Au SERS Nanotags

To prepare IO−Au SERS nanotags, EpCAM, HER2, CD44, or IGF1R antibodies (Abs), or isotype IgG was functionalized with HS-PEG by incubating the Ab solution (10 μg) with HS-PEG-NHS (MW = 5000, Ab/NP = 100 in molar ratio) in phosphate-buffered saline (PBS, pH = 7.4) at 4 °C for 16 h. The thiolated Ab or IgG control was separated from free HS-PEG linkers by filtration with a centrifugal filter (30 kDa MWCO) (Pall Corporation). The purified HS-PEG-Ab or IgG control was mixed with 250 μL of 0.5 nM IO−Au NPCs (Ab/NP = 400) for 8 h at room temperature (RT). Then, Raman reporters (QSY21 for EpCAM, BHQ3 for HER2, QXL680

for CD44, and IR740 for IGF1R) were added with specific dyes at NP molar ratios (15,000 for QSY21, 15,000 for QXL680, 45,000 for BHQ3, and 5000 for IR740) and mixed with constant stirring for 15 min. Then, mPEG-SH (10^5 /NPC molar ratio) was added and the mixture was incubated with constant stirring for 45 min at RT. The resulting SERS nanotags were purified by centrifugation at 10,000 rpm for 10 min, re-dispersed in 250 μL of Dulbecco's PBS (DPBS), and stored at 4 ℃ until use. The size and zeta potential of the SERS nanotags were characterized by DLS. SERS signals were measured with a portable TSI ProRaman spectrometer (λ = 785 nm). The TMB assay was performed to confirm the successful conjugation of Ab to IO−Au NPCs by our conjugation method using HRP as the protein representative. Briefly, 100 μL of HRP-conjugated IO−Au NPCs were mixed with 25 μL of 1-Step Ultra TMB-ELISA substrate solution for 25 min and the color change of the solution was recorded. IO−Au NPCs without HRP was used as the negative control. The Micro BCA protein assay was used to determine the number of proteins bound to the NPs using IgG as the model. Briefly, IgG-linked IO−Au NPCs with various IgG loading ratios were mixed with the Micro BCA reagent with equal molar amounts and incubated for 60 min at 60 °C. The absorption at 562 nm was measured and compared against a standard curve of pure IgG solution.

2.4. Cell Culture and Cell Collection

SK-BR-3, MDA-MB-231, and MCF-7 breast cancer cells were cultured in their respective media (RPMI 1640 for SK-BR-3 and DMEM for MDA-MB-231 and MCF7) with 10% FBS, 1% NEAA, 100 U/mL penicillin, and 0.1 mg/mL streptomycin at 37 °C with 5% CO2. To collect cells, cells were cultured in a 6-well culture plate at a density of 5 × 104 cells/well and incubated for 48−72 h. Next, cells were washed three times with DPBS and

incubated in cell dissociation buffer for 10 min at 37 °C. The dislodged cells were centrifuged at 1500 rpm for 5 min and resuspended in DPBS for immediate use.

2.5. Characterization of Cell Surface Protein Expression with a Cellular ELISA

In a typical assay, 2000 cells per well (in 50 μL medium) were plated in a 96-well cell culture plate and incubated for 24−48 h at 37 °C with 5% CO2. Following a wash with PBST (PBS with 0.1% Tween 20 Detergent), cells were fixed in 50 μL of 1% paraformaldehyde for 12 min at 37 °C. Cells were then washed and nonspecific binding spots were blocked with 100 μL of 1% BSA for 30 min at 37 °C. After blocking, cells were washed once more and incubated with 50 μL of 2 μg/mL primary antibody for 1 h at 37 °C. This step was succeeded by three washes and labeling with 50 μL of 1:60 goat anti-mouse IgG-HRP (in 1% BSA) for 1 h at 37 °C. Following five more washes, 100 μL of TMB was added to each well and the plate was incubated at 37 °C for 10 min. After 10 min of incubation, the reaction was stopped with 100 μL of 2 M sulfuric acid. Finally, the absorbance of each well was measured at 450 nm using a BioTek ELx800 microplate reader.

2.6. Cellular Binding and SERS Detection of Cancer Cells with IO−Au SERS Nanotags

In a microcentrifuge vial, 100 μL of DPBS containing ∼5 × 104 cells (SK-BR-3, MDA-MB-231, or MCF7) and four-color nanotags (each 12.5 pM) or an IgG control nanotag were incubated for 30 min at 37 °C with intermittent mixing. Following incubation, the labeled cells were centrifuged and fixed in 1% paraformaldehyde for 15 min at 25 °C. After purification by centrifugation, the cells were resuspended in DPBS and examined under a dark field using an Olympus IX71 inverted microscope and measured with a Raman microscope.

2.7. Fabrication of Microfluidic Device

The microfluidic device was designed with COMSOL Multiphysics software. The chip contained two transparent quartz slides, each of 4.5 cm length, 1.5 cm width, and 1 mm thickness, fused together. The top slide contained through-hole fluidic ports (D = 1 mm), whereas the bottom slide had microfluidic channels with a depth of 100 μm. After fusion, the microchannel was sandwiched between the two slides with access only through the ports. The major components of the device were: the isolation and detection chambers (20 mm length × 5 mm width × 0.1 mm thickness), six fluidic ports (A to F), and the connection channels (1 mm width × 0.1 mm thickness). A cylindrical neodymium−iron− boron (NdFeB) magnet with a diameter of 20 mm and a thickness of 25 mm was attached to the chip under the chamber to capture NP-bound CTCs. The six ports were as follows: A is connected to the blood sample inlet, B supplies PBS to wash the cells after each step, C supplies the fix solution to fix the cells, D supplies FITC-labeled CD45 monoclonal antibodies to recognize WBC impurities, E supplies DAPI to counterstain the cell nucleus, and F is the waste outlet. The channel was terminated at the fluidic ports that were connected to a syringe via capillary and port assemblies. The chamber held ∼10 μL solution. The dead volume in each side channel will be less than 1 μL. The microfluidic device was fabricated commercially by Micronit Microfluidics.

2.8. Determination of the Flow Rate for Magnetic Cell Capture in Microfluidic Device

To determine the flow rate that preferentially captures cancer cells over free NPs, SK-BR-3 cells were labeled with a cocktail of anti-EpCAM and anti-HER2 IO−Au NPCs, purified by centrifugation, and fixed with paraformaldehyde using the procedure described above. 1 mL of 300,000 labeled cells were pumped through the microfluidic chip at a range of flow rates. Uncaptured cells were collected and counted using a hemocytometer to determine the capture

efficiency of labeled cells. To determine the capture efficiency of free NPs, 1 mL of 5 pM mPEG-stabilized IO−Au NPCs were flowed through the microfluidic chip under the presence of the magnet at various flow velocities and collected at the end. Uncaptured NPs were quantified by UV−vis absorption spectroscopy. Capture efficiency was calculated as the percentage of captured cells or NPs over the added amount of cells or NPs.

2.9. Magnetic Capture and SERS Detection of CTCs in the Microfluidic Device

In a microcentrifuge vial, 100 μL of human blood spiked with 1000 breast cancer cells (SK-BR-3, MDA-MB-231, or MCF-7) were incubated with a cocktail of 4-color nanotags (each of 12.5 pM final concentration) or an IgG control nanotag for 30 min at 37 °C with intermittent mixing. Then, the solution was diluted to 1 mL with DPBS and flowed across the microfluidic device in the presence of the magnet with a flow rate of 50 μL/min, followed by washing with DPBS. Captured cells were fixed by 1% paraformaldehyde for 10 min. After washing with DPBS, the cells were stained with 300 nM DAPI for 5 min. After washing with DPBS, captured cells were labeled with 1 μg/mL FITC antihuman CD45 antibodies for 30 min. After washing, the cells were examined with an integrated Raman/fluorescence microscope that consists of an Olympus CX41 fluorescence microscope and a TSI ProRaman L spectrometer with laser excitation at 785 nm. The SERS spectra on single cells were collected with a 40× objective. The laser spot size at focus is 30 μm. The laser power is 100 mW and the acquisition time is 10 s. Fluorescence images were collected with a DAPI filter ($\lambda_{excitation}$ = 387/11 nm; $\lambda_{emission}$ = 447/60 nm) to visualize cell nuclei and an FITC filter ($\lambda_{excitation}$ = 482/35 nm; $\lambda_{emission}$ = 536/40 nm) to visualize WBCs.

2.10. Signal Deconvolution and Data Analysis

The total SERS signal from a cell or solution is deconvolved (unmixed) with the direct classic least squares (CLS) method to derive signal contribution from each nanotag using Solo+MIA software (Eigenvector Research, Inc.). Specifically, the total SERS signal (S_{total}) from a mixture is considered as a linear addition of those from individual nanotags S1 to S4 on the cell: $S_{total} = C_1S_1 + C_2S_2 + C_3S_3 + C_4S_4 + \Delta$, where C_1 to C_4 are the weight factor for the four nanotags and Δ is the residual error to be minimized for optimal choices of the weight factors. The weight factor for each nanotag is the relative SERS signal intensity to the SERS spectrum of the pure nanotag solution. The SERS spectrum of the pure nanotag solution was collected with 25 pM (NP concentration) IO−Au SERS nanotags with a 100 μm Raman probe. The laser power was 25 mW and the acquisition time was 1 s.

2.11. Simultaneous Detection of Multicolor SERS Nanotags in a Mixed Solution

To verify the accuracy of the CLS method for signal deconvolution, we prepared four-color SERS nanotags with mPEG-SH stabilization and made mixture solutions with varying concentration of the individual nanotags. Specifically, QSY21, BHQ3, QXL680, or IR740 Raman reporters were added to IO−Au NPCs with a specific dye to particle molar ratios (15,000 for QSY21, 15,000 for QXL680, 45,000 for BHQ3, and 5000 for IR740) and mixed with constant stirring for 15 min. Then, mPEG-SH (105 /NPC molar ratio) was added and the mixture was incubated with constant stirring for 45 min at RT. The resulting SERS nanotags were purified by centrifugation at 10,000 rpm for 10 min and redispersed in DPBS to obtain a 10 pM solution. A series of mixture solutions were prepared by adding different amounts of four-color nanotags with varied ratios. Raman signals of the different mixture solutions were collected and signals were deconvolved to calculate the SERS weight factor for each nanotag in each solution.

The experimental values were compared with theoretical values with linear regression to calculate the accuracy of detection for each nanotag in each solution.

2.12. Comparison between ELISA and Multicolor SERS Method

The correlation of the ELISA results with those of SERS methods with cells suspended in PBS and in blood was analyzed using a Pearson correlation test and their linear relationship was assessed using curve fits. Additionally, the correlation between the SERS results in PBS and blood was compared with each other in a similar fashion and the agreement between the two sets was examined. The correlation coefficient *r* was calculated between the SERS mean weight factor and the ELISA mean absorbance for each of the four markers in every cell line, yielding a total of 12 data points for each of the three sets. The *t*-statistic was calculated from *r* using Student's *t*-distribution with degrees of freedom $n - 2$, as shown in eq 2.1. The *p*-value was determined from the *t*-statistic based on a one-tailed distribution and a null hypothesis of $r = 0$.

$$t = r\sqrt{\frac{n-2}{1-r^2}} \qquad (2.1)$$

The ELISA mean absorbance was plotted as a function of the mean weight factor of the SERS method to examine the correlation between ELISA and SERS methods with standard deviation (SD) for each sample. To assess the linear relationship between ELISA and SERS, the SERS weight factor was fitted as a linear function *f(x)* of the ELISA absorbance *(x)* using an ordinary least squares regression. The root-mean-square error (RMSE) of the fits was calculated with respect to the ELISA absorbance ($RMSE_{ELISA}$) and the SERS weight factor ($RMSE_{SERS}$) to estimate the lower and upper uncertainty bounds as shown in eq 2.2.

$$f_{bounds} = f(x \mp RMSE_{ELISA}) \pm RMSE_{SERS} \qquad (2.2)$$

The same method is used to compare the results of the SERS method between PBS and blood. The uncertainty bounds are defined by this RMSE, as presented in eq 2.3.

$$f_{bounds} = f(x \mp RMSE) \pm RMSE \qquad (2.3)$$

3. Results and Discussion

3.1. Design of CTC Capture and Multiplexed Detection

Because of their scarcity in blood, identification of CTCs generally requires the combination of enrichment and detection technologies. Materials that allow dual separation/ detection modalities are highly desirable in order to develop a simple, rapid, and efficient detection method. We use magnetic-optical IO−Au NPCs to dually capture CTCs through immunomagnetic separation and detect them with the SERS technique via the adsorbed Raman reporter (Figure 2.1). Immunomagnetic separation is the most commonly used method to isolate and enrich CTCs because it is rapid and highly specific. It avoids nontumor cells that are morphologically similar to CTCs. Immunomagnetic separation under flow conditions is a highly efficient way to capture NP-bound CTCs without capturing free magnetic NPs at appropriate flow rates.[86,108] This is because magnetic force is proportional to bound NP numbers.[109] The free NPs are more effectively removed by flow drag forces than the cells which contain a number of NPs.

We perform the immunomagnetic separation in a microfluidic device. The microfluidic device provides a venue for producing a highly integrated system that can process clinical samples in closed architectures to minimize sample contamination and loss.[110−112] It enables user-friendly automation on a single device, reducing human intervention and operational errors.

The microfluidic chip is very important for enriching low-frequency CTCs to reduce false signals. It also allows on-chip staining for negative selection to reduce false positives. In addition, it allows single-cell analysis so as to increase the detection accuracy. Cell isolation in the channel can be simply achieved with permanent magnets under the chip.[113–118] The capture efficiency (percentage of captured cells over the total number of cells) and the sample throughput can be precisely controlled through the design of the fluidic channel and the control of the flow rate.

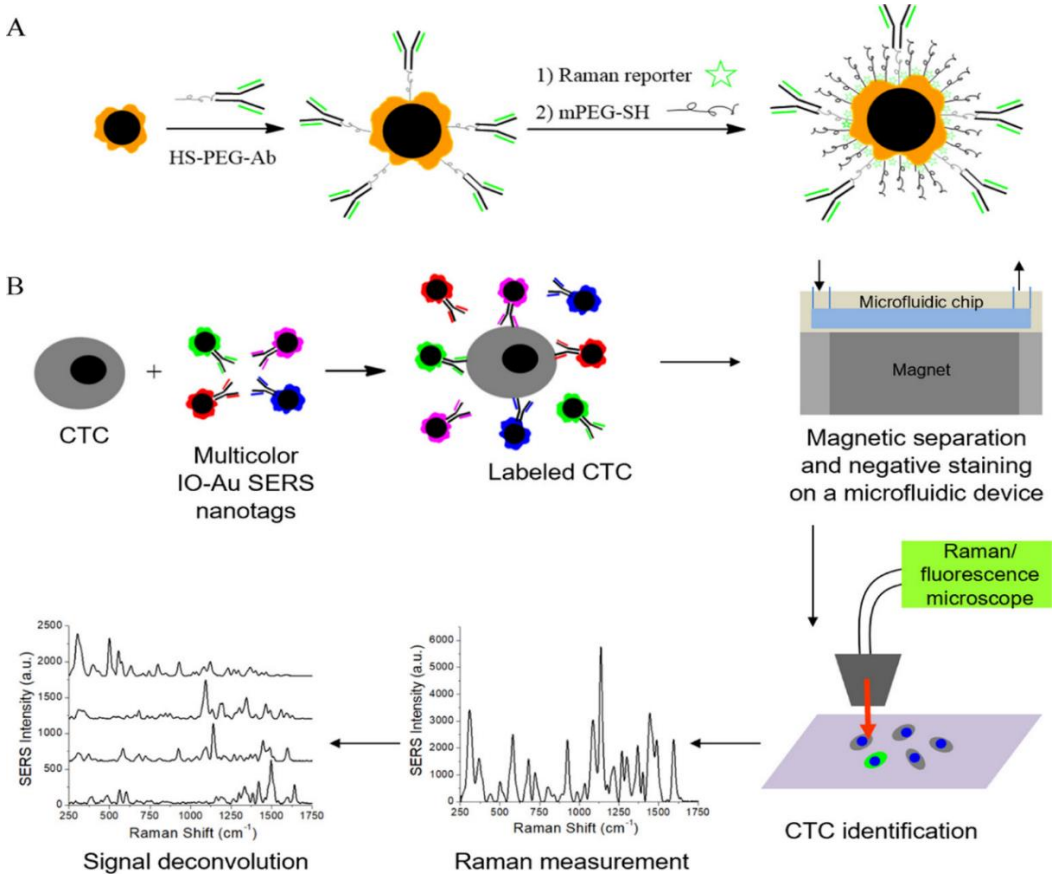

Figure 2.1 Design of CTC immunomagnetic capture and multiplexed detection with multicolor IO−Au core−shell SERS nanotags. (A) Preparation of IO−Au SERS nanotags. By varying the Raman reporter and the antibody, four-color IO−Au SERS nanotags were prepared to target four different surface markers. (B) Methodology for CTC labeling, microfluidic-based magnetic separation, and single-cell Raman detection using multicolor IO−Au SERS nanotags. Signals from each SERS nanotag is obtained by deconvolution of a total SERS spectrum of single cells with the classic least squares fitting method.

To improve SERS detection sensitivity, we use anisotropic IO−Au NPCs. Anisotropic NPs give orders of magnitude stronger SERS signals than the spherical counterparts because of their stronger electronic field enhancement.[44] We design four-color SERS nanotags to detect four different surface cancer proteins including EpCAM and three breast cancer surface markers HER2, CD44, and IGF1R. To quantify the expression of each targeted cancer marker, the total SERS signal from individual cells was unmixed with CLS fitting to determine the level of each nanotag on the cells. To increase the reliability of CTC detection, we performed counterstaining with DAPI to confirm the presence of cell nucleus and with FITC-labeled CD45 antibodies to identify WBC impurities. We performed all cell isolation/enrichment, negative staining, optical imaging, SERS detection, and molecular profiling in a microfluidic device, which is simple and easy to operate.

3.2. Properties of Multicolor IO−Au Core−Shell SERS Nanotags

IO−Au NPCs were synthesized via a seed-mediated growth method.[43] Figure 2.2 (A−C) shows typical TEM images of IO NPs, Au seed-coated IO NPs, and IO− Au NPCs. The IO−Au NPCs, which were about100 nm in size, exhibited a localized surface plasmon resonance (LSPR) peak at 620 nm, whereas the Au seed-coated IO NPs had an LSPR at 560 nm (Figure 2.2 D). Systematic characterization in previous studies have shown that the IO−Au NPCs are core− shell structures with ferromagnetic properties.[43] Figure 2.2 E shows a photograph of the IO−Au NPCs before and after separation with a 12-well tube magnet.

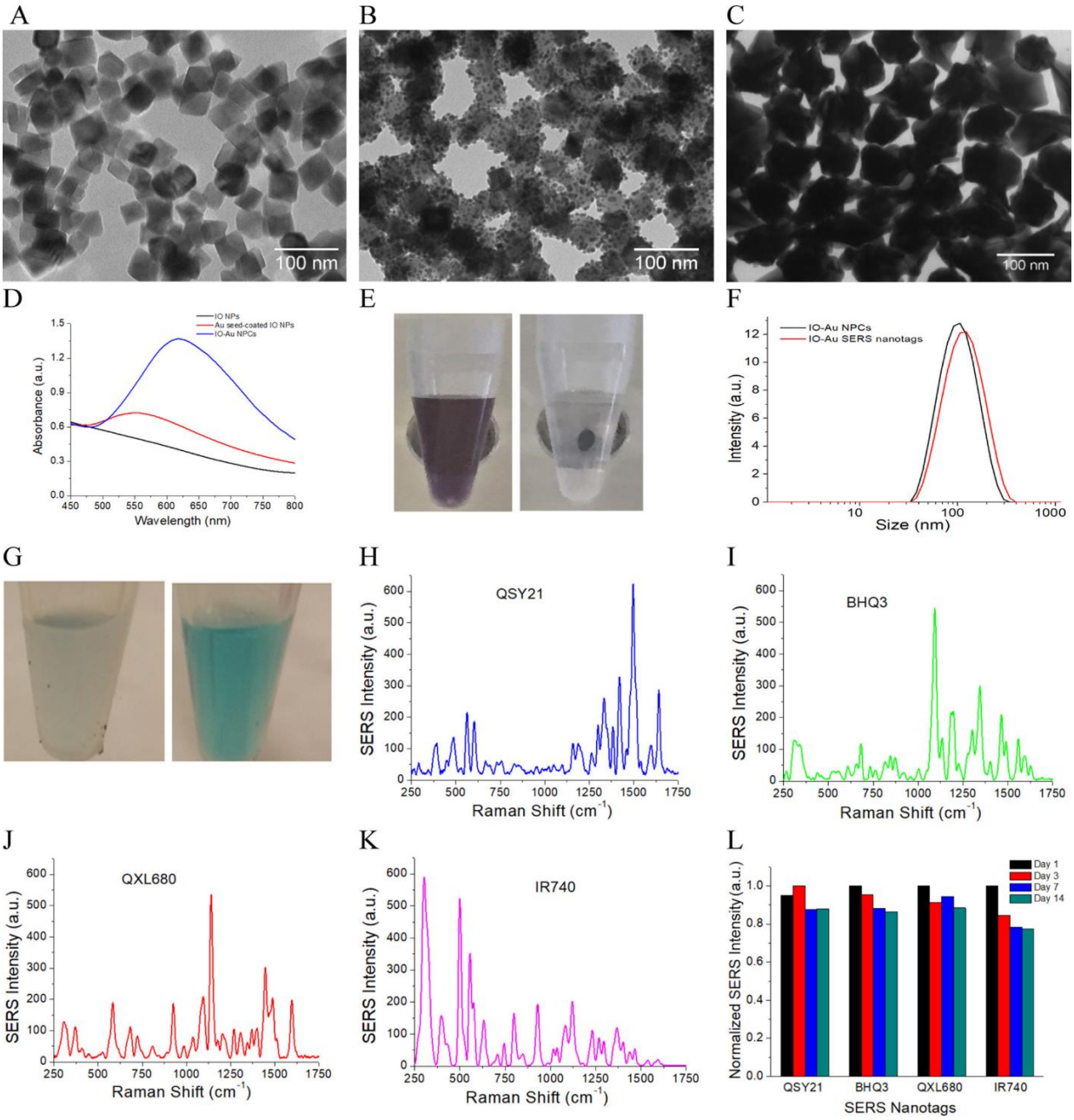

Figure 2.2 Characterization of IO−Au NPCs and SERS nanotags. (A−C) TEM image of IO NPs (A), Au seed-coated IO NPs (B), and IO−Au NPCs (C). (D) Absorption spectra of IO NPs, Au seed-coated IO NPs, and IO−Au NPCs. (E) Photographic picture of IO−Au NPCs before (left) and after (right) magnetic separation. (F) DLS characterization of the size distribution of IO−Au NPCs and IO−Au SERS nanotags. (G) Confirmation of the presence of proteins on IO−Au NPCs using HRP by the TMB assay. Left: IO−Au NPCs. Right: HRP-conjugated IO−Au NPCs. (H−K) SERS spectrum of IO-Au SERS nanotags coated with QSY21 (H), BHQ3 (I), QXL680 (J), and IR740 (K). (L) Examination of the stability of SERS nanotags. SERS signal intensities were measured at 1497 cm^{-1} for QSY21, 1092 cm^{-1} for BHQ3, 1139 cm^{-1} for QXL680, and 501 cm^{-1} for IR740. They were normalized to the signal intensities at day 1 for each nanotag.

The IO−Au SERS nanotags were prepared by nonspecific adsorption of Raman reporters and covalent binding of targeting Ab through a PEG-HS linker with further stabilization by mPEG-SH (Figure 2.1 A). To optimize the Ab surface density, we performed cellular binding studies with the SERS NPs linked with different loading ratios of Ab to NP using HER2 Ab as the model. The dark-field image shows that increasing the HER2 Ab loading ratio from 25 to 100 increased the amount of NPs on the HER2-positive SK-BR-3 cells (Figure S1). No significant difference was observed when the HER2 loading ratio was increased from 100 to 200. Thus, we used Ab/NP of 100 to prepare the SERS nanotags in all the studies. DLS measurements showed that the Ab and PEG conjugation increased the size of IO−Au NPCs by 20 nm (Figure 2.2 F). The zeta potential decreased from +35 to −5 ± 10 mV. The color change in the TMB assay showed the presence of proteins on the IO−Au NPCs (Figure 2.2 G). We further determined the number of Abs per NP using the Micro BCA protein assay with IgG as the protein model. The results showed that there were approximately 25 Abs bound to each IO−Au NPC. (Figure S2 and Table S1).

For multiplexed detection, we made four-color SERS nanotags with four different organic dyes, QSY21, BHQ3, QXL680, and IR740, to detect EpCAM, HER2, CD44, and IGF1R, respectively. The loading ratio of these Raman reporters was adjusted to give similar SERS signal intensity at their representative peak (Figure 2.2 H−K). The SERS nanotags were relatively stable in PBS (Figure 2.2 L). At day 14 after preparation, all nanotags showed ≥85% signal intensity of those at day 1 except IR740 nanotags. The SERS intensity of IR740 is 77% of that at day 1. In our experiments, we used freshly prepared nanotags that have similar SERS intensities at the representative SERS peak intensity (QSY21 at 1497 cm^{-1}, BHQ3 at 1092 cm^{-1},

QXK680 at 1139 cm^{-1}, and IR740 at 501 cm^{-1}). We further studied the stability of the nanotags in whole blood. As the interaction of the nanotags with blood is less than 1 h (30 min for cellular binding and 20 min for microfluidic magnetic separation), we focused our study within the first few hours of mixing of the nanotags and blood from a healthy donor. The results from repeated experiments (n = 3) showed that there were no significant differences among the four groups (t = 0, 0.5, 1.5, and 3.5 h) (Figure S3). Signal fluctuation is most likely due to the interference (such as scattering of the Raman laser light) by the abundant blood cells during Raman measurement. The SERS IO−Au NPs were further characterized by examining their cellular binding to three model BC lines, SKBR-3, MDA-MB-231, and MCF-7. These cell lines have varied expressions of EpCAM, HER2, CD44, and IGF1R,[119−121] which we have confirmed with flow cytometry (Figure S4).

We choose HER2, CD44, and IGF1R as additional markers for CTC recognition based on their clinical significance in the BC model. HER2 is a member of the epidermal growth factor receptor family having tyrosine kinase activity. It is overexpressed in 15−30% BC.[122] CD44 is associated with triple negative BC.[123] IGF1R belongs to the large class of tyrosine kinase receptors and is overexpressed in many cancers such as breast, colon, prostate, and nonsmall cell lung.[124] It plays an important role in breast cancer metastasis.[125,126] In agreement with flow cytometry data, the dark-field images show that SK-BR-3 has high levels (the presence of golden color NPs) of EpCAM and HER2, MDA-MB-231 of CD44, and MCF-7 of EpCAM and CD44 (Figure 2.3). Expression of IGF1R is also significant on MCF-7 cells. These results suggest specific binding of the four-color SERS nanotags to their targeted cancer proteins on different cancer cell lines.

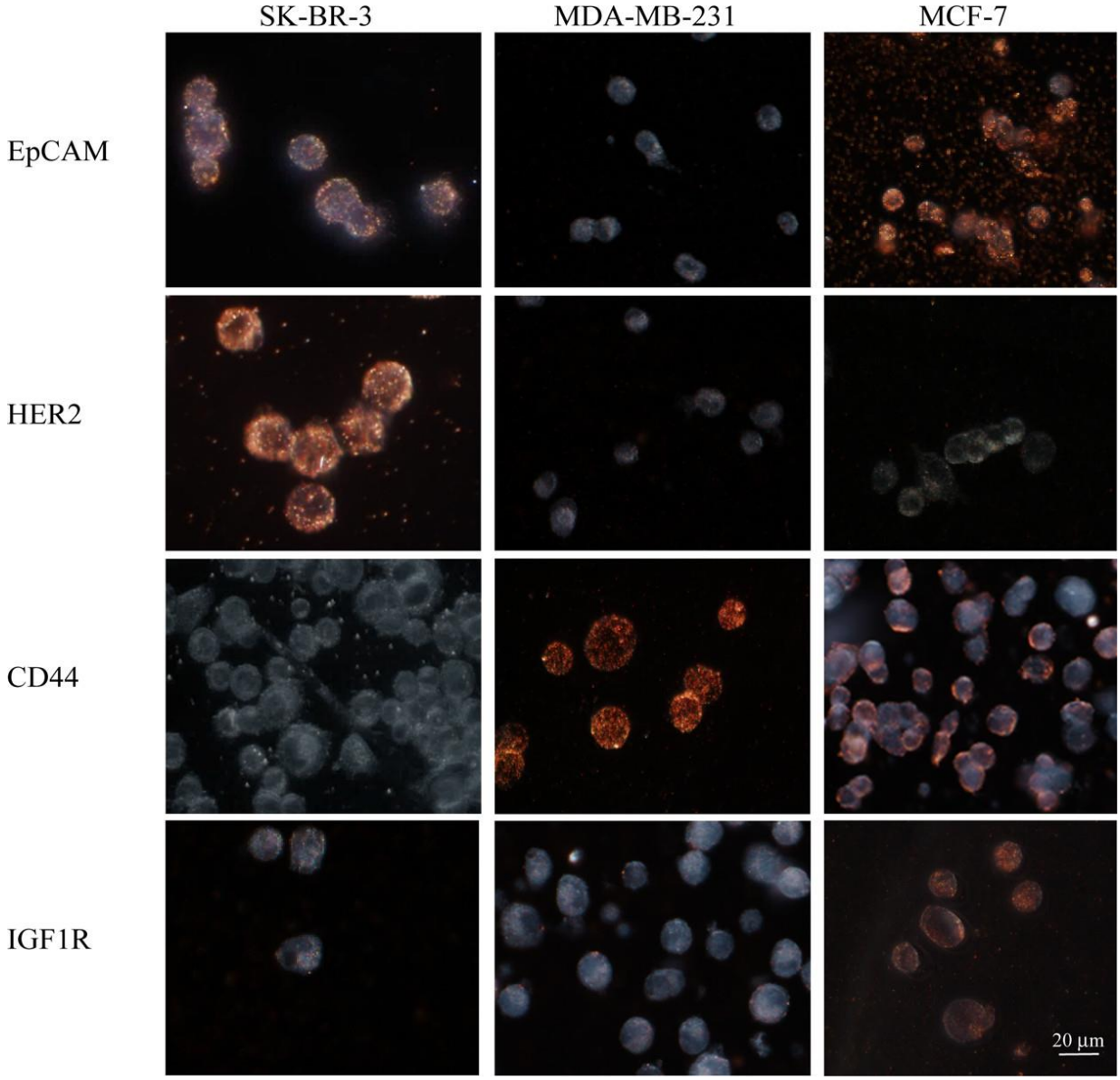

Figure 2.3 Characterization of cellular binding of the four-color IO−Au SERS nanotags to different breast cancer cell lines with dark-field imaging. The IO−Au NPCs were coated with QSY21, QXL680, BHQ3, and IR740 and conjugated with anti-EpCAM, anti-HER2, anti-CD44, and anti-IGF1R monoclonal antibodies, respectively. The bound NPCs are shown in golden color in the dark-field images.

3.3. Multicolor IO−Au SERS Nanotags for Quantitative Measurement of Surface Protein Markers on Cancer Cells

SERS is very promising for multicolor detection because it gives narrow peaks. However, a Raman reporter gives many peaks, which makes it difficult to identify one distinct peak for each tag when three and more colors are needed simultaneously. To solve the limitation, an alternative way is signal deconvolution using the reference spectrum from pure nanotag.[127] The deconvolution was done with CLS regression based on the fact that the total SERS signal from a mixed solution is a linear combination of the SERS signals of individual nanotags (Figure S5). The contribution of each tag is measured by the weight factor. To test the robustness of CLS for signal deconvolution, we mixed the four-color SERS nanotags in various ratios, measured the SERS spectrum of the mixture, and calculated the weight factor from each tag (Figure 2.4). The results show that the experimentally measured fraction of a nanotag in the mixed solution matches well with the theoretical values. For example, in the QSY21/BHQ3/ QXL680/IR740 = 2:1:1:1 sample, the intensity of the SERS spectrum from the QSY21 nanotag in the mixture solution is 2/5 of that of the pure QSY21 nanotag because of the dilution by other three nanotags. Thus, the theoretical C_{QSY21} is 0.4. The C_{QSY21} calculated by CLS fitting is 0.400094. The theoretical values of C_{BHQ3}, C_{QXL680}, and C_{IR740} are 0.2. The calculated C_{BHQ3}, C_{QXL680}, and C_{IR740} are 0.18529, 0.21252, and 0.20075, respectively. The accuracy for the detection of QSY21, BHQ3, QXL680, and IR720 nanotags is 99.98, 92.65, 93.74, and 99.62%, respectively (Table S2). The mean accuracy of detecting all nanotags in all the samples is 95.53%.

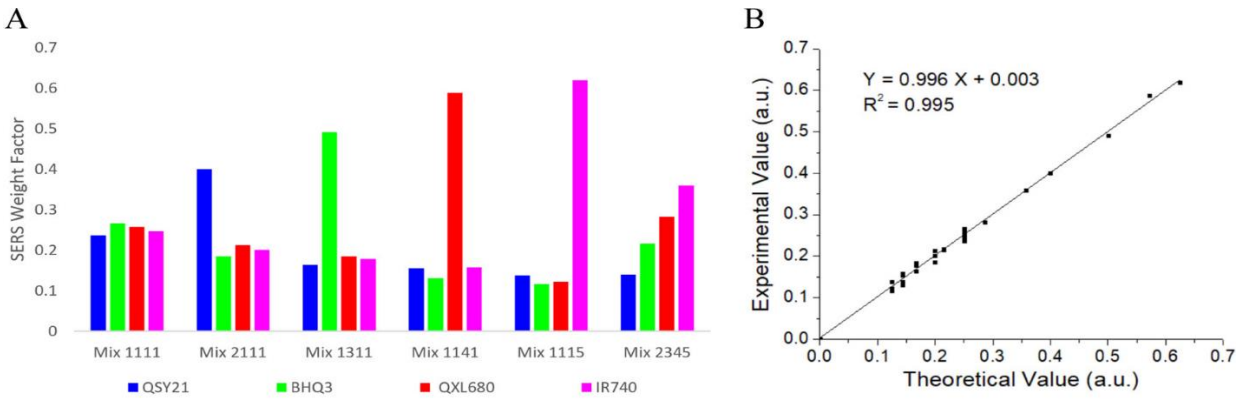

Figure 2.4 Examination of the accuracy of multicolor SERS nanotags with CLS fitting for multiplexed detection. (A) Plot of experimentally measured SERS weight factors vs theoretical weight factors for each nanotag in each mixed solution. (B) Linear correlation of the measured and theoretical values.

To examine the ability of the multicolor IO−Au SERS nanotags for multiplexed detection, we incubated each of SK-BR3, MDA-MB-231, or MCF-7 cells in PBS with a cocktail of four-color nanotags for 45 min and separated the labeled cells from free nanotags by low-speed centrifugation. The cells were placed on a quartz coverslip and SERS signals from individual cells were collected with a Raman microscope. Fifty cells were measured and CLS regression was used to extract the signals from each nanotag for each cell. The weight factor for each nanotag on each cell (n = 50) is shown in Figure 2.5 A. The results show that the expression is certainly heterogenous at the single-cell level. To better compare the expression levels of different markers, we repeated three times and the mean with SD is plotted in Figure 2.5 B. The results show that EpCAM and HER2 are highly expressed on SK-BR-3 cells, CD44 on MDA-MB-231 cells, and EpCAM and CD44 on MCF-7 cells, which are consistent with flow cytometry results (Figure S2) and dark-field imaging (Figure 2.3). It is important to mention that the SERS weight factor is the relative intensity of the SERS spectrum of a nanotag on a cell to a reference SERS spectrum of the pure nanotag we defined.

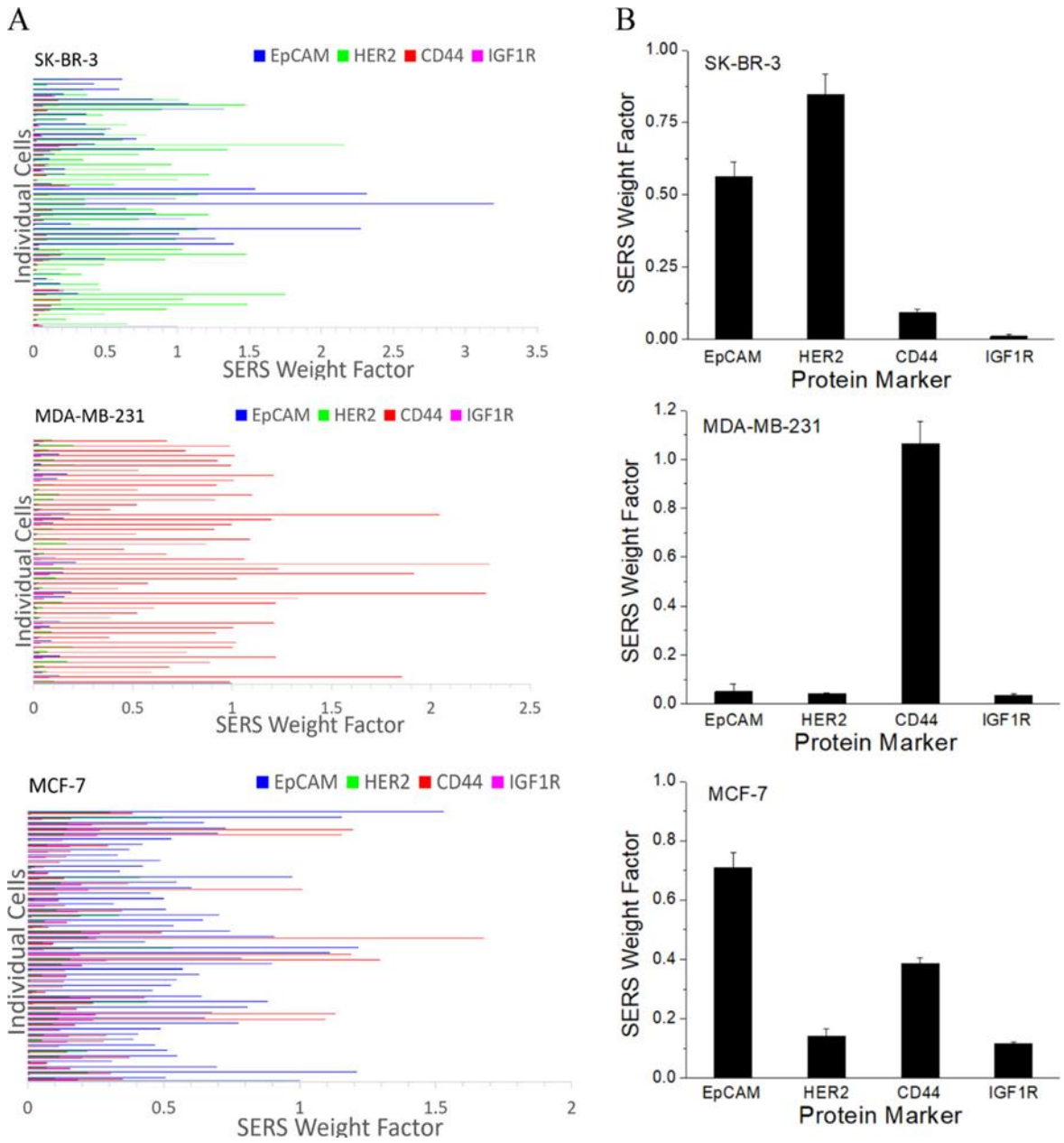

Figure 2.5 Detection of surface protein markers on cancer cells in PBS with four-color IO–Au SERS NPs. (A) SERS weight factor of each marker from 50 individual cells. (B) Mean SERS weight factor from triplicate measurement of the protein markers for each cell line.

In our studies, we used 25 pM IO−Au SERS nanotag solution to collect the reference spectra (shown in Figure 2.2). The signals were taken using a 100 μm Raman probe with a laser power of 25 mW and an acquisition time of 1 s. Based on the sample volume under the Raman probe and the concentration of the nanotag solution, we estimated that the signals of the reference SERS spectrum were produced by 6×10^5 nanotags. To generate the same strength of SERS signals under the cell measurement conditions (laser power: 100 mW; acquisition time: 10 s), it will require approximately 1.5×10^4 nanotags. Based on this information, together with the value of the SERS weight factor, we can estimate the number of nanotags bound to each surface protein. For example, in the SKBR3 cell line, the weight factor for EpCAM, HER2, CD44, and IGF1R was 0.56, 0.85, 0.09, and 0.01, respectively. Therefore, the estimated number of nanotags bound to EpCAM, HER2, CD44, and IGF1R is 8400, 12750, 1350, and 150, respectively.

3.4. Immunomagnetic Cell Capture in the Micro-fluidic Chip

To detect CTCs in blood, we fabricated a microfluidic device to isolate the tumor cells with an external magnet from the blood components and free NPs and immobilize them on the chip for optical detection. The device was designed in such a way that it meets the following criteria: (1) transparent for optical imaging and detection; (2) with no or minimal fluorescence and Raman background signals; (3) flat channel surface; (4) with laminar flow in the channel; (5) with high throughput for processing large volumes of sample; (6) adaptable with the Raman detection system, and (7) cost effective.

Figure 2.6 A−C shows the schematics of the chip that shows the dimension of the chip and magnetic separation with a permanent magnet underneath. Figure 2.6 D is a photograph of the fabricated chip with the holder and collecting tubes. The chip was made of two transparent quartz slides that were fused together to form an isolation and detection chamber. Unlike

polymer-based materials, quartz has no Raman background and is nonfluorescent. The top slide contained the inlet and outlet ports, whereas the bottom slide had the microfluidic chamber (20 × 5 × 0.1 mm) and connection channels with a depth of 100 μm. Six ports were designed to have different functions, with port (A) for supplying blood samples, (B) PBS to wash the cells after each step, (C) paraformaldehyde solution to fix the cells, (D) FITC-conjugated CD45 antibodies to label WBCs, (E) DAPI to counterstain the cell nucleus, and (F) to act as a waste outlet. The chamber held ∼10 μL solution. The dead volume in each side channel was less than 1 μL. The channel bends were angled at 60° or less along the flow direction to reduce sheer stress on the cells flowing with the fluids. These angular junctions, a bioinspired approach mimicking blood vessel branching, minimize vortex formation and allow smooth laminar flow of fluids inside the channels. The chip was placed on top of a NdFeB magnet (D = 20 mm and L = 25 mm) with the channel centered on the magnet. The surface field of the magnet was 5000 Gauss. Because of the short distance between the surface of the magnet and the channel (1 mm), the field at the channel was estimated to be the same as that on the surface of the magnet.

To determine a flow rate to preferentially capture cancer cells over free NPs, we examined the effect of capture efficiencies of IO−Au NPCs and SK-BR-3 cells prelabeled with a cocktail of anti-EpCAM- and anti-HER2-conjugated IO−Au nanotags (Figure 2.6 E). When the flow rate increased from 10 to 200 μL/min, the capture efficiencies of the cells decreased from 90 to 82% and the IO-Au NPCs decreased from 38 to 7%. To consider both the speed and the cell capture efficiency, we choose 50 μL/min as the working flow rate to capture cancer cells in blood for detection. At this flow rate, about 20% free NPs were captured. To minimize the effect of the captured free NPs, SERS signals from the individual cells were subtracted with the background spectrum that was taken from an area in the chip without cancer cells.

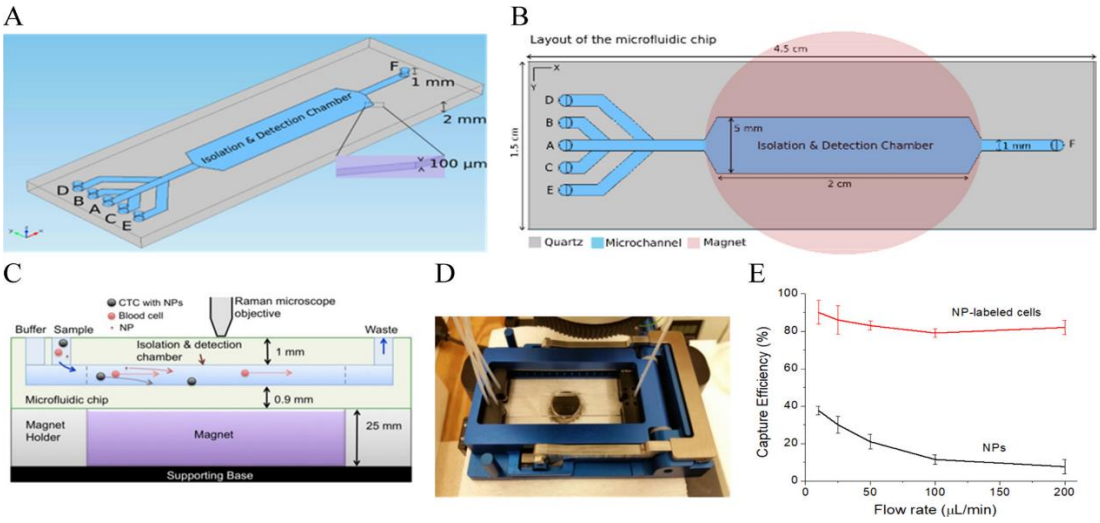

Figure 2.6 Design and characterization of the microfluidic device for on-chip magnetic isolation and optical detection of CTCs. (A) 3D view, (B) layout, and (C) cross-sectional view (not to scale) of the microchannel with a magnet underneath. (D) Photograph of the fabricated microfluidic device. (E) Capture efficiencies of SK-BR-3 cells labeled with a cocktail of anti-EpCAM and anti-HER2 IO−Au NPCs (red curve) and free IO−Au NPCs (black curve).

3.5. Multiplexed Surface Protein Marker Detection of Spiked Cancer Cells in Human Whole Blood

To mimic CTCs, we spiked breast cancer cells into 1 mL of human blood from healthy donors. Three cell lines, SK-BR-3, MDA-MB-231, and MCF-7, were used to test the validity of our technique as these cells have varied expressions of EpCAM, HER2, CD44, and IGF1R. Following the procedure described above in the Experimental Section, we obtained the fluorescence images and the Raman spectrum of captured cells in the microfluidic device. We determined that a cell was a cancer cell when it satisfied the following criteria: (1) it met morphologic features (nearly round or oval morphology); (2) it had a visible nucleus (DAPI positive); (3) it was CD 45 negative, and (4) it was EpCAM, HER2, CD44, or IGF1R positive. A cell was identified EpCAM-, HER2-, CD44-, or IGF1R-positive when it was SERS-positive. A cell was defined as SERS-positive based on the Rose criterion, in which the intensity of the

Raman peak of the reporter from a whole cell was at least 5 times higher than the SD of the background noise collected from a neighborhood area without cells. The spectra from both signal and noise were automatically baseline-corrected in advance using a multisegment polynomial fitting to subtract the weak fluorescence and SERS background (broad continuum emission). This baseline correction was applied for all the Raman spectra we obtained in this study.

Figure 2.7 A−C shows an example of the optical images of a captured cancer cell in bright- and fluorescence-imaging modes. Bright-field imaging showed the round morphology of a cancer cell. The cell was DAPI-positive and CD45- negative, which further confirmed the cancer cell features. In contrast, a WBC showed positive staining with FITC-CD45 antibodies and was excluded in the following SERS analysis (Figure 2.7 D)

Figure 2.7 E shows the distribution of the weight factors for each nanotag across 50 cancer cells from each cell line, with the mean ± SD being plotted in Figure 2.7 F. The results from cells in blood was similar to those in PBS, as shown in Figure 2.5. Again, EpCAM and HER2 were highly expressed on SK-BR-3 cells, CD44 on MDA-MB-231 cells, and EpCAM and CD44 on MCF-7 cells. To validate the multicolor SERS method for analysis of tumor cells in blood, we measured protein expressions with indirect ELISA using the same primary antibodies as those in the SERS methods. Figure 2.8 A−C shows the level of EpCAM, HER2, CD44, and IGF1R expression on the three cancer cell lines. Similar to the SERS method (Figures 2.5 and 2.7), EpCAM and HER2 were highly expressed on SK-BR-3 cells, CD44 on MDA-MB-231, and EpCAM and CD44 on MCF-7 cells.

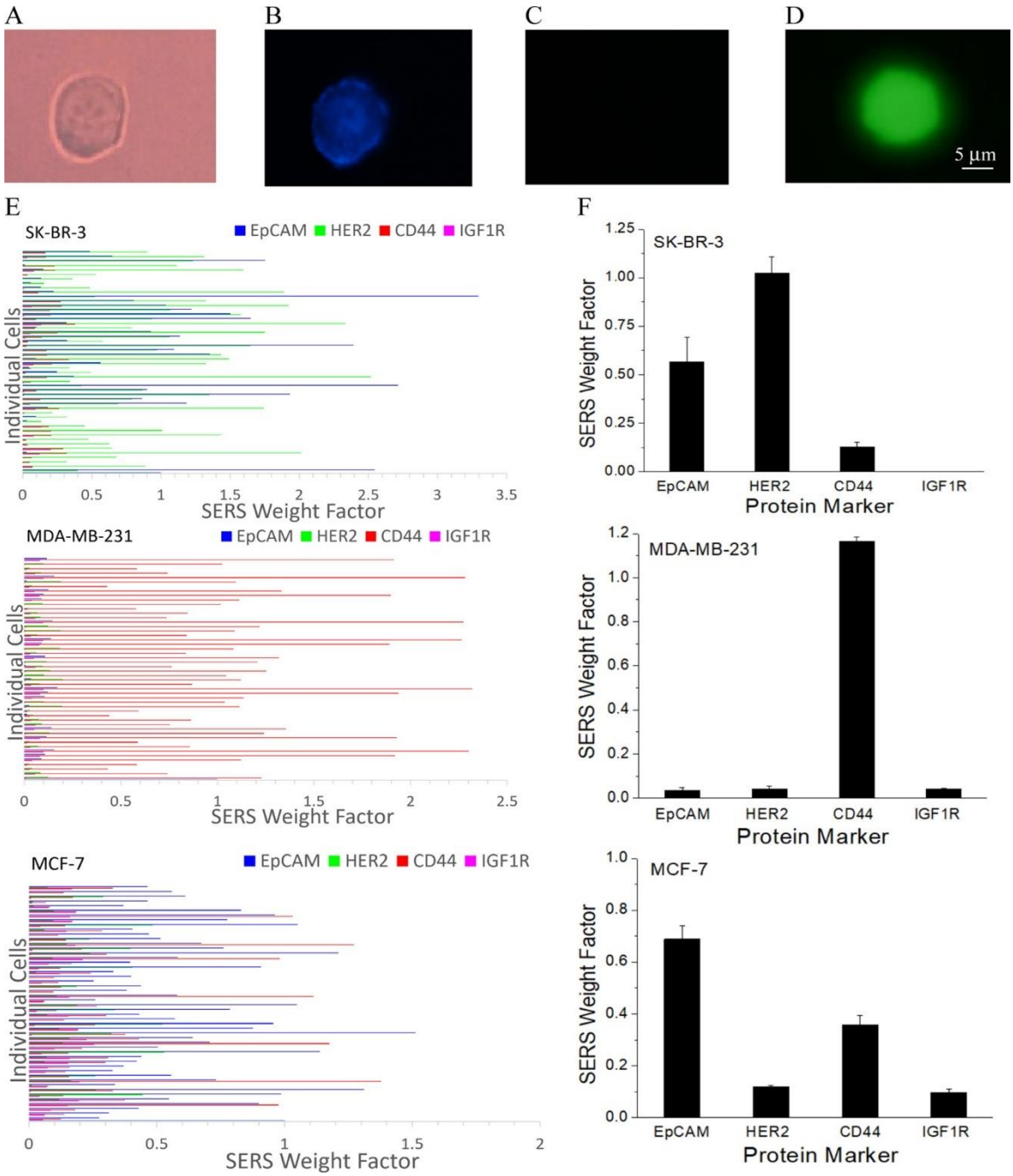

Figure 2.7 Detection of surface protein markers on spiked cancer cells in human blood with four-color IO–Au SERS nanotags. (A) Bright-field image of a cancer cell. (B) Fluorescence image of the cell in (A) with a DAPI filter showing the cell nucleus. (C) Fluorescence image of the cell in (A) with a FITC filter showing the cell is CD45-negative. (D) Fluorescence image of a WBC cell with a FITC filter showing the cell is CD45-positive. (E) Plot of SERS weight factor across individual cancer cells (n = 50). (F) Mean SERS weight factor from triplicate measurements of the protein markers for each cell line.

To quantitatively examine the correlation between ELISA and SERS methods, the ELISA mean absorbance was plotted as a function of the mean weight factor of the SERS method using cancer cells suspended in PBS or blood (Figure 2.8 D,E). The results showed that the SERS method was strongly correlated with ELISA, with high correlation coefficients ($r \geq 0.97$) and low p-values ($p < 10^{-6}$). The coefficients of determination R^2 for the linear fits between ELISA and SERS (black lines) were relatively high, with $R^2 > 0.94$. Nearly all the points fell within the uncertainty bounds of the fit (red lines). The $RMSE_{SERS}$ and $RMSE_{ELISA}$ in Figure 2.8 D were 0.0792 and 0.1117, respectively. The $RMSE_{SERS}$ and $RMSE_{ELISA}$ in Figure 2.8 E were 0.0956 and 0.1212, respectively. This suggests a strong linear relationship between the results of ELISA and SERS with virtually no outliers. The one exception was CD44 expression in MDA-MB-231, where the mean weight factor was slightly higher than the upper bounds. However, the error bars still overlapped with the upper bound in both Figure 2.8 D,E.

To assess the effects of the cell matrix (PBS and blood), the mean weight factor of SERS in blood was plotted against the mean weight factor of SERS in PBS (Figure 2.8 F). The black line was the identity line on which the SERS weight factors in PBS and in blood were equivalent to each other. The result showed that the 10 lowest expressing points were almost exactly on the identity line, indicating that the SERS measurement of cells suspended in blood was nearly identical to those cells suspended in PBS for lower expression levels. As expected, the correlation coefficient was very high, with $r = 0.993$. The corresponding p-value was extremely low, with $p = 4.7 \times 10^{-11}$. To quantitatively examine the agreement between the two sets, the RMSE was calculated between their weight factors and determined to be RMSE = 0.06203, a value that was low enough to distinguish between negative and positive marker expression for both sets. The HER2 expression in SK-BR-3 fell above the upper bound but still had error bars

that overlap (red lines). The highest expressed point, corresponding to CD44 expression in MDA-MB-231, fell off the identity line but still remained within the uncertainty bounds.

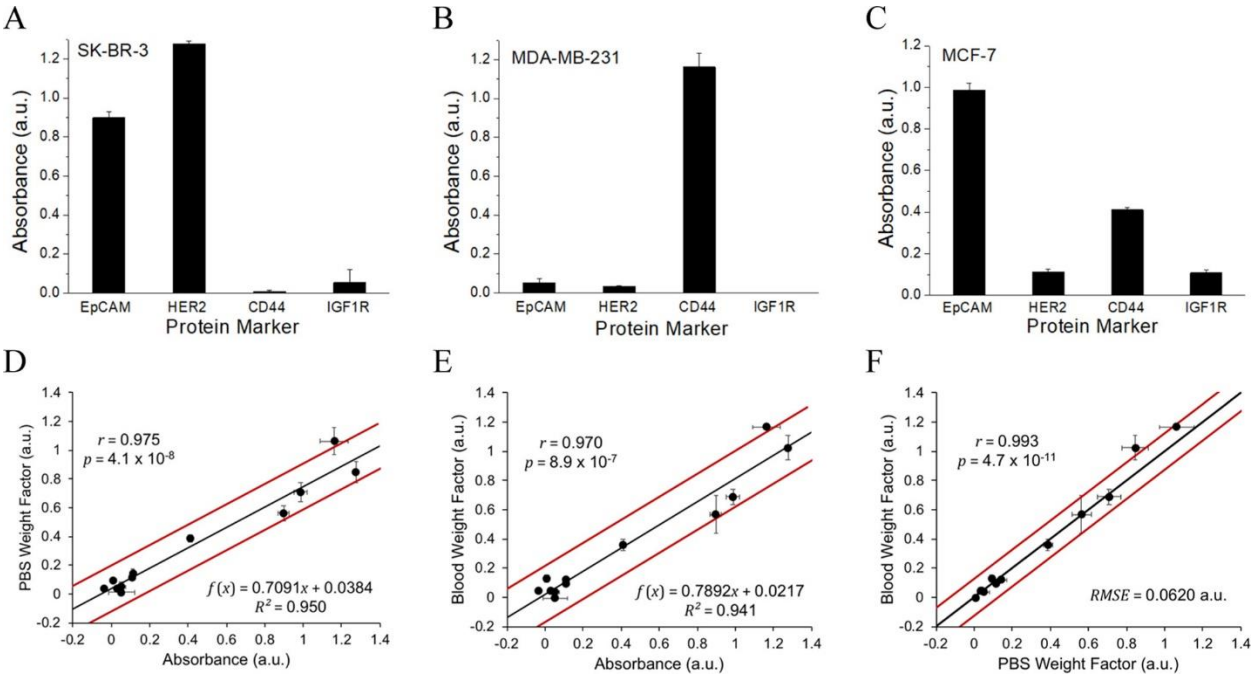

Figure 2.8 Correlation of multicolor SERS method with ELISA. (A–C) Expression level of surface protein markers of different cell lines with ELISA. (D,E) Plots of SERS mean weight factor as a function of the ELISA mean absorbance for SERS with cells in PBS (D) and with cells in blood (E). (F) Plot of the SERS mean weight factor with cells in blood as a function of the SERS mean weight factor with cells in PBS. The black line is the linear fit and the red lines represent the uncertainty bounds.

4. Conclusions

Using spiked cancer cells in blood to mimic CTCs, we have shown that CTCs can serve a dual purpose of isolation from human whole blood and detection with IO−Au core−shell SERS nanotags in a microfluidic device. By varying the Raman reporters and targeting ligands, four-color SERS nanotags targeting four different cancer markers were prepared. With the assistance

of CLS deconvolution, EpCAM, HER2, CD44, and IGF1R on single breast cancer cells were simultaneously detected. Using ELISA as the reference method, we showed that our method can accurately detect multiple cancer markers on different cell lines, suggesting that our method has the potential to simultaneously detect CTCs of multiple subpopulations in clinical samples. In our method, all cell isolation/enrichment, negative staining, optical imaging, SERS detection, and molecular profiling were performed on a microfluidic device. The microchip device increases the degree of operational automation, facilitates single-cell analysis, and reduces false negative signals by concentrating low-frequency tumor cells. We bridge the isolation and detection techniques with “all-in-one” IO−Au SERS nanotags, making the sample preparation simple and easy to operate. CTC identification is based on a combination of several parameters at the single-cell level. We used SERS for molecular cancer cell detection. We also used supplementary fluorescence imaging to recognize blood cell impurities and bright-field imaging to confirm cancer cells with morphological criteria. The combinatory criteria reduce false positives and ensure detection accuracy.

Chapter 3. OPTIMIZING CELLULAR BINDING OF LIGAND-CONJUGATED GOLD NANOPARTICLES

1. Introduction

Due to the intriguing surface plasmon resonance (SPR)-enhanced optical properties, gold nanoparticles (AuNPs) have attracted intense research interests for decades.[128-130] AuNPs absorb and scatter light orders of magnitude stronger than non-metallic NPs and individual organic dyes.[131] Under dark field light scattering imaging, AuNPs appears as bright fluorescence analogs.[132] Different from fluorescence dyes, AuNPs do not photo-bleach. AuNPs are highly efficient photothermal agents. The absorbed light can be converted to heat within picosecond.[133] Thus, AuNPs have been widely used for a variety of biomedical applications, including cancer imaging, spectroscopic detection, photothermal therapy, radiotherapy, and drug delivery.[2,134-137]

To use AuNPs effectively as diagnostics and therapeutic agents, AuNPs need specifically and sensitively bind to target of interests on cancer cells. A major important parameter is surface chemistry of the NPs. Targeting specific ligand, such as antibodies, peptide, oligonucleotide, and aptamer are generally chemically immobilized on to AuNPs. The most common method is through robust thiol chemistry. The ligand is either modified with a thiol linker to bind to AuNPs or through a heterofunctional linker that binds to AuNPs on one end and to the ligand on the other end. In addition, a protective agent, often polyethene glycol (PEG), is used to increase the stability of the conjugates. Literature has reported many different approaches for the formulation of the light-conjugated and PEG stabilized AuNPs. However, a systemic evaluation on the effect of ligand density and role of PEG on targeted cellular labeling are lacking.

Detection of target of interests on cancer cells has two ways, direct and indirect targeting. For the direct targeting. Ligand-conjugated AuNPs directly bind to cell surface markers or to antibodies that are bound to cells in advance. In the indirect method, primary antibodies bind to cells first, followed by secondary antibodies. The ligand-conjugated AuNPs recognize secondary antibodies. Compared to direct method, the indirect method requires the use of secondary antibody. But, it is flexible for detection of multiple surface markers as the primary antibody does not need chemical modification. For both studies, literature have reported the use of different matrix for the primary and second antibodies. Most studies use phosphate buffered solution (PBS) with 1-5% bovine serum albumin (BSA) that blocks nonspecific cellular binding of the antibodies. Other studies use low concentration of tween-20 to block nonspecific bindings. But, it is not clear what is the best binding conditions. A side-by-side comparison is needed to optimize cellular targeting and labeling.

In this study, we performed a systemic study on the effects of surface chemistry of ligand-conjugated AuNPs and the binding conditions to detect cancer cell surface protein markers. We use streptavidin (SA) as the protein ligand model. MDA-MB-231 breast cancer cells was used as the cancer cell model, with the high expression CD44 protein marker as the surface target. We examined both direct and indirect labeling method in which biotin was conjugated to primary antibody and secondary antibody, respectively. Using dark field imaging to examine the cellular binding, we have found optimal SA-AuNP formulation and the cellular binding conditions. The results will benefit many fundamental and applied research using ligand-conjugated AuNPs and other types of NPs.

2. Materials and Methods

2.1 Materials

All chemicals were purchased from Sigma-Aldrich (St. Louis, MO) unless specified. CD44 antibodies and biotin-CD44 antibodies were purchased from Biolegend (San Diego, CA). MDA-MB-231 cells were purchased from ATCC (Manassas, VA). Colloidal gold (50 nm in diameter) was purchased from Ted Pella (Redding, CA). Dulbecco's Modified Eagle Medium (DMEM) with high glucose (4.5 g/L), 0.25% trypsin, and 100 U/mL HyClone Penicillin-Streptomycin (P/S) were purchased from VWR (Atlanta, GA). Biotin-secondary antibodies, fetal bovine serum (FBS) and non-essential amino acids (NEAA) were purchased from Fisher Scientific (Waltham, MA). Streptavidin-thiol (SA-SH) was purchased from Nanocs (New York, NY).

2.2 Synthesis and characterization of SA-conjugated AuNPs

To 200 µL of as-purchased 50-nm AuNP solution (75 pM) in a non-stick plastic vial, 10 µL tween-20 in 20 mM 4-(2-hydroxyethyl)-1-piperazineethanesulfonic acid (HEPES) pH7 was added. Then, SA-SH was added with different loading SA-to-AuNP molar ratios from 0 to 10, 000. The solution was mixed via gentle vortexing for 1.5 h at RT. Then, 4.5 µL of 0.1 mM methoxyl-polyethenly glycol thiol (mPEG-SH) with molecular weight of 2000 or 5000 was added and mixed for another 1.5 h at RT. At the end, the solution was centrifuged (10,000 rpm, 10 min) and the conjugates were resuspended in 300 µL of phosphate buffered solution (PBS) containing 0.05% (w/v) tween-20. This process was repeated for two more times. The final conjugates were resuspended in 200 µL PBST0.05% with 0.05% (w/v) sodium azide and stored at 4^{o}C before use.

2.3 Cell Culture

MDA-MB-231breast cancer cells were cultured in DMEM with 10% fetal bovine serum, 1% NEAA, 100 U/mL penicillin, and 0.1 mg/mL streptomycin at 37°C with 5% CO_2. To label surface protein markers, cells were cultured in an 8-well chamber slide of 5 x 10^4 cells/well for 72 h.

2.4 Indirect detection of cell surface protein markers with SA-conjugated AuNPs

MDA-MB-231 cells cultured in an 8-well chamber slide were washed with PBST0.05% and fixed with 1% formaldehyde at room temperature (RT) for 15 min. The cells were blocked with 1% BSA for 30 min at 37ºC, followed by two times washing with PBS. Then, the cells were incubated with 150 µL of 5 µg/mL CD44 antibodies (CD44-Ab1) diluted in PBS, PBS with 1% BSA, or in PBST0.05% for 1 h at 37ºC. After washing three times with PBST0.05%, the cells were incubated with 150 µL of 5 µg/mL biotin-secondary antibodies (biotin-Ab2) diluted (1:60) in PBS, PBS with 1% BSA or PBST0.05% for 1 h at 37ºC. After washing three times with PBST0.05%, the cells were incubated with 150 µL of 20 pM of SA-AuNP conjugates with different SA-to-AuNP loading ratios from 0 to 10,000 in PBS with 0.1% BSA, PBS with 1% BSA or PBST0.05% for 1 h at 37ºC. The cells were washed three times with PBST0.05% followed by two times washing within PBS before imaging. The experiments without using CD44-Ab1 were performed as the negative controls.

2.5 Direct Detection of Cell Surface Protein Markers with SA-conjugated AuNPs

MDA-MB-231 cells cultured in an 8-well chamber slide were washed with PBST0.05% and fixed with 1% formaldehyde at room temperature (RT) for 15 min. The cells were blocked with 1% BSA for 30 min at 37ºC, followed by 2 times washing with PBS. Then, the cells were

incubated with 150 µL of 5 µg/mL biotin-CD44 Ab1 diluted in PBS, PBS with 1% BSA, or in PBST0.01% for 1 h at 37^{o}C. After washing three times with PBST0.05%, the cells were incubated with 150µL of 20 pM of 5K SA-AuNP conjugates diluted in PBST0.05% for 1 h at 37^{o}C. The cells were washed three times with PBST0.05% followed by two times washing within PBS before imaging. The experiments without using biotin-CD44 Ab1 were performed as the negative controls.

2.6 Characterization of SA-conjugated AuNPs and Their Cellular Binding

Size and zeta potential of the conjugates were measured by dynamic light scattering (DLS) using a Zetasizer Nano ZS (Malvern Instruments). Absorption spectra were measured with an UV-Vis absorption spectrometer (Shimadzu Scientific Instruments). Cellular binding of the SA-conjugated AuNPs were characterized by dark field imaging using an Olympus IX71 inverted microscope with a 40x objective.

3. Results and Discussion

3.1 Design of the Studies

Cellular targeting and imaging are usually done in two different ways, direct and indirect detections (Figure 3.1). In direct detection, the labeling agent is directing the primary antibodies. In indirect method, the labeling agent is detecting secondary antibody that recognizes the primary antibodies. Compared to the direct method, the indirect method has one more step, but there is no need of chemical modification of the primary antibody. This is advantageous in efficiency for detecting multiple surface markers.

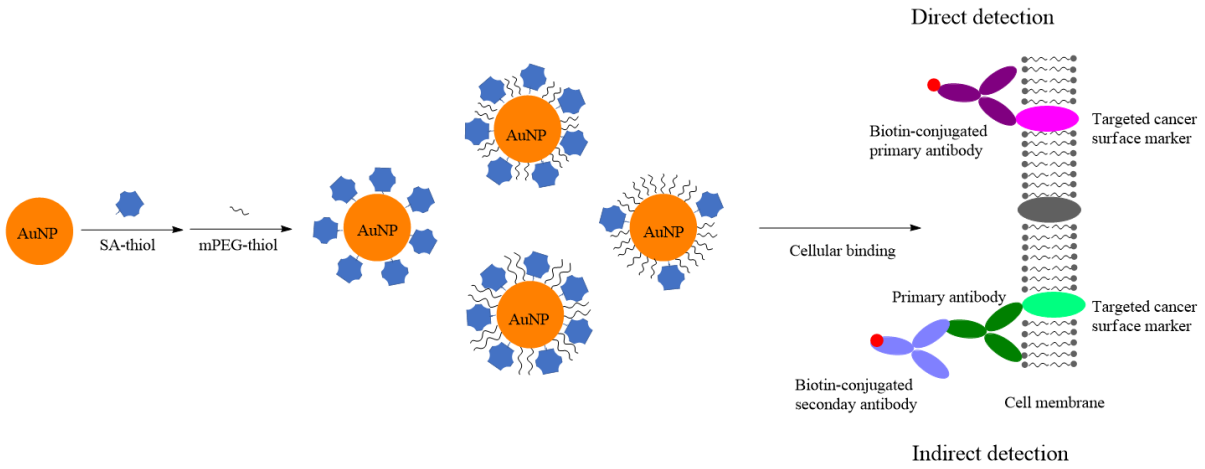

Figure 3.1. Schematic of the preparation of SA/AuNPs with different formulations for cancer marker detection. SA-thiol is bound to AuNPs via Au-S bond. A series of formulations are formed by varying the surface density of SA and subsequent binding with mPEG-SH with different molecular weight. Cellular binding were tested in two different approaches, direct binding with biotin-conjugated primary antibody and indirect binding with biotin-conjugated secondary antibody.

To investigate the two targeting methods, we make use of the high affinity and high specificity streptavidin-biotin binding. We functionalize AuNPs with streptavidin. In the direct method, we use commercially available biotin-conjugated antibodies. The biotin-conjugated antibodies bind to targeted surface protein marker on cells and then recognized by SA-conjugated AuNPs. In the indirect method, targeted surface markers are recognized by primary antibody. Then, the primary antibody was recognized by biotin-conjugated secondary antibody. Lastly, the biotin-conjugated secondary antibody is recognized by SA-conjugated AuNPs. To detect AuNPs, we use dark field imaging to. Due to their intense localized surface plasma resonance (LSPR), AuNPs exhibit strong light-scattering properties.[128,138] Thus, AuNPs can be easily detected under dark field, which makes them attractive fluorescence analogs for biomedical imaging via dark field light scattering imaging with a regular optical microscope.[130,139]

Surface chemistry determines the binding affinity and specificity of AuNPs. To investigate the effect of surface chemistry, we made SA-conjugated AuNPs with different surface density of SA. We also examine the role of stabilizing PEG by making the SA-conjugated AuNPs without PEG and without PEG. The effect of the size of PEG is examined by varying the molecular weight and thus the chain length of PEG. We use MDA-MB-231 breast cancer cells as the model to examine cellular binding. CD44, a high expression cancer marker on MDA-MB-231 cells, was used as the surface protein target.

3.2 Synthesis of SA-conjugated AuNPs

SA-conjugated AuNPs were prepared by reacting SA-SH with bare AuNPs with different SA to AuNP loading molar ratios via constant mixing for 1.5 h at RT in a centrifuge 1.5 mL vial. To minimize the adsorption of protein-bound AuNPs to the plastic vial, the reaction was performed in 1% v/v tween-20. To prevent the aggregation of AuNPs, the reaction was performed in 20mM pH7.0 HEPES buffer. Then, the SA-conjugated AuNPs was followed by PEGylation or directly purified by centrifugation. We use excessive PEG-SH2K or PEG-SH5K (30,000:1 = PEG: AuNP) to saturate the surface of the SA-conjugated AuNPs. The final conjugates were purified by centrifugation and washing with PBST0.05%. Again, tween-20 was used during washing steps to minimize the adsorption of the conjugates to the plastic vials. The conjugates were stored in PBST0.05% with 0.05% (w/v) sodium azide. Alternatively, the conjugates can be stored in low-protein binding vial (Fisher Scientific) in PBS without tween. It is worthy to note that the protein-bound AuNPs were heavily adsorbed to plastic vials without tween-20 during the reaction or storage. So, tween-20 is critically important in preparation, handling, and storage of protein-functionalized NPs unless low-protein binding vials were used.

3.3 Characterization of SA-conjugated AuNPs

The SA-conjugated AuNPs were characterized by DLS and absorption spectroscopy for hydrodynamic size and LSPR, respectively (Table 3.1, Figure 3.2). It is very interesting to note that the hydrodynamic size varies before and after centrifugation-based purification depending on the surface chemistry. Figure 3.2 A&B show the hydrodynamic sizes of SA/mPEG-SH2K/AuNPs with different SA to AuNP loading ratios before and after centrifugation. The bare AuNPs is 48.5 nm. Before centrifugation The AuNPs modified with mPEG-SH2K only, the conjugates were 50.5 nm before centrifugation and 63.5 nm after centrifugation. This revealed that the centrifugal force changed the conformation of PEG, leading to increased thickness of the polymer layer on the surface of AuNPs. After centrifugation, the thickness of mPEG-SH was about 6 nm.

Table 3.1: Characterization of the particle size of purified SA-conjugated AuNPs

	Hydrodynamic size (nm)
Bare AuNPs	48.5
mPEG2k/AuNPs	63.5
mPEG5k/AuNPs	74.6
0.25k SA/mPEG2k/AuNPs	78.7
0.6k SA/mPEG2k/AuNPs	95.0
1k SA/mPEG2k/AuNPs	108.4
2k SA/mPEG2k/AuNPs	84.5
5k SA/AuNPs	60.3
5k SA/mPEG2k/AuNPs	67.4
5k SA/mPEG5k/AuNPs	64.9
8k SA/mPEG2k/AuNPs	60.1
10k SA/mPEG2k/AuNPs	59.0

The size of AuNPs at 1.5 h after SA addition increased with increasing SA-to-AuNP loading ratio from 55 nm for 0.25k SA/mPEG/AuNPs to 65.2 nm for 10k SA/mPEG/AuNPs. After mPEG-SH saturation and centrifugation, the size of the conjugates changed depending on the SA to AuNP loading ration (Figure 3.2 C&D).

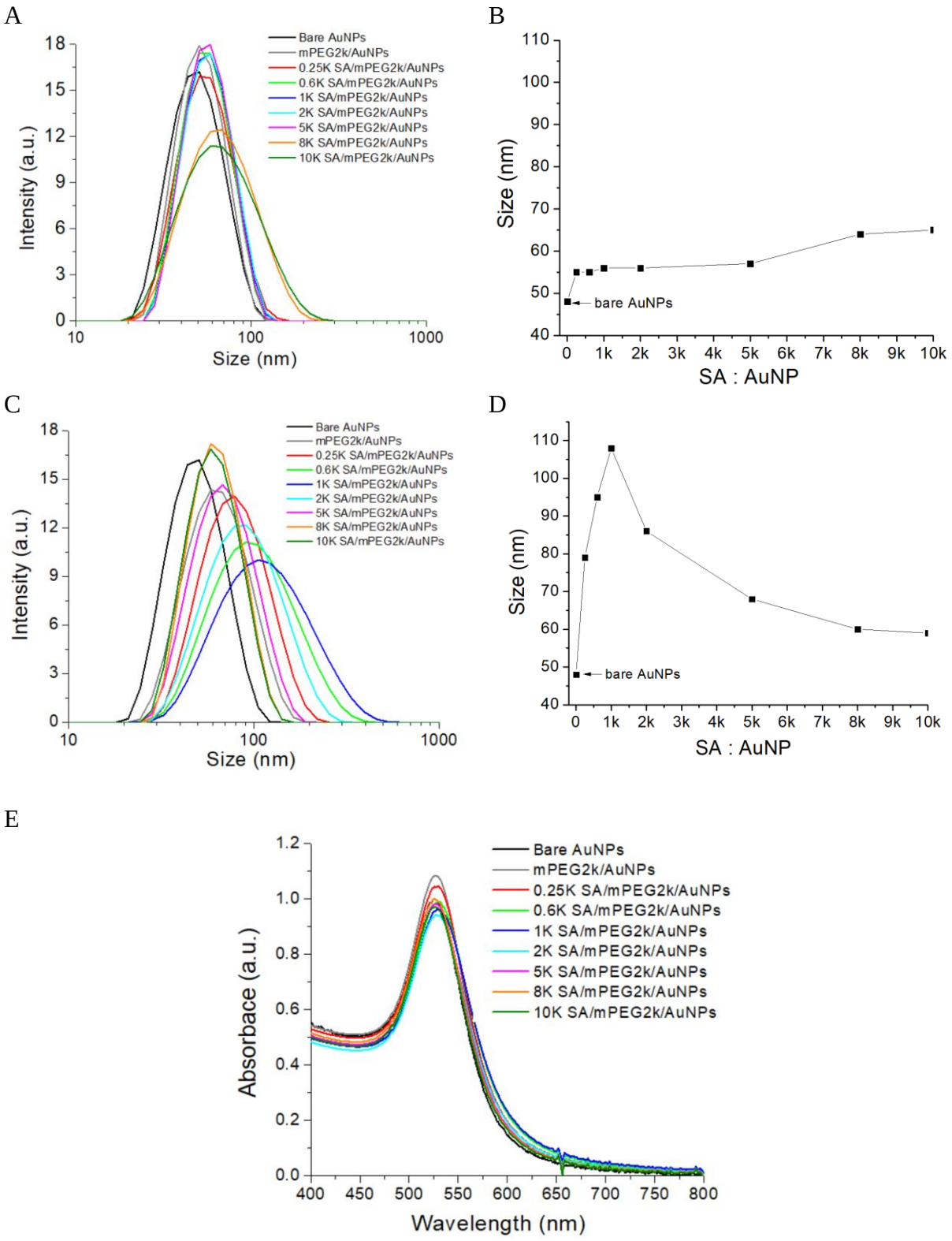

Figure 3.2. Characterization of SA-AuNPs with different SA to AuNP loading ratios. (A)&(B) Hydrodynamic size before addition of mPEG-SH 2K and purification. (C)&(D) Hydrodynamic size after mPEG-SH addition and purification. (E) Absorption spectra.

When the SA to AuNP ratio increased from 0.25k to 1k, the size increased from 78.7 nm to 108. 4nm. However, continuous increasing of the SA to AuNP ratio from 1k to 8k decreased the size of the SA/mPEG/AuNPs from 108.4 nm to 60.1 nm. Further increasing of the SA-to-AuNP ratio to 10k did not significantly decrease the size of the particles. Based on the size of bare AuNPs (48.5 nm) and SA (~ 5 nm), we estimate that SA/AuNPs should be ~ 59 nm. The mPEG2k/AuNPs was 63.5 nm. So, the size of SA/mPEG2K/AuNPs should be between 58 to 64 nm. The conjugates with 8k and 10k SA to AuNP loading ration fell within this range and thus they were monodisperse NPs. The conjugates with significantly larger size, including 0.25k, 0.6k, 1k, and 2k/mPEG/AuNPs were thus aggregated. Figure 3.2 E shows the absorption spectra of the AuNPs at 1.5 h after SA addition. The results show that there were no significant change on the LSPR wavelength after SA addition. This also suggests the SA binding was performed without aggregation.

3.4 Effect of SA-to-AuNP Loading Ratio to Cellular Binding

Figure 3.3 shows the dark field images of CD44 targeting MDA-MB-231 cells after labeled with SA/mPEG2k/AuNPs by the indirect method. In this study, CD44 primary antibody was diluted in PBS and biotin-secondary antibody was diluted in 1% BSA. SA/mPEG2K/AuNPs with varied SA-to-AuNP loading ratios were diluted in PBST0.05%. The negative control was the experiment without CD44 primary antibody. The results show that 5k SA/mPEG2K/AuNPs and 10k SA/mPEG2K/AuNPs bound to the cells very well, which was indicated by high density green scattering AuNPs. The 0.25k SA/mPEG2K/AuNPs barely bound to the cells. There were some aggregated NPs (shown as red aggregates) for the 0.6k SA/mPEG2K/AuNPs. More particles were found on the cells from 2k SA/mPEG2K/AuNPs compared to 0.25k and 0.6k SA/mPEG2K/AuNPs. The negative controls for all formulations did not bind to the cells. These

studies showed that cellular binding of SA/mPEG2K/AuNPs depends on ligand density, with higher ligand leading to better cellular binding. To achieve effective cellular labeling without particle aggregation, a SA-to-AuNP loading ratio of 5000 or higher is needed to make specificity and sensitive monodisperse SA/mPEG2k/AuNPs.

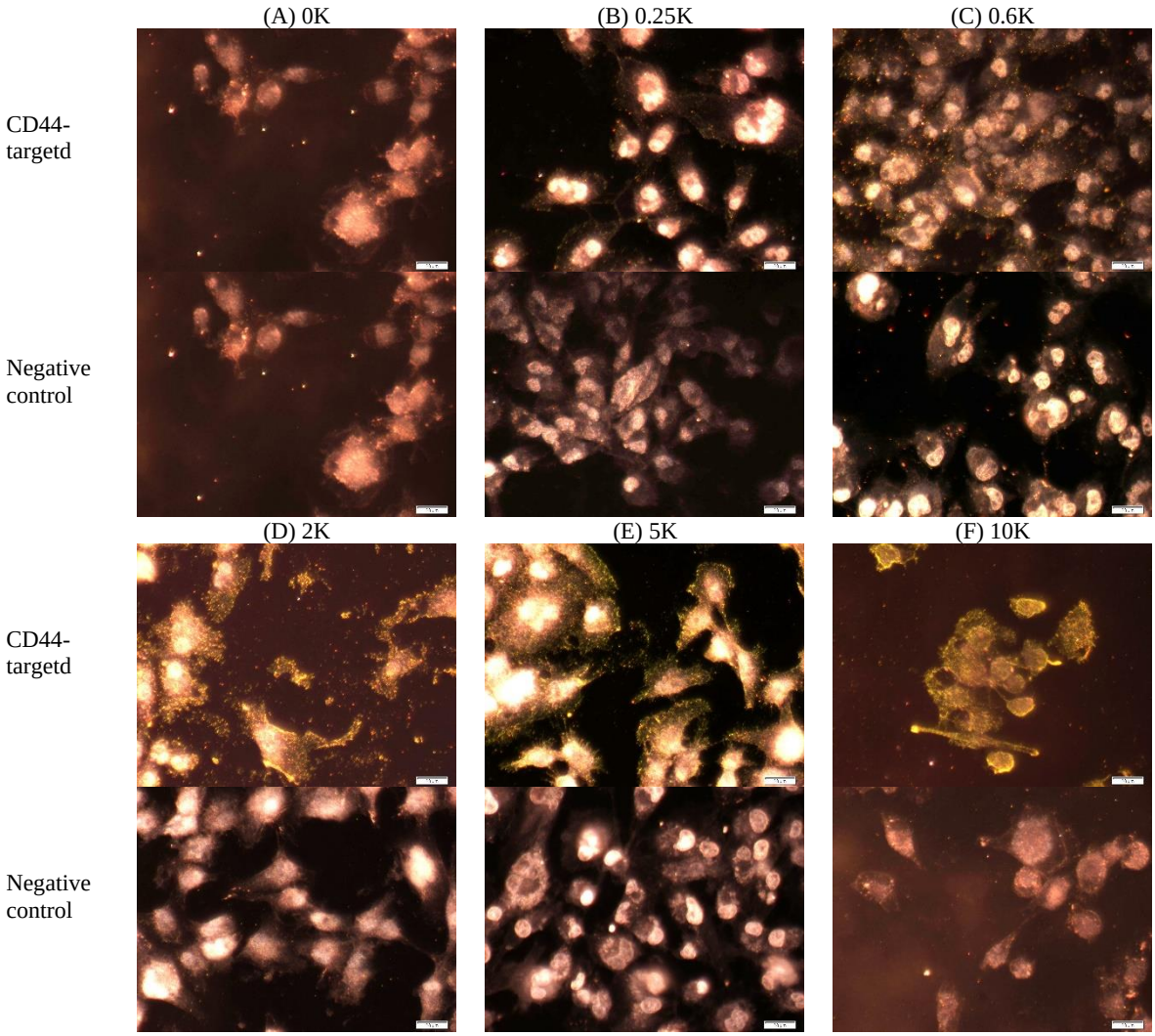

Figure 3.3. Examining the effect of SA loading ratio on the cellular binding of AuNPs. CD44 primary antibody was diluted in PBS and biotin-secondary antibody was diluted in 1% BSA. SA/mPEG2K/AuNPs with varied SA to AuNP loading ratios were diluted in PBST0.05%. CD44 on MDA-MBA-231 cells was used as the surface marker target. Negative control was the treatment without CD44 Ab1.

3.5 Effect of Binding Matrix of Primary and Secondary Antibody to Cellular Binding

Figure 3.4 shows dark field images of CD44-targeting MDA-MB-231 cells when using primary and secondary antibody in three different matrix, PBS, PBS with1% BSA and PBS with 0.05% tween-20. The results show that when CD44 primary antibody (CD44-Ab1) suspended in PBST0.05% showed best binding, followed by PBS with 1% BSA, and PBS only. For the secondary antibody, the biotin-secondary antibody (biotin-Ab2) showed best binding among the three matrices, although all three showed good bindings. The negative controls for all cases did not bind to the cells, indicating excellent specificity of the primary and secondary antibodies. These studies suggest that suspension of combination of primary antibody in PBST0.05% and secondary antibody in PBS with 1% BSA gave the best cellular binding than other binding matrices.

3.6 Effect of Binding Matrix of SA-conjugated AuNPs to Cellular Binding.

Figure 3.5 shows dark field images of CD44-targeting MDA-MB-231 cells when SA-conjugated AuNPs were suspended in PBS with 0.1% BSA, 1% BSA, and tween-2 0.05%. In this study, 5K SA/mPEG2K/AuNPs were used as the model conjugate. The results showed that the 5K SA/mPEG2K/AuNPs suspended in PBST0.05% showed highly specific and efficient binding to the cancer cells. In contrast, heavy nonspecific binding of the conjugates in PBS with 0.1% or 1% BSA to the chamber slide were found. In addition, the NPs aggregated with the presence of BSA. This is most likely due to the biotin impurity in the commercial BSA. It is known that the purity of BSA varies based on the commercial resources. Most BSA contains biotin impurity. Thus, for the use of SA-conjugated AuNPs, biotin-free BSA is needed to avoid NP aggregation.

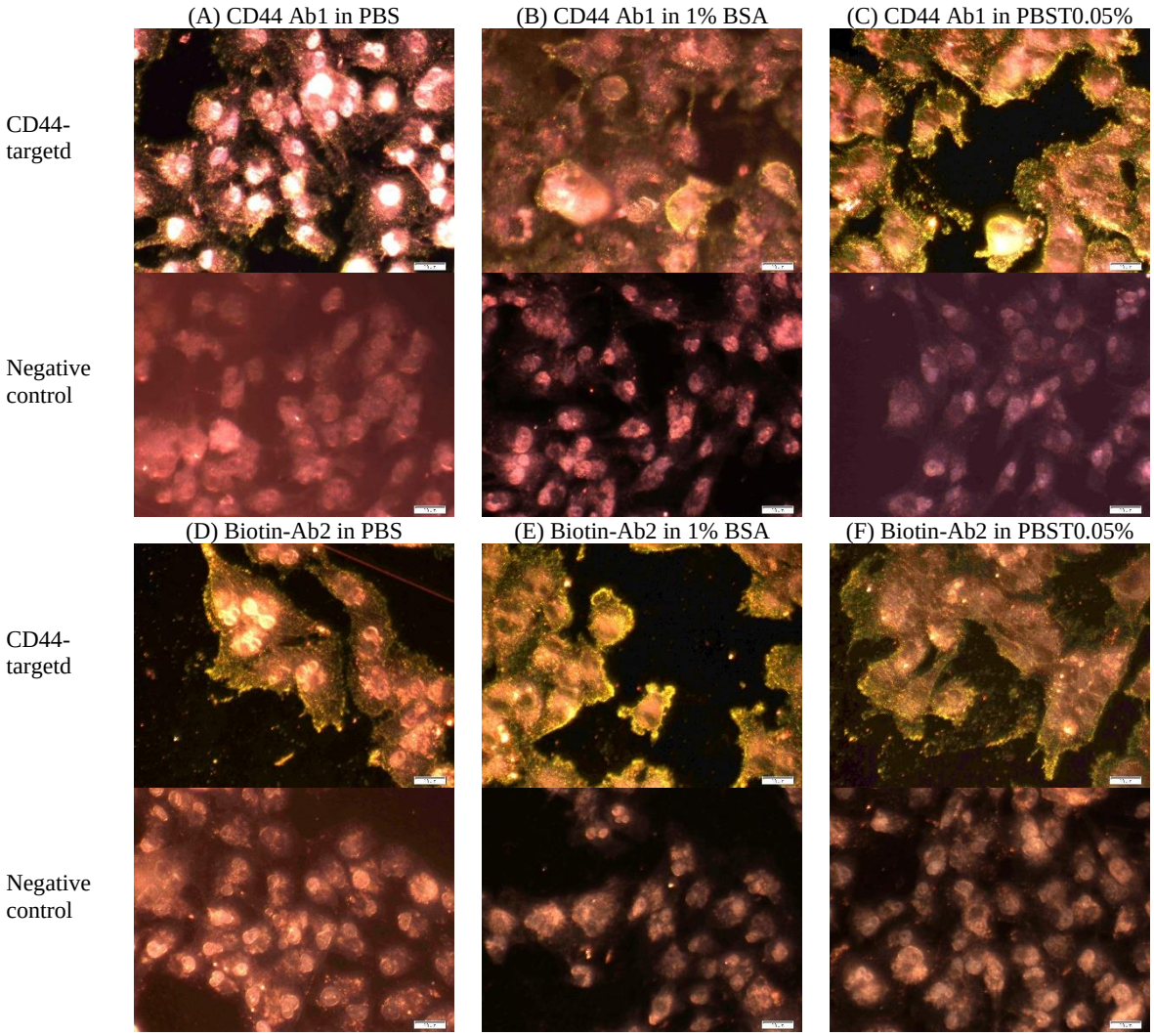

Figure 3.4. Examining the effect of different matrix on cellular binding of the primary and secondary antibodies with SA-conjugated AuNPs. (A-C) CD44 Ab1 was diluted in PBS (A), 1% BSA (B), and PBST0.05% (C). Biotin-Ab2 was diluted in PBST0.05%. (D-F) Biotin-Ab2 was diluted in PBS (D), 1% BSA (E), and PBST0.05% (F). CD44 Ab1 was diluted in PBST0.05%. In all cases, SA/mPEG-SH2k/AuNPs (SA: AuNP = 10K:1) were diluted in PBST0.05%. CD44 on MDA-MBA-231 cells was used as the surface marker target. Negative control was the treatment without CD44 Ab1.

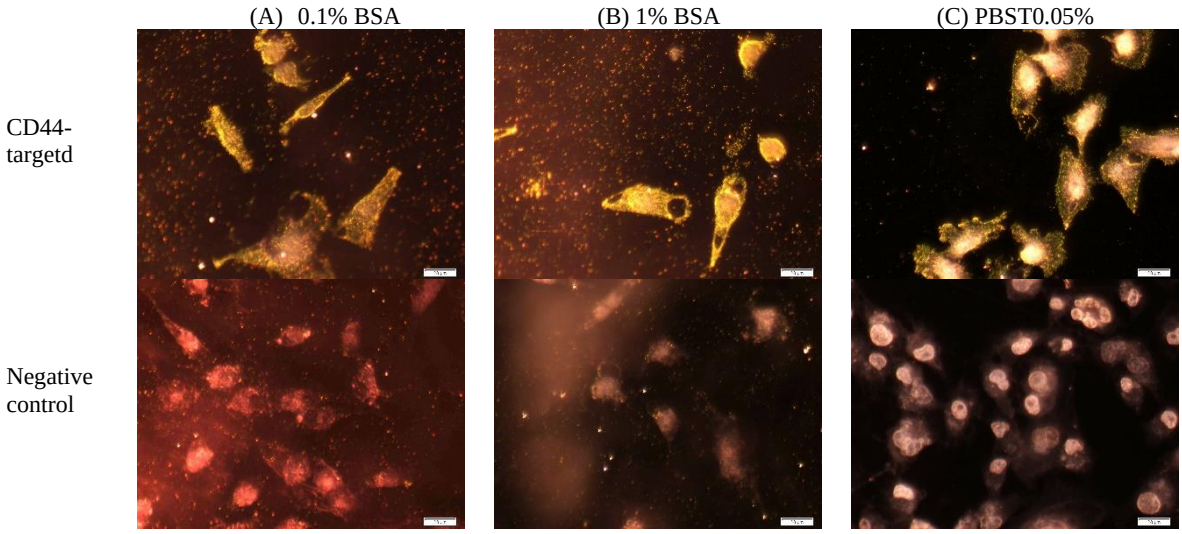

Figure 3.5. Examining the effect of different matrix on the cellular binding of SA-conjugated AuNPs. SA/mPEG-SH2k/AuNPs (SA:AuNP = 5K:1) were diluted in 0.1% BSA (A), 1% BSA (B) and PBST0.05% (C). CD44 Ab1 was diluted in PBS and biotin-Ab2 was diluted in 1% BSA. CD44 on MDA-MBA-231 cells was used as the surface marker target. Negative control was the treatment without CD44 Ab1.

3.7 Effect of Binding Matrix of Biotin-conjugated Primary Antibody to Cellular Binding in the Direct Method

The studies discussed above all used the indirect detection method. For the direct method, only biotin-CD44 Ab1 is used. Figure 3.6 shows the effect of matrix for suspension of the biotin-CD44 Ab1 to cellular binding. Both PBS with 1% BSA and PBST0.05% gave highly efficient binding. The PBS showed lower amount of AuNPs than PBS with 1% BSA or 0.05% tween-20. In the indirect method, PBST0.05% showed best binding than other matrix (Figure 3.4). Thus, primary antibody diluted in PBST0.05% is recommended for both direct and indirect method for cellular labeling.

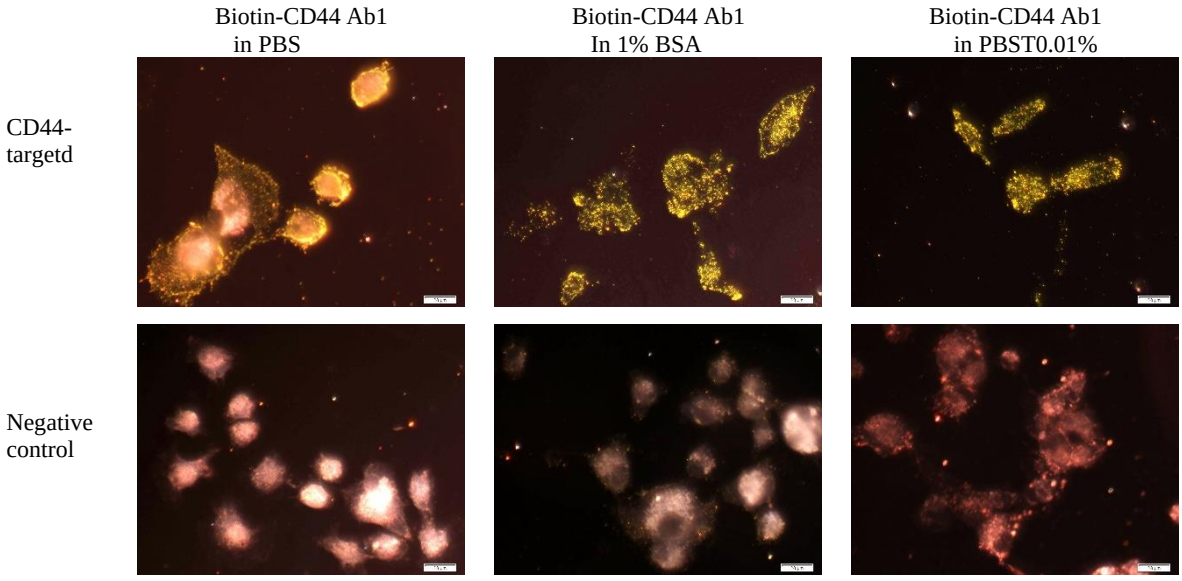

Figure 3.6. Examining the effect of different matrix on the biotin-conjugated primary antibodies with SA-conjugated AuNPs. CD44-biotin was diluted in PBS, 1% BSA, and PBST0.01%. SA/mPEG-SH2k/AuNPs (SA: AuNP = 5K:1) were diluted in PBST0.005%.

3.8 Effect of PEG Stabilizer on the Cellular Binding of SA-conjugated AuNPs

To examine the effect of PEG on the cellular binding of the SA-conjugated AuNPs, we made the conjugates with SA only (SA/AuNPs), with both SA and mPEG-SH 2k (SA/mPEG2k/AuNPs), and with both SA and mPEG-SH5k (SA/mPEG5k/AuNPs), in which SA-to-AuNP ratio was 5000. Figure 3.7 A-C shows the hydrodynamic size before and after centrifugation. Again, centrifugation led to an increase of the size of the conjugate when PEG was used. For the SA/AuNPs, there was no effect on the particle size by centrifugation. The size of the SA/AuNPs was about 59 nm, suggesting the thickness of SA on the particle surface was approximately 5 nm. For the purified particles, the size of mPEG5k/AuNPs was 74.6 nm, which is nearly 10 nm larger than the mPEG2k/AuNPs and 25 nm larger than the bare AuNPs. Compared to SA/AuNPs, the sizes of SA/mPEG2k/AuNPs and SA/mPEG5k/AuNPs increased by 7 nm and 5 nm, respectively. It is interesting to note that there is no significance difference in

the particle size for the SA/mPEG2k/AuNPs and SA/mPEG5k/AuNPs. Thus, the PEG chain length did not affect significantly the overall size of the protein conjugates, although it changes dramatically the size of AuNPs with PEG modification only.

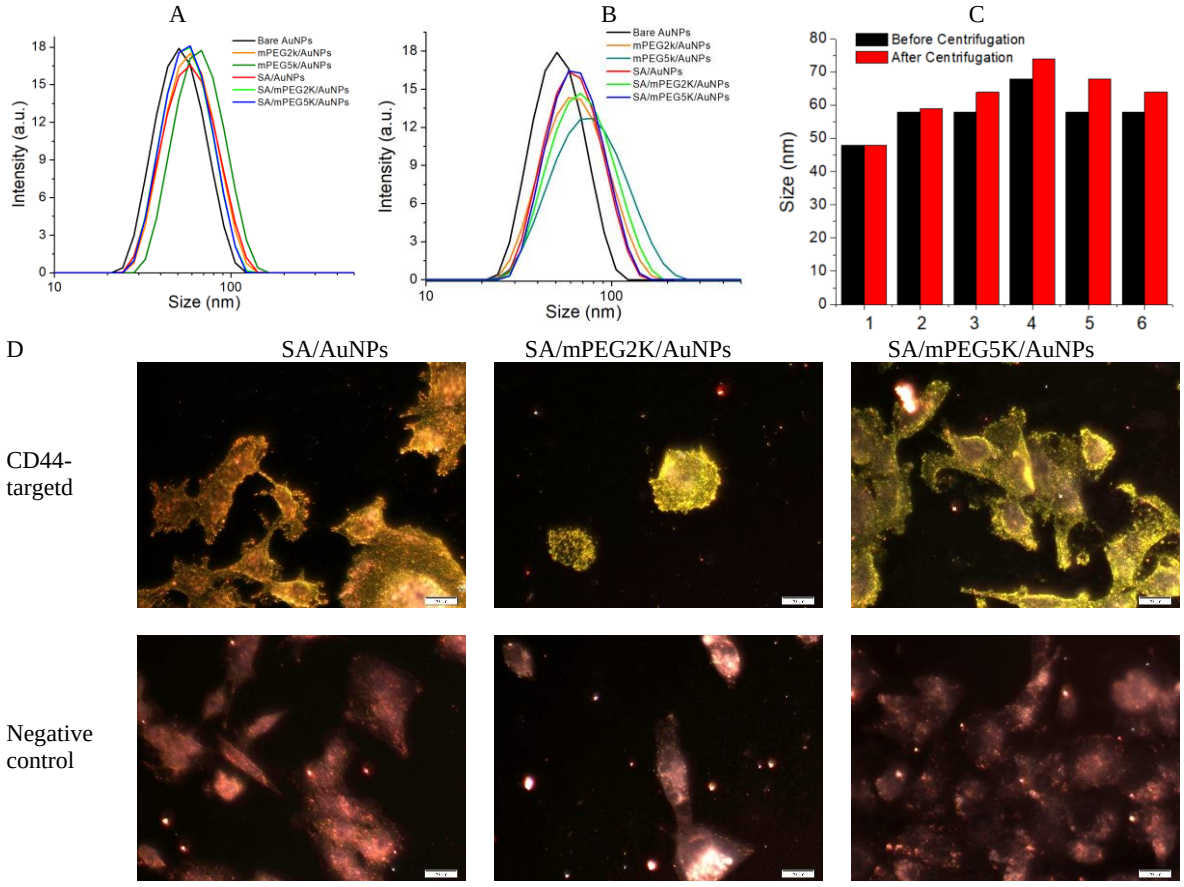

Figure 3.7. Examining the effect of the size of mPEG-SH stabilizer on the cellular binding of SA-conjugated AuNPs. CD44-biotin was diluted in PBST0.01%. SA:AuNP = 5K:1. (A) Hydrodynamic size before purification by centrifugation. (B) Hydrodynamic size after purification by centrifugation. (C) comparison of the size for different formulations before and after purification by centrifugation. 1: bare AuNPs (both red and black plots are the size of AuNPs without centrifugation). 2: SA/AuNPs. 3: mPEG-SH2k/AuNPs. 4: mPEG-SH5k/AuNPs. 5: SA/mPEG-SH2K/AuNPs. 6: SA/mPEG-SH5K/AuNPs. (D) Dak field images of MDA-MB-231 cells targeting CD44 marker (top row) using SA/AuNPs (left column), SA/mPEG-SH2k/AuNPs (middle column), and SA/mPEG-SH5k/AuNPs (right column) with their controls (bottom row).

Figure 3.7 D shows the dark field images of CD44-targeting MDA-MB-231 cells labeled with SA/AuNPs, SA/mPEG2k/AuNPs, and SA/mPEG5k/AuNPs. The results show that both SA/mPEG2k/AuNPs and SA/mPEG5k/AuNPs showed high bindings to the cells. The SA/AuNPs showed lower binding than SA/mPEG2k/AuNPs and SA/mPEG5k/AuNPs. This study suggests that PEGylation helps cellular binding of SA-conjugated AuNPs regardless of the polymer chain length.

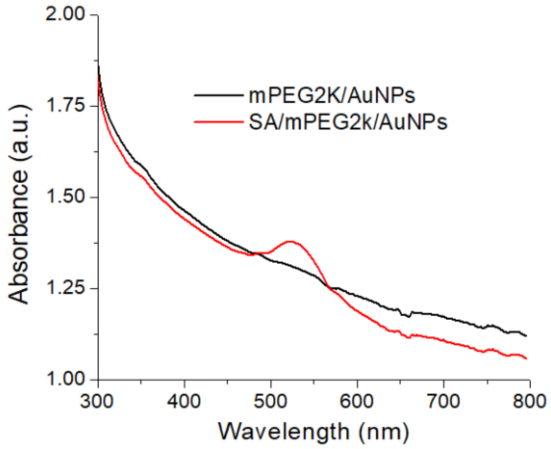

Figure 3.8. Absorption spectrum of CD44-targeting MDA-MB-231 cells after incubation with mPEG-SH2k/AuNPs (black curve) and SA/mPEG2k/AuNPs (red curve). The presence of absorption peak around 528 nm suggestions the binding of SA/mPEG2k/AuNPs to the cancer cells.

The presence of the AuNPs on the cells were further confirmed by absorption spectrum (Figure 3.8). Using the 5k SA/mPEG2k/AuNPs as the example, we measured the absorption spectrum in comparison to mEG2k/AuNPs. The LSPR peak of AuNPs around 528 nm suggests the binding of the conjugates on the cells.

4. Conclusion

Using SA-conjugated AuNPs, we have shown that cellular labeling largely depends on the surface chemistry of the particles and the matrix of the binding agents. For the SA-conjugated AuNPs, SA-to-AuNPs loading ratio of 5000 or higher is needed to make stable and monodisperse conjugates for efficient labeling. The conjugates with PEG stabilization were better than that without PEG. However, the molecular weight of PEG did not play an important role. SA-conjugated AuNPs stabilized with mPEG-SH 2000 or 50000 showed similar cellular binding. Tween or BSA was needed to dilute the primary antibody or secondary antibody to achieve good cellular labeling, with PBST showing better cellular binding than BSA. To dilute SA-conjugated AuNPs, BSA caused particle aggregation, probably due to biotin impurity in BSA. Similar to primary or secondary antibody, the PBST0.05% is the best matrix for SA-conjugated AuNPs.

It is realized that the optimized SA-AuNP formulation and binding conditions are concluded from *in vitro* study alone. For *in vivo* application, other factors need to be considered, including stability in blood, organ biodistribution, and tumor uptake. In addition, this study using spherical nanoparticles as the model. Anisotropic nanoparticles may differ slightly in terms of ligand density. Thus, future studies with animal models are needed to achieve best protein-nanoparticle conjugates for in vivo applications.

Chapter 4. DEVELOPMENT OF A GOLD NANOPARTICLE-ENHANCED ENZYME-LINKED IMMUNOSORBENT ASSAY FOR DETECTION OF ANTIBODIES AGAINST SARS-COV-2 SPIKE PROTEIN

1. Introduction

The ongoing coronavirus pandemic (COVID-19) is caused by a pathogen named severe acute respiratory syndrome coronavirus 2 (SARS-CoV-2) first reported in Wuhan, China in 2019.[140-142] Since its onset, the disease has inflicted over 230 million people and caused nearly 5 million deaths worldwide.[143] SARS-CoV-2 belongs to the same family of coronaviruses as severe acute respiratory syndrome coronavirus (SARS-CoV) and Middle East respiratory syndrome coronavirus (MERS-CoV).[144] The viral particle is spherical in shape and spans 125 nm in diameter; it includes a single stranded RNA genome and four structural proteins consisting of a spike protein, membrane protein, envelope protein, and nucleocapsid protein.[145] The spike protein plays a critical role in granting entry of the virus into the host cell by interacting with cell receptors like the angiotensin converting enzyme 2 (ACE-2).[146] The spike protein's prominent location outside the viral particle and its critical role in gaining entry of the virus into the host cell make it an effective target for an immune system response.[147]

The standard method for detecting active COVID-19 cases is by amplifying and detecting viral RNA using real-time reverse-transcriptase polymerase chain reaction (RT-PCR) techniques. To detect SARS-CoV-2 RNA, samples must be obtained from a nasal or pharyngeal swab, or less commonly a bronchoalveolar lavage sample, as the virus is known to infect the lower respiratory tract. [141,148-150] RT-PCR-based detection is an established method that offers high-throughput screening, superior sensitivity, and high selectivity. In addition, it is a useful technique for clinics in discerning active viral cases. However, this detection method does

present some limitations including a potentially lengthy wait time for results that can span days to weeks.[151] Another limitation is that equipment required for high-throughput RT-PCR detection must generally be housed in large laboratory facilities. Furthermore, although RT-PCR is a valuable resource in determining active SARS-CoV-2 cases, this information must be supplemented with serological testing to determine seroprevalence, evaluate candidates for monoclonal antibody drugs, as well as to monitor vaccine response.[152-154]

Serological tests may be used to detect SARS-CoV-2-specific IgG and IgM antibodies and are considered valid confirmations of infection.[155] These tests typically include techniques such as lateral flow assay, chemiluminescent assays, and enzyme-linked immunosorbent assay (ELISA). It has been shown that IgM response to SARS-CoV-2 is detectable in the beginning stages of infection, crossing the detection threshold at day 4 and peaking near day 20 in one study.[156] The immune system's IgG response is delayed compared to IgM response, as IgM provides early-stage viral protection and IgG response is dedicated to long-term immunity and immunological memory.[157] In addition to detecting infection, serological testing will be critical in gauging SARS-CoV-2 vaccine efficacy, especially for populations experiencing an immunosuppressive illness or undergoing immunosuppressive treatment.[158,159] A focus on developing fast, reliable, economical, and sensitive immunoassays will be of great aid as we continue to combat the SARS-CoV-2 pandemic.

ELISA is a standard immunoassay capable of detecting and quantifying biological analytes in a variety of sample matrices.[160] In addition to being an agile method, it is also a sensitive one capable of routinely detecting sub-ng/mL analyte concentrations.[161] Since ELISA is such an established and reliable platform, there have been many important efforts using the ELISA scheme to design novel, ultra-sensitive assays.[162-164] In this study, we endeavor to

demonstrate a gold nanoparticle (AuNP) enhanced ELISA method for detecting SARS-CoV-2 spike protein IgG antibodies. We combine the reliability of the ELISA scheme with the unique properties of AuNPs, like a high surface-to-volume ratio and facile surface modification, that afford our method significantly improved enhancement over standard ELISA. We first optimize a sandwich ELISA method for specific and effective capture of SARS-CoV-2 spike protein antibody. This is followed by the design and optimization of anti-IgG/HRP-conjugated AuNPs for specific and sensitive detection of spike protein antibodies without sacrificing the speed and reliability of standard ELISA.

2. Materials and Methods

2.1 Materials

All reagents were purchased from Sigma-Aldrich (St. Louis, MO) unless otherwise specified. Goat anti-mouse IgG/HRP and mouse anti-human CD44 were purchased from Biolegend (San Diego, CA). SARS-CoV-2 spike protein S1 subunit and SARS-CoV-2 spike protein S1 subunit IgG antibody were purchased from R&D Systems (Minneapolis, MN). Thiolated methoxy polyethylene glycol (mPEG-SH, MW = 5000) and thiolated polyethylene glycol *N*-hydroxy succinimide (HS-PEG-NHS, MW = 1000) were purchased from Nanocs (Natick, MA). Dulbecco's modified Eagle's medium (DMEM) with high glucose (4.5 g/L), 0.25% trypsin, 100 U/mL HyClone penicillin–streptomycin (P/S), and TMB Plus Liquid 1-Component substrate were purchased from VWR (Atlanta, GA). Fetal bovine serum (FBS), nonessential amino acids (NEAA), beta-propiolactone (BPL) and bovine serum albumin (BSA) were purchased from Fisher Scientific (Waltham, MA). Gold colloid nanospheres 80 nm were purchased from BBI solutions (Portland, ME). MDA-MB-231 cell line was purchased from

ATCC (Manassas, VA). Human blood plasma was isolated from whole blood from healthy donors purchased from Research Blood Components (Watertown, MA).

2.2 Cell Culture

MDA-MB-231 breast cancer cells were cultured in DMEM with 10% FBS, 1% NEAA, 100 U/mL penicillin, and 0.1 mg/mL streptomycin at 37 °C with 5% CO_2. For ELISA experiments, cells were cleaved from culture dishes using trypsin solution, purified, and 2000 cells per well (in 50 μL medium) were plated in a 96-well cell culture plate and incubated for 24–48 h at 37 °C with 5% CO_2.

2.3 Identifying a Compatible Virus Inactivation Method

BPL and formaldehyde (FA) were selected as potential virus inactivation candidates.[165,166] CD44 antibody targeting high expression CD44 receptor on MDA-MB-231 cells was used as the antibody model in preliminary studies. CD44 monoclonal antibody was diluted in phosphate buffer solution (PBS), cell culture medium, or human plasma (10 times diluted in PBS) at different concentrations. The antibodies were incubated with different concentrations of beta-propiolactone (BPL) (0 to 0.1% final concentration) for16 h at 4°C, followed by 2h incubation at 37°C. Similarly, antibodies were incubated with different concentrations of formaldehyde (FA) (0 to 4% final concentration) for 1 h at RT. The activities of the CD44 antibodies with and without BPL treatments, and with and without FA treatments, were evaluated by characterizing their bindings to CD44 receptors on MDA-MB-231 breast cancer cells (MDA-MB-231 has high expression of CD44) using an indirect cellular ELISA assay.[167] In this assay, horseradish peroxidase (HRP)-conjugated anti-mouse IgG secondary binds to CD44 antibody on MDA-MB-231 cells and be detected by 3,3,5,5-tetramethylbenzidine

solution (TMB) via enzyme-based amplification. Colorimetric signals were recorded at 450 nm. To compare the antibody activities between different groups, we normalized the signals using the untreated groups (0% BPL and 0% FA) as the reference (100% activity). When the optimal reagent was determined for method compatibility, it was tested using our optimized ELISA method for detection of SARS-CoV-2 anti-S1.

2.4 Optimization of Standard ELISA for SARS-CoV-2 Spike Protein Antibodies

Each parameter of a capture-based sandwich ELISA method was tested for optimal detection of SARS-CoV-2 anti-S1 IgG. In our optimized procedure, 50 µL of 5 µg/mL SARS-CoV-2 spike protein S1 subunit in PBS is used to coat wells of a 96-well plate for 16 h at 4°C. The S1 subunit solution is removed and followed by gentle washing by PBS three times. Non-specific binding is then blocked by 100 µL of 1% BSA solution in PBS for 30 minutes at 37°C. The blocking buffer is removed and followed by three gentle washings with PBS. Next, 50 µL of various concentrations of anti-S1 IgG in various matrices are incubated in the well for 1 h at 37°C. Anti-S1 IgG is removed followed by 2 washings by PBST (0.05%) and 3 washings by PBS. Wells are then incubated with 50 µL of 120 ng/mL goat anti-mouse IgG/HRP in 1% BSA for 1 h at 37°C. Secondary antibody is then removed followed by 2 washings by PBST (0.05%) and 3 washings by PBS. Next, wells are incubated 100 µL of TMB substrate solution for 30 min at 37°C. Finally, 100 µL of 0.2 M sulfuric acid are added to each well and the absorbance of each well was measured at 450 nm using a BioTek ELx800 microplate reader.

2.5 Identification of a Method for AuNP-Enhanced ELISA

Based on the unique surface properties of AuNPs, the possibility of packing significant amounts of targeting ligand or targeting antibody along with HRP for signal generation onto

AuNP surface became realized. In effect, this would not change the scheme or technical difficulty of ELISA as traditional secondary antibody would simply be replaced by AuNP-enhanced secondary antibody. Several methods were analyzed to determine which modified AuNP was capable of delivering the greatest target affinity and specificity along with the highest signal generation. Some of the methods explored include (1) simultaneous and sequential addition of thiolated streptavidin (SA-SH) and thiolated horseradish peroxidase (HRP-SH) to AuNPs, (2) attachment of dibenzocyclooctyne (DBCO)-HRP-SH to AuNP surface, followed by conjugation of azide-streptavidin to HRP via bioorthogonal click chemistry, and (3) direct attachment of HRP-conjugated anti-IgG to AuNP surface by thiolation of anti-IgG/HRP and subsequently reacting with AuNP. Studies showed direct attachment of anti-IgG/HRP to AuNP surface were the optimal choice for AuNPs with the highest target affinity as well as enzyme activity. In addition to conjugation method, AuNP size was also evaluated for optimization. To this end, 40-, 50-, 60-, and 80-nm AuNPs were tested and it was determined anti-IgG/HRP-conjugated 80-nm AuNPs provided that greatest HRP activity without sacrificing target affinity.

2.6 Synthesis of anti-IgG/HRP-AuNPs

First, 20 µg anti-IgG/HRP were purified using 10 kDa MWCO centrifugal filter at 13000 RPM for 4 minutes. Anti-IgG/HRP was re-dispersed to 0.4 mg/mL in carbonate/bicarbonate (pH 9) buffer. Next, anti-IgG/HRP solution was gently mixed with HS-PEG-NHS with a molar ratio of 250 HS-PEG-NHS: anti-IgG/HRP and the mixture was incubated for 2 h at 37°C. After incubation, 100 µL of 50 mM Tris (pH 8) buffer was added to mixture to quench the reaction. Next, anti-IgG/HRP-PEG-SH was purified from unbound linker three times using 10 kDa MWCO centrifugal filter at 13000 RPM for 4 minutes. After each purification, antibody solution was washed with 200 µL 20 mM HEPES (pH 7). After final purification, anti-IgG/HRP-PEG-SH

was re-dispersed in HEPES buffer with a concentration of 0.4 mg/mL and mixed with 80 pM colloidal AuNPs (containing 0.05% Tween-20) using a molar ratio of 2000 anti-IgG/HRP-PEG-SH:AuNP. The mixture was vortexed gently for 30 s and incubated for 16 h at 4°C in the dark. Next, mPEG-SH was added to the mixture with a molar ratio of 30,000 mPEG-SH:AuNP and gently shaken for 1.5 h at 25°C in the dark. Finally, modified AuNPs were purified three times by centrifuging at 10,000 RPM for 5 min. Anti-IgG/HRP-PEG-AuNP solution was washed with PBST between purifications and re-dispersed in PBST after final purification.

2.7 Characterization of IgG-HRP-AuNPs

The optical extinction of AuNPs was characterized by Thermo Scientific SPECTRONIC™ 200 spectrophotometer. The size of anti-IgG/HRP-conjugated AuNPs and unconjugated AuNPs were characterized by DLS. A TMB assay was performed to confirm the successful conjugation of anti-IgG/HRP to AuNPs by our conjugation method. Briefly, 100 μL of anti-IgG/HRP-conjugated AuNPs were mixed with 25 μL of TMB Plus Liquid 1-Component substrate solution for 25 min and the color change of the solution was recorded. AuNPs without anti-IgG/HRP were used as a negative control.

2.8 AuNP-Enhanced ELISA for SARS-CoV-2 Spike Protein Antibodies in PBS and Healthy Human Blood Plasma

The optimized anti-IgG/HRP-conjugated AuNPs were tested for satisfactory replacement of standard anti-IgG/HRP secondary antibody using our capture-based sandwich ELISA for detection of SARS-CoV-2 anti-S1 IgG. Anti-S1 was spiked into a variety of matrices including PBS, diluted human healthy blood plasma, as well as pure human healthy blood plasma. Negative controls included the respective sample matrix with no anti-S1 added, while still

receiving anti-IgG/HRP-conjugated AuNPs. In this manner, a range of anti-S1 concentrations were tested to determine the linear range and sensitivity of enhanced ELISA method. The plot of optical density (O.D.) at 450 nm versus the concentration of anti-S1 was fitted linearly using Microsoft Excel to get the calibration curve. The limit of detection (LOD) for conventional and enhanced ELISA were evaluated in PBS and human blood plasma. The LOD was calculated using the formula in eq. 4.1,

$$LOD = \frac{3.3 \times S_{yx}}{s} \qquad (4.1)$$

where S_{yx} is the standard error of the predicted y-value for each x-value in the regression, and s is the slope of the calibration curve. Parameters remained constant between standard and enhanced ELISA methods for adequate comparison.

3. Results and Discussion

3.1 Effect of Formaldehyde on CD44 Antibody Activity by Determining Their Binding to CD44 Receptor on MDA-MB-231 Breast Cancer Cells

Figure 4.1 and Table 4.1 show a comparison of the CD44 antibody activity after incubation with FA of different concentrations. The results show that the activity significantly decreased after FA treatments for all tested FA concentrations. When the antibody was treated with 0.5% FA (the concentration that has shown to cause complete virus inactivation), the antibody activity decreased by 14%, 27%, 35% for 2 µg/mL, 1 µg/mL, and 0.5 µg/mL CD44 antibody, respectively. Increasing FA concentrations further reduced antibody activity.

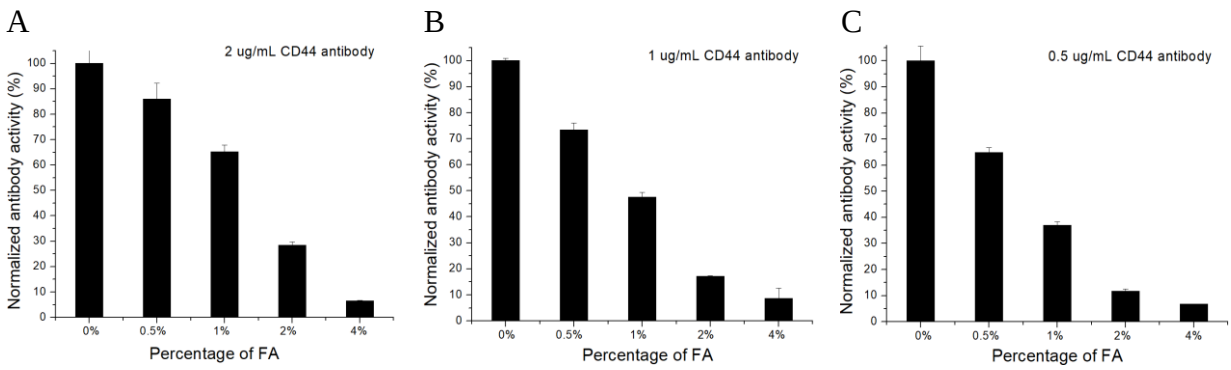

Figure 4.1 Normalized antibody activity after FA treatment with different concentrations. (A) 2 µg/mL CD44 antibody. (B) 1 µg/mL CD44 antibody. (C) 0.5 µg/mL CD44 antibody. All treatments were performed in PBS.

Table 4.1: Effect of formaldehyde on CD44 antibody activity to their binding to CD44 receptor on MDA-MB-231 breast cancer cells.

	Concentration of formaldehyde				
Concentration of CD44 antibody	**0%**	**0.5%**	**1%**	**2%**	**4%**
2 µg/mL	100±6.1%	**86.0±6.3%**	65.2±2.6%	28.4±1.3%	6.5±0.2%
1 µg/mL	100±0.9%	**73.4±2.6%**	47.5±1.8%	17.1±0.2%	8.6±4.0%
0.5 µg/mL	100±5.7%	**64.8±1.8%**	36.8±1.4%	11.7±0.8%	6.6±0.2%

3.2 Effect of beta-Propiolactone on CD44 Antibody Activity by Determining Their Binding to CD44 Receptor on MDA-MB-231 Breast Cancer Cells

Figure 4.2 A shows a comparison of the CD44 antibody activity after incubation with BPL of different concentrations in PBS at a concentration of 2 µg/mL. As listed in Table 4.2, the activity slightly decreased to 96% after treatment with 0.0125% BPL, the concentration that caused complete virus inactivation. Further increase of the BPL concentration led to more activity reduction, with 0.025% BPL to 91%, 0.05% BPL to 88.7% and 0.1% BPL to 72.6%.

Since antibody concentration varies as the infection goes on, we need to examine whether the effect of BPL treatment depends on the antibody concentration. Figure 4.2 B shows the BPL effect of CD44 antibody at 1 µg/mL and Figure 4.2 C shows the effect of CD44 antibody at 0.5 µg/mL. The results show that the adverse effect of BPL increased when the concentration of antibody decreased. For example, the treatment of 1 µg/mL CD44 antibody with 0.0125% BPL reduced the antibody activity by 12% while treatment of 0.5 µg/mL CD44 antibody with 0.0125% BPL reduced the antibody activity by 18%.

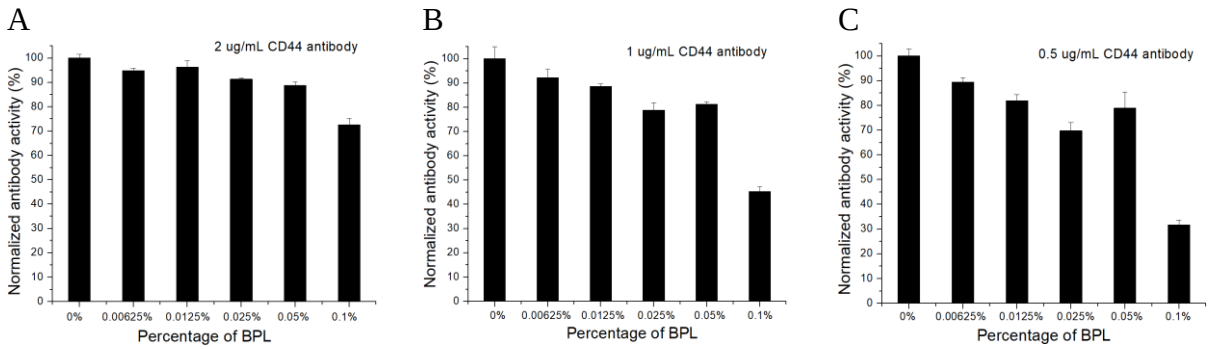

Figure 4.2. Normalized antibody activity after BPL treatment with different concentrations of BPL for different concentrations of antibodies. (A) 2 µg/mL CD44 antibody. (B) 1 µg/mL CD44 antibody. (C) 0.5 µg/mL CD44 antibody. All treatments were performed in PBS.

To further examine the matrix effect, we diluted CD44 antibody in cell culture medium and 10x diluted (with PBS) human plasma using 0.5 µg/mL CD44 antibody as the model. The results show that the adverse effect of BPL to antibody activity is significantly lower when the treatment was performed in 10x diluted plasma than the treatments in PBS and cell culture medium (Figure 4.3)**.** For the treatment with 0.0125% BPL in the 10x diluted plasma, the antibody activity decreased by 8%, in contrast to 18% in PBS and 16% in medium.

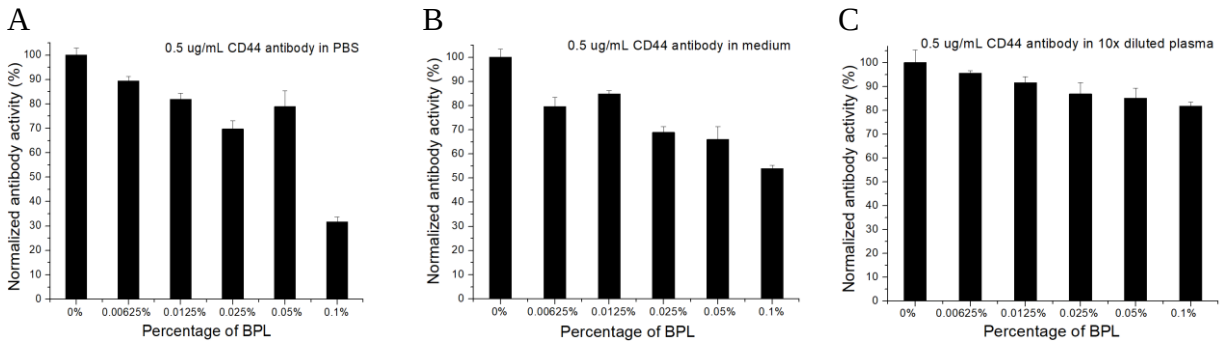

Figure 4.3 Normalized antibody activity after BPL treatment with different concentrations of BPL for antibodies diluted in different matrix. (A) PBS. (B) cell culture medium. (C) 10 times PBS-diluted human plasma.

To measure the effect of BPL on antibody activity in plasma directly, we diluted CD44 antibody in human plasma (without dilution) in the presence of 0.0125% BPL. Three antibody concentrations were examined: 0.5 µg/mL, 0.1 µg/mL, and 0.05 µg/mL. The results (Figure 4.4 and Table 4.2) show that the antibody activity reduced by 7%, 16%, and 19% for 0.5 ug/mL, 0.1 ug/mL, and 0.05 ug/mL, respectively. BPL reduced the antibody activities for all tested concentrations of BPL and antibodies. The adverse effect increased when the concentration of antibodies decreases. At the lowest concentration of BPL (0.0125%) for virus complete inactivation, the mildest effect was the treatment of antibody in 10x diluted plasma.

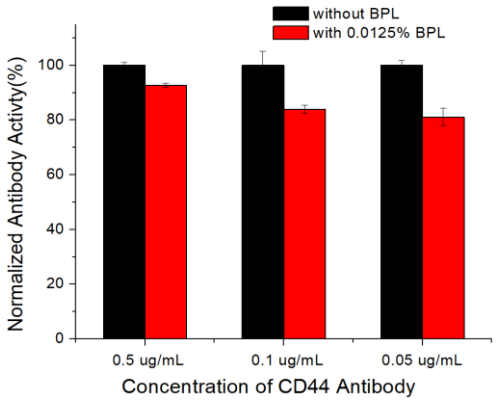

Figure 4.4 Normalized antibody activity of different concentrations anti-CD44 after treatment with 0.0125% BPL in plasma.

The antibody activity decreased by 8% when 0.5 µg/mL CD44 antibody was treated with 0.0125% BPL in 10x diluted plasma. When BPL treatment was performed in plasma directly, the antibody activity decreased by 7% for 0.5 µg/mL CD44 antibody, 16% for 0.1 µg/mL CD44 antibody, and 19% for 0.05 µg/mL CD44 antibody. This indicates that at low antibody concentrations (≤0.1 ug/mL), the BPL effect is significant and may not be ignored.

Table 4.2: Effect of BPL on CD44 antibody activity to their binding to high expression CD44 receptor on MDA-MB-231 breast cancer cells.

	Concentration of BPL					
Concentration of CD44 antibody	0%	0.00625%	**0.0125%**	0.025%	0.05%	0.1%
2 µg/mL in PBS	100±1.6%	94.8±1.1%	**96.2±2.6%**	91.3±0.6%	88.7±1.6%	72.6±2.7%
1 µg/mL in PBS	100±5.1%	92.2±3.6%	**88.6±1.0%**	78.8±3.2%	81.2±1.0%	45.2±2.0%
0.5 µg/mL in PBS	100±2.9%	89.4±1.9%	**81.9±2.5%**	69.8±3.4%	78.9±6.5%	31.7±2.0%
0.5 µg/mL in cell culture medium	100±3.4%	79.6±3.7%	**84.8±1.4%**	68.8±2.5%	65.9±5.3%	53.8±1.53%
0.5 µg/mL in 10x diluted human plasma	100±5.3%	95.5±1.18%	**91.6±2.5%**	86.9±4.72%	85.1±4.3%	81.7±1.9%
0.5 µg/mL in plasma	100±1.0%	-	**92.7±0.8%**	-	-	-
0.1 µg/mL in plasma	100±5.1%	-	**83.9±1.5%**	-	-	-
0.05 µg/mL in plasma	100±1.7%	-	**81.1±3.2%**	-	-	-

3.3 Effect of beta-Propiolactone on anti-S1 Activity by Determining Their Binding to S1 Subunit in Sandwich ELISA

When the deteriorating effect of BPL on antibodies was thoroughly modeled using anti-CD44, it became necessary to treat SARS-CoV-2 anti-S1 IgG with BPL as a complete simulation of the effect our targeted analyte will undergo during virus inactivation. Anti-S1 was incubated with 0.0125% BPL in pure human blood plasma using low concentrations of antibody. It was

determined that 0.01 µg/mL anti-S1 experienced a 10% decrease in activity, and 0.02 µg/mL anti-S1 experienced a 3% decrease in activity upon treatment with BPL (Figure 4.5). The decrease in antibody activity is expected following our studies with anti-CD44, but the effect is less pronounced when treating anti-S1. This may be due to differences between our cellular ELISA for detecting anti-CD44 compared to our sandwich ELISA for detecting anti-S1, or maybe due to differences in the two antibodies. However, this study confirms that 0.0125% BPL, while mildly affecting antibody activity, is a virus inactivation agent that is compatible with our detection assay.

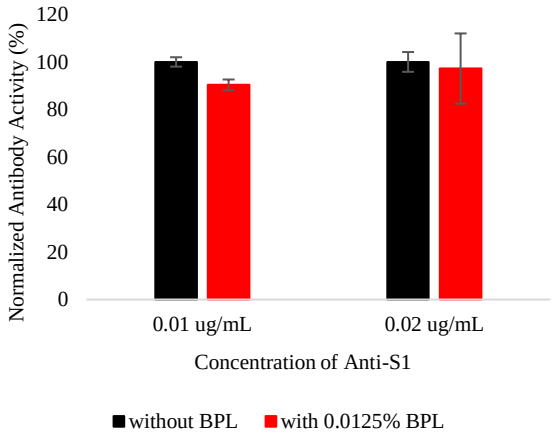

Figure 4.5 Normalized antibody activity of different concentrations of anti-S1 after treatment with 0.0125% BPL in plasma.

3.4 Optimization of Sandwich ELISA for Detection of Anti-S1

To qualify the improvement of our enhanced ELISA method over the standard ELISA technique, each parameter of the standard sandwich ELISA was calibrated for optimal detection of anti-S1. First, the coating concentration of capture protein, SARS-CoV-2 spike protein S1 subunit, was varied from 1 to 10 µg/mL. As seen in Figure 4.6 A, there is a rapid incline in the detection sensitivity of this assay from 1 to 5 µg/mL S1 coating concentration. 5 µg/mL S1 was

selected as the optimal coating concentration for maximizing detection sensitivity as well as reagent life, as there is only a 7% increase in detection sensitivity from 5 to 10 µg/mL. Anti-IgG/HRP was titrated between 1:2000 and 1:5000 upon manufacturer's recommendation to determine optimal conditions and 1:3400 dilution, or 120 ng/mL, of anti-IgG/HRP was selected for generating the highest signal-to-noise ratio. TMB substrate was incubated with 1 and 2 ng/mL anti-IgG/HRP and the reaction was stopped at time points from 1 to 120 min. From Figure 4.6 B, it is apparent most of the signal is generated in the first 30 minutes of the reaction. The optimal incubation time for HRP/TMB reaction was selected to be 30 min for obtaining maximum detection sensitivity without drastically lengthening the assay time.

The detection capability of the optimized sandwich ELISA was tested for sensitivity to SARS-CoV-2 anti-S1 IgG. To determine the limit of detection (LOD) for this assay, anti-S1 was spiked into PBS as well as pure human healthy blood plasma at concentrations from 0.5 to 20 ng/mL, as seen in Figure 4.6 C-D. The LOD of our optimized standard ELISA for anti-S1 in PBS was determined to be 3.7 ng/mL. In plasma samples, the LOD was determined to be 1.1 ng/mL. Although detecting anti-S1 in plasma generates substantially higher signals than for PBS, the negative controls gave comparable signals for the two different matrices. The background signal for anti-S1-containing plasma was 26% higher compared to PBS samples, likely due to cross-reactivity between the secondary antibody and components in the plasma. The calibration curves in these assays show a good fit to the data with coefficients of determination of 0.983 and 0.995 in PBS and plasma, respectively.

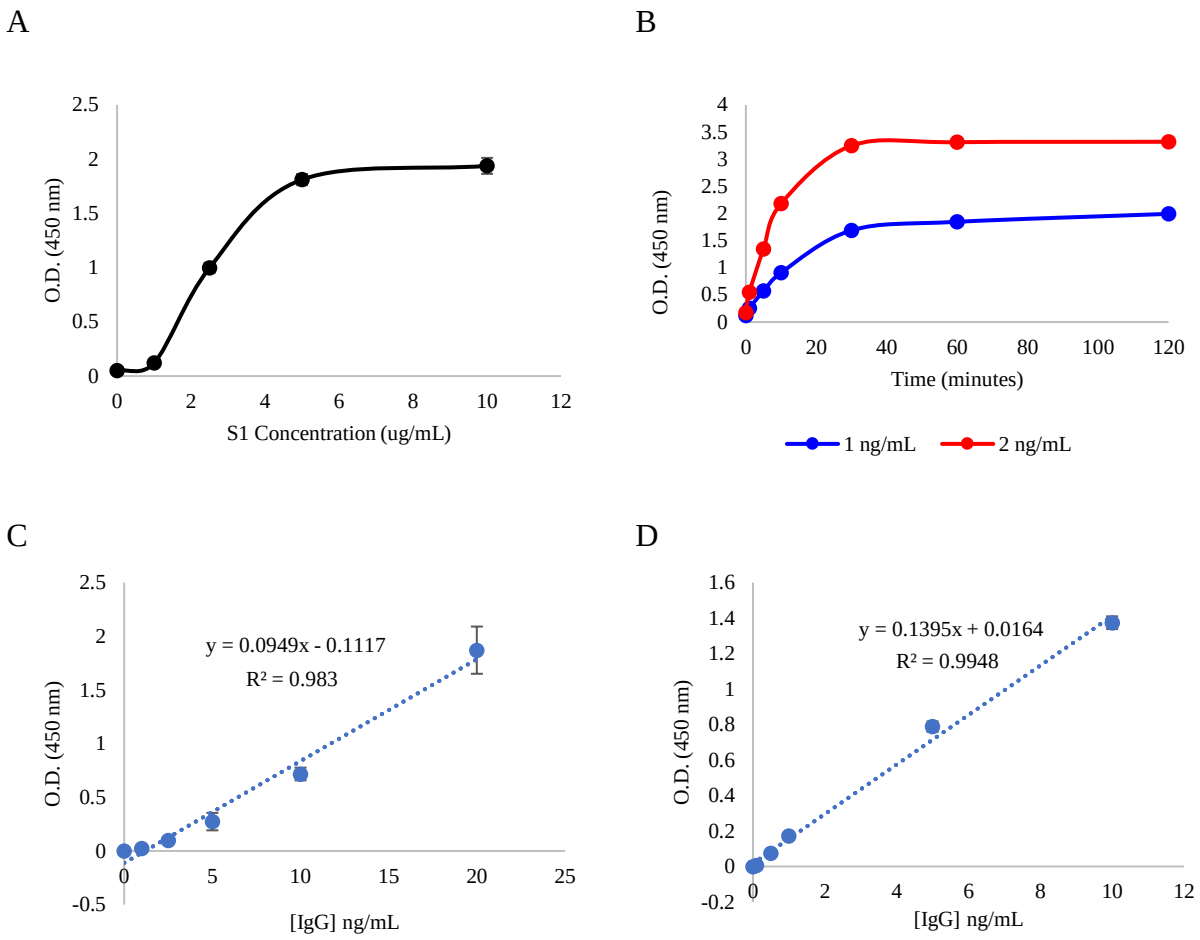

Figure 4.6 Optimization of standard ELISA method for detection of SARS-CoV-2 spike protein IgG. (A) Determination of optimum spike protein S1 subunit coating concentration for capture of spike protein antibody. (B) Optimizing the TMB reaction by incubating with 1 ng/mL and 2 ng/mL IgG-HRP solution. Determining the sensitivity of standard ELISA for detecting SARS-CoV-2 spike protein antibody in PBS (C) and healthy human blood plasma (D).

3.5 Design of the AuNP-Enhanced ELISA

Sandwich ELISA is an established method for selective capture and sensitive detection of biological analytes through serology testing. Since the method is widely employed, it is conceivable to build on our understanding and infrastructure and design novel methods for sensitive detection using ELISA as a template. We selected AuNPs as a mode by which we can amplify standard ELISA detection based on the unique surface properties of AuNPs.[168] For one, their nm-range size imparts compatibility for interacting with like-sized bio-analytes.

Additionally, they exhibit high surface-to-volume ratios critical for delivering maximum amounts of probing molecules. Furthermore, they display a chemically reactive surface that may be readily functionalized with targeting biomolecules. For these reasons, we elected to use IgG-targeted AuNPs to deliver large amounts of HRP near analyte for the sensitive detection of SARS-CoV-2 anti-S1 IgG. Figure 4.7 shows a comparison between the two detection schemes of standard ELISA and AuNP-enhanced ELISA.

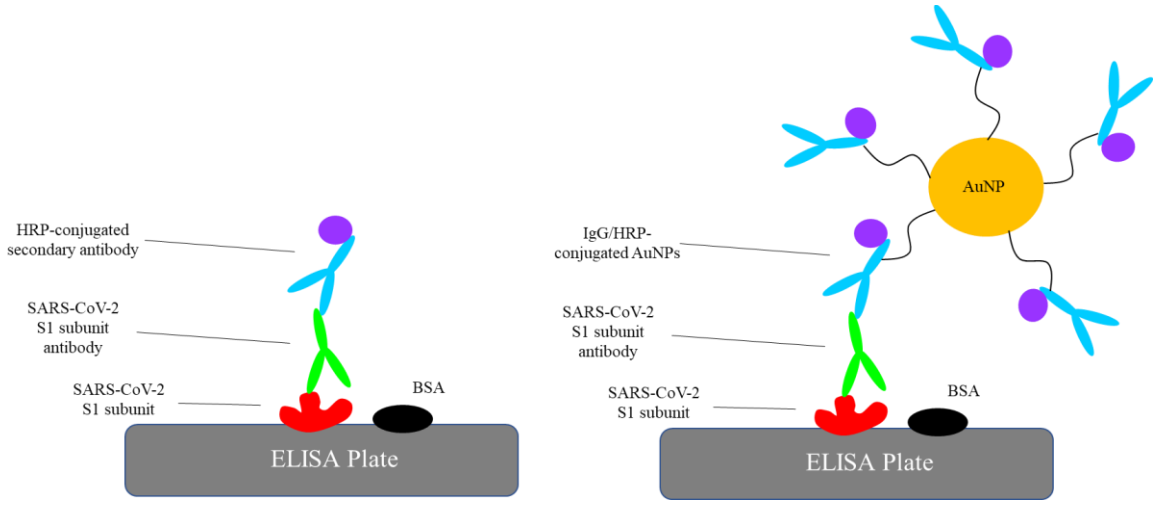

Figure 4.7 A schematic representation of standard ELISA (left) method compared to AuNP-enhanced ELISA (right) method for detection SARS-CoV-2 spike protein antibodies.

3.6 Application of AuNP-Enhanced ELISA for Detecting SARS-CoV-2 anti-S1

We applied our enhanced ELISA technique to PBS and human blood plasma samples with anti-S1 spiked in as seen in Figure 4.8. The technique remained identical to standard ELISA technique except for the replacement of standard secondary antibody, anti-IgG/HRP, by our anti-IgG/HRP-conjugated AuNP. In PBS, we see a significant improvement in sensitivity over standard ELISA with an LOD of 18.0 pg/mL and a similar coefficient of determination, 0.986. In pure human blood plasma, we observe a marked improvement over standard ELISA, but with a

higher LOD, 370.5 pg/mL, than we experience for enhanced ELISA in PBS. It is also observed that AuNP-enhanced ELISA generates a higher background signal than standard ELISA. The effect is especially exaggerated in pure plasma. However, we determined that the exaggerated background subsides as plasma is further diluted, indicating the utility of this method for determining the antibody titer in serology testing.

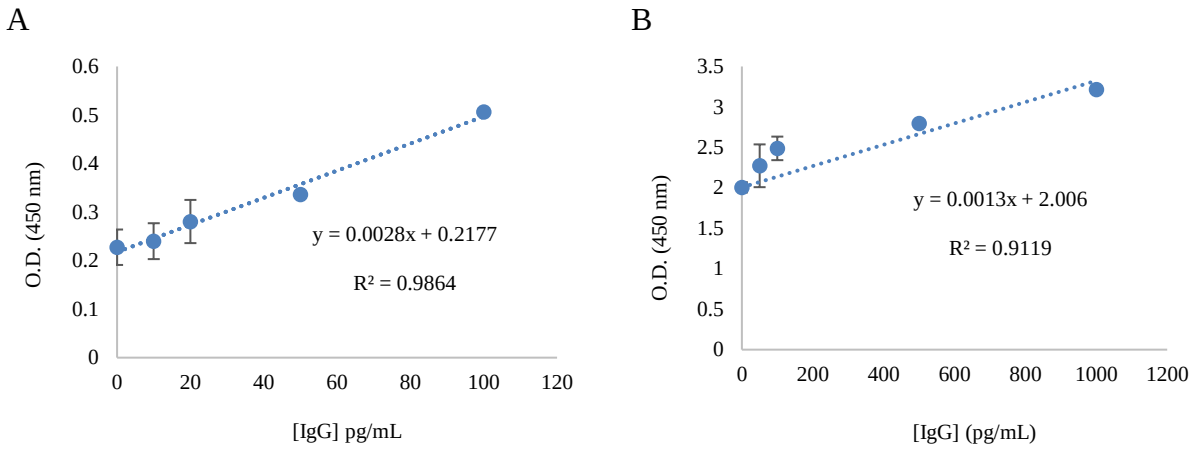

Figure 4.8 Determining the sensitivity of AuNP-enhanced ELISA for detecting SARS-CoV-2 spike protein IgG in (A) PBS and (B) healthy human blood plasma through a series of spike-in experiment. Although AuNP-enhanced method does generate significantly more background than standard ELISA, the limit of detection is significantly lower for enhanced method.

4. Conclusion and Future Outlook

In this study, we demonstrated the ability to use AuNPs in an effort to enhance ELISA for the detection of SARS-CoV-2 anti-S1 IgG. We used AuNPs' high surface-to-volume ratio and surface reactivity to efficiently load their surface with HRP and targeting antibody. This method significantly improves the sensitivity of standard ELISA by as much as 200-fold in PBS without increasing the difficulty and time of the assay. We intend to continue the development of this method by applying it to SARS-CoV-2-infected mouse sera in a collaboration with Dr. Kui

Li of University of Tennessee Health Science Center in Memphis, TN. In this collaboration we seek not only to prove the sensitivity of this enhanced assay, but to gain an understanding of virus-host interactions through real-time monitoring of serum in mouse models.

Chapter 5. CONCLUSION AND FURTHER PERSPECTIVES

In this dissertation, we have provided an overview of the history of AuNPs. Furthermore, we have discussed some of the important qualities of AuNPs that make them so useful in the biomedical field. For one, they are extremely biocompatible, especially when coated with a protective layer such as PEG. Next, they possess excellent loading capacity due to their high surface-to-volume ratio, as well as an easily modified surface allowing functionalization by any number of thiolated molecules. Finally, AuNPs provide superior optical enhancement through the nanoscale phenomenon of localized surface plasmon enhancement. This phenomenon is especially applicable in surface-enhanced Raman scattering spectroscopy enabling single molecule and single particle detection. These properties have allowed researchers to develop some very creative methods for detecting analytes. From metal ions to cancer cells, AuNPs have shown to be a great asset in the field of circulating biomarker detection.

In Chapter 2, we have shown that IO-Au core-shell SERS nanotags can serve a dual function of selectively isolating and detecting CTCs from human whole blood in a microfluidic device. Multicolor SERS nanotags were first realized by the addition of select Raman reporters and targeting ligands to IO-Au core-shell nanoparticles. The multicolor SERS nanotags were then capable of targeting four distinct cancer markers. Furthermore, we showed that distinct Raman signals corresponding to expression of EpCAM, HER2, CD44, and IGF1R could be obtained from a signal mixture by using CLS deconvolution. The cancer marker expression profiles obtained using our method were compared to ELISA profiles as a reference. This comparison suggests that our method has the potential to simultaneously detect CTCs of multiple subpopulations in clinical samples. In our method, all cell isolation/enrichment, negative staining, optical imaging, SERS detection, and molecular profiling were performed on a

microfluidic device. This device increases the degree of operational automation, enables single-cell analysis, and reduces false negative signals by concentrating low-frequency tumor cells. We connect isolation and detection methods with multiplex IO−Au SERS nanotags, making the sample preparation simple and easy to operate. CTC identification is based on a combination of several characteristics at the single-cell level. First, we confirm the morphological standards of suspected cancer cells through bright-field imaging. We then determine if any blood cell impurities are present through fluorescence staining and imaging. Finally, molecular cancer cell detection is ascertained through SERS. The combination of these criteria reduces false positives and ensures detection accuracy. In this manner, a simple, sensitive, and selective method for capture and multicolor detection of CTCs from whole blood is provided.

In Chapter 3, we used ligand-conjugated AuNPs to show that cellular labeling largely depends on the surface chemistry of the particles and the matrix conditions during binding. Thiolated SA was used as a ligand model to show that loading ratio of 5000 or higher is needed to make stable conjugates with uniform size distribution for efficient labeling. We also determined that SA-AuNPs stabilized with a PEG layer were better for cellular labeling than SA-AuNPs without PEG. Interestingly, the molecular weight of PEG did not play an important role in stabilizing the conjugates. When comparing mPEG-SH 2000 and 5000, both PEG-stabilized conjugates showed similar cellular binding. In addition to particle formulation, the matrix conditions for cellular labeling were analyzed for optimal binding potential. We determined that Tween (in PBS) or BSA (in PBS) was necessary for primary and secondary antibody dilution, with antibodies in PBST showing better binding potential than in BSA. We also determined the optimal storage and binding conditions for SA-conjugated AuNPs. We observed that SA-AuNPs stored with BSA experienced particle aggregation, likely due to biotin impurity in BSA. Similar

to primary and secondary antibody conditions, it was shown that PBST provided the best storage and labeling conditions for SA-AuNPs. In this chapter, we have surveyed ligand-conjugated AuNP formulation and cellular labeling matrix conditions with the aim of providing robust techniques to achieve optimal cellular binding results.

In Chapter 4, we sought to use the unique surface properties of AuNPs in order to enhance the sensitivity of conventional ELISA for detecting SARS-CoV-2 spike protein antibody. We utilized the facile surface modification and high surface area-to-volume ratio characteristic of AuNPs to load HRP-conjugated anti-IgG onto particle for colorimetric detection of primary antibody. We optimized the formulation of these IgG/HRP-conjugated AuNPs for selectively recognizing anti-S1 IgG in PBS or human blood plasma. This method for enhancing conventional ELISA was determined to be over 200 times more sensitive than conventional ELISA when analyte is contained in PBS. Substantial background signal was detected when analyte was contained in pure plasma, however, this background is readily overcome by diluting plasma samples with PBS. We intend to continue the development of this method by testing SARS-CoV-2-infected mouse blood serum in collaboration with Dr. Kui Li of University of Tennessee Health Science Center in Memphis, TN. We aim to demonstrate the capability of this method for detecting rare IgG in infected mouse serum as well as to better understand virus-host interactions through real-time monitoring of serum in mouse models.

REFERENCES

1. “PubMed.” National Center for Biotechnology Information. U.S. National Library of Medicine. Accessed October 7, 2021. https://pubmed.ncbi.nlm.nih.gov/.
2. Dreaden, Erik C., Alaaldin M. Alkilany, Xiaohua Huang, Catherine J. Murphy, and Mostafa A. El-Sayed. "The golden age: gold nanoparticles for biomedicine." *Chemical Society Reviews* 41, no. 7 (2012): 2740-2779.
3. Wilson, Robert. "The use of gold nanoparticles in diagnostics and detection." *Chemical Society Reviews* 37, no. 9 (2008): 2028-2045.
4. Freestone, Ian, Nigel Meeks, Margaret Sax, and Catherine Higgitt. "The Lycurgus cup—a roman nanotechnology." *Gold bulletin* 40, no. 4 (2007): 270-277.
5. Faraday, Michael. "X. The Bakerian Lecture.—Experimental relations of gold (and other metals) to light." *Philosophical Transactions of the Royal Society of London* 147 (1857): 145-181.
6. Mie, Gustav. "Contributions to the optics of diffuse media, especially colloid metal solutions." *Ann. Phys* 25 (1908): 377-445.
7. Kerker, Milton. *The scattering of light and other electromagnetic radiation: physical chemistry: a series of monographs*. Vol. 16. Academic press, 2013.
8. Bohren, Craig F., and Donald R. Huffman. *Absorption and scattering of light by small particles*. John Wiley & Sons, 2008.
9. Kelly, K. Lance, Eduardo Coronado, Lin Lin Zhao, and George C. Schatz. "The optical properties of metal nanoparticles: the influence of size, shape, and dielectric environment." (2003): 668-677.

10. Turkevich, John, Peter Cooper Stevenson, and James Hillier. "A study of the nucleation and growth processes in the synthesis of colloidal gold." *Discussions of the Faraday Society* 11 (1951): 55-75.
11. Frens, Gerrit. "Controlled nucleation for the regulation of the particle size in monodisperse gold suspensions." Nature physical science 241, no. 105 (1973): 20-22.
12. Fleischmann, Martin, Patrick J. Hendra, and A. James McQuillan. "Raman spectra of pyridine adsorbed at a silver electrode." *Chemical physics letters* 26, no. 2 (1974): 163-166.
13. Jeanmaire, David L., and Richard P. Van Duyne. "Surface Raman spectroelectrochemistry: Part I. Heterocyclic, aromatic, and aliphatic amines adsorbed on the anodized silver electrode." *Journal of electroanalytical chemistry and interfacial electrochemistry* 84, no. 1 (1977): 1-20.
14. Albrecht, M. Grant, and J. Alan Creighton. "Anomalously intense Raman spectra of pyridine at a silver electrode." *Journal of the american chemical society* 99, no. 15 (1977): 5215-5217.
15. Nie, Shuming, and Steven R. Emory. "Probing single molecules and single nanoparticles by surface-enhanced Raman scattering." *science* 275, no. 5303 (1997): 1102-1106.
16. Mirkin, Chad A., Robert L. Letsinger, Robert C. Mucic, and James J. Storhoff. "A DNA-based method for rationally assembling nanoparticles into macroscopic materials." *Nature* 382, no. 6592 (1996): 607-609.
17. Rosi, Nathaniel L., and Chad A. Mirkin. "Nanostructures in biodiagnostics." *Chemical reviews* 105, no. 4 (2005): 1547-1562.

18. Hirsch, L. R., J. B. Jackson, A. Lee, N. J. Halas, and J. L. West. "A whole blood immunoassay using gold nanoshells." *Analytical Chemistry* 75, no. 10 (2003): 2377-2381.

19. Huang, Xiaohua, Ivan H. El-Sayed, Wei Qian, and Mostafa A. El-Sayed. "Cancer cell imaging and photothermal therapy in the near-infrared region by using gold nanorods." *Journal of the American Chemical Society* 128, no. 6 (2006): 2115-2120.

20. Link, Stephan, and Mostafa A. El-Sayed. "Spectral properties and relaxation dynamics of surface plasmon electronic oscillations in gold and silver nanodots and nanorods." *The Journal of Physical Chemistry B* 103, no. 40 (1999): 8410-8426.

21. Pong, Boon-Kin, Hendry I. Elim, Jian-Xiong Chong, Wei Ji, Bernhardt L. Trout, and Jim-Yang Lee. "New insights on the nanoparticle growth mechanism in the citrate reduction of gold (III) salt: formation of the Au nanowire intermediate and its nonlinear optical properties." *The Journal of Physical Chemistry C* 111, no. 17 (2007): 6281-6287.

22. Ji, Xiaohui, Xiangning Song, Jun Li, Yubai Bai, Wensheng Yang, and Xiaogang Peng. "Size control of gold nanocrystals in citrate reduction: the third role of citrate." *Journal of the American Chemical Society* 129, no. 45 (2007): 13939-13948.

23. Ojea-Jiménez, Isaac, Francisco M. Romero, Neus G. Bastús, and Victor Puntes. "Small gold nanoparticles synthesized with sodium citrate and heavy water: insights into the reaction mechanism." *The Journal of Physical Chemistry C* 114, no. 4 (2010): 1800-1804.

24. Masuda, Hideki, Hideki Tanaka, and Nobuyoshi Baba. "Preparation of porous material by replacing microstructure of anodic alumina film with metal." *Chemistry letters* 19, no. 4 (1990): 621-622.

25. Brumlik, Charles J., and Charles R. Martin. "Template synthesis of metal microtubules." *Journal of the American Chemical Society* 113, no. 8 (1991): 3174-3175.
26. Payne, Emma Kathryn, Kevin L. Shuford, Sungho Park, George C. Schatz, and Chad A. Mirkin. "Multipole plasmon resonances in gold nanorods." *The Journal of Physical Chemistry B* 110, no. 5 (2006): 2150-2154.
27. Yu, Yu-Ying, Ser-Sing Chang, Chien-Liang Lee, and CR Chris Wang. "Gold nanorods: electrochemical synthesis and optical properties." *The Journal of Physical Chemistry B* 101, no. 34 (1997): 6661-6664.
28. Jana, Nikhil R., Latha Gearheart, and Catherine J. Murphy. "Seed-mediated growth approach for shape-controlled synthesis of spheroidal and rod-like gold nanoparticles using a surfactant template." *Advanced Materials* 13, no. 18 (2001): 1389-1393.
29. Nikoobakht, Babak, and Mostafa A. El-Sayed. "Preparation and growth mechanism of gold nanorods (NRs) using seed-mediated growth method." *Chemistry of Materials* 15, no. 10 (2003): 1957-1962.
30. Huang, Xiaohua, Svetlana Neretina, and Mostafa A. El-Sayed. "Gold nanorods: from synthesis and properties to biological and biomedical applications." *Advanced materials* 21, no. 48 (2009): 4880-4910.
31. Chen, Jingyi, Joseph M. McLellan, Andrew Siekkinen, Yujie Xiong, Zhi-Yuan Li, and Younan Xia. "Facile synthesis of gold− silver nanocages with controllable pores on the surface." *Journal of the American Chemical Society* 128, no. 46 (2006): 14776-14777.
32. Liang, Zhijian, Andrei Susha, and Frank Caruso. "Gold nanoparticle-based core− shell and hollow spheres and ordered assemblies thereof." *Chemistry of Materials* 15, no. 16 (2003): 3176-3183.

33. Zhang, Jian, Mark R. Langille, Michelle L. Personick, Ke Zhang, Shuyou Li, and Chad A. Mirkin. "Concave cubic gold nanocrystals with high-index facets." *Journal of the American Chemical Society* 132, no. 40 (2010): 14012-14014.

34. Shankar, S. Shiv, Akhilesh Rai, Balaprasad Ankamwar, Amit Singh, Absar Ahmad, and Murali Sastry. "Biological synthesis of triangular gold nanoprisms." *Nature materials* 3, no. 7 (2004): 482-488.

35. Kwizera, Elyahb Allie, Elise Chaffin, Yongmei Wang, and Xiaohua Huang. "Synthesis and properties of magnetic-optical core–shell nanoparticles." *RSC advances* 7, no. 28 (2017): 17137-17153.

36. Cho, Sung-Jin, Benjamin R. Jarrett, Angelique Y. Louie, and Susan M. Kauzlarich. "Gold-coated iron nanoparticles: a novel magnetic resonance agent for T1 and T2 weighted imaging." *Nanotechnology* 17, no. 3 (2006): 640.

37. Melancon, Marites P., Andrew Elliott, Xiaojun Ji, Anil Shetty, Zhi Yang, Mei Tian, Brian Taylor, R. Jason Stafford, and Chun Li. "Theranostics with multifunctional magnetic gold nanoshells: photothermal therapy and t2* magnetic resonance imaging." *Investigative radiology* 46, no. 2 (2011): 132.

38. Ji, Xiaojun, Ruping Shao, Andrew M. Elliott, R. Jason Stafford, Emilio Esparza-Coss, James A. Bankson, Gan Liang et al. "Bifunctional gold nanoshells with a superparamagnetic iron oxide− silica core suitable for both MR imaging and photothermal therapy." *The Journal of Physical Chemistry C* 111, no. 17 (2007): 6245-6251.

39. Pham, Thao Thi Hien, Cuong Cao, and Sang Jun Sim. "Application of citrate-stabilized gold-coated ferric oxide composite nanoparticles for biological separations." *Journal of magnetism and magnetic materials* 320, no. 15 (2008): 2049-2055.

40. Lu, Q. H., K. L. Yao, D. Xi, Z. L. Liu, X. P. Luo, and Q. Ning. "Synthesis and characterization of composite nanoparticles comprised of gold shell and magnetic core/cores." *Journal of magnetism and magnetic materials* 301, no. 1 (2006): 44-49.

41. Banerjee, S., S. O. Raja, M. Sardar, N. Gayathri, B. Ghosh, and A. Dasgupta. "Iron oxide nanoparticles coated with gold: Enhanced magnetic moment due to interfacial effects." *Journal of Applied Physics* 109, no. 12 (2011): 123902.

42. Goon, Ian Y., Leo MH Lai, May Lim, Paul Munroe, J. Justin Gooding, and Rose Amal. "Fabrication and dispersion of gold-shell-protected magnetite nanoparticles: systematic control using polyethyleneimine." *Chemistry of Materials* 21, no. 4 (2009): 673-681.

43. Kwizera, Elyahb Allie, Elise Chaffin, Xiao Shen, Jingyi Chen, Qiang Zou, Zhiming Wu, Zheng Gai et al. "Size-and shape-controlled synthesis and properties of magnetic–plasmonic core–shell nanoparticles." *The Journal of Physical Chemistry C* 120, no. 19 (2016): 10530-10546.

44. Hao, Encai, George C. Schatz, and Joseph T. Hupp. "Synthesis and optical properties of anisotropic metal nanoparticles." *Journal of fluorescence* 14, no. 4 (2004): 331-341.

45. Shukla, Ravi, Vipul Bansal, Minakshi Chaudhary, Atanu Basu, Ramesh R. Bhonde, and Murali Sastry. "Biocompatibility of gold nanoparticles and their endocytotic fate inside the cellular compartment: a microscopic overview." *Langmuir* 21, no. 23 (2005): 10644-10654.

46. Mosmann, Tim. "Rapid colorimetric assay for cellular growth and survival: application to proliferation and cytotoxicity assays." *Journal of immunological methods* 65, no. 1-2 (1983): 55-63.

47. Fratoddi, Ilaria, Iole Venditti, Cesare Cametti, and Maria Vittoria Russo. "The puzzle of toxicity of gold nanoparticles. The case-study of HeLa cells." *Toxicology Research* 4, no. 4 (2015): 796-800.

48. Tamarkin, Lawrence, Lonni Myer, Ryan Haynes, and Guilio Paciotti. "CYT-6091 (Aurimune™): A Colloidal Gold-Based Tumor-Targeted Nanomedicine." *MRS Online Proceedings Library Archive* 1019 (2007).

49. AshaRani, P. V., Grace Low Kah Mun, Manoor Prakash Hande, and Suresh Valiyaveettil. "Cytotoxicity and genotoxicity of silver nanoparticles in human cells." *ACS nano* 3, no. 2 (2009): 279-290.

50. Boisselier, Elodie, and Didier Astruc. "Gold nanoparticles in nanomedicine: preparations, imaging, diagnostics, therapies and toxicity." *Chemical society reviews* 38, no. 6 (2009): 1759-1782.

51. Spadavecchia, Jolanda, Dania Movia, Caroline Moore, Ciaran Manus Maguire, Hanane Moustaoui, Sandra Casale, Yuri Volkov, and Adriele Prina-Mello. "Targeted polyethylene glycol gold nanoparticles for the treatment of pancreatic cancer: from synthesis to proof-of-concept in vitro studies." *International journal of nanomedicine* 11 (2016): 791.

52. Farooq, Muhammad U., Valentyn Novosad, Elena A. Rozhkova, Hussain Wali, Asghar Ali, Ahmed A. Fateh, Purnima B. Neogi, Arup Neogi, and Zhiming Wang. "Gold

nanoparticles-enabled efficient dual delivery of anticancer therapeutics to HeLa cells." *Scientific reports* 8, no. 1 (2018): 1-12.

53. Daniel, Marie-Christine, and Didier Astruc. "Gold nanoparticles: assembly, supramolecular chemistry, quantum-size-related properties, and applications toward biology, catalysis, and nanotechnology." *Chemical reviews* 104, no. 1 (2004): 293-346.
54. Giersig, Michael, and Paul Mulvaney. "Preparation of ordered colloid monolayers by electrophoretic deposition." *Langmuir* 9, no. 12 (1993): 3408-3413.
55. Campion, Alan, and Patanjali Kambhampati. "Surface-enhanced Raman scattering." *Chemical society reviews* 27, no. 4 (1998): 241-250.
56. Bain, Colin D., E. Barry Troughton, Yu Tai Tao, Joseph Evall, George M. Whitesides, and Ralph G. Nuzzo. "Formation of monolayer films by the spontaneous assembly of organic thiols from solution onto gold." *Journal of the American Chemical Society* 111, no. 1 (1989): 321-335.
57. Love, J. Christopher, Lara A. Estroff, Jennah K. Kriebel, Ralph G. Nuzzo, and George M. Whitesides. "Self-assembled monolayers of thiolates on metals as a form of nanotechnology." *Chemical reviews* 105, no. 4 (2005): 1103-1170.
58. Walter, Michael, Jaakko Akola, Olga Lopez-Acevedo, Pablo D. Jadzinsky, Guillermo Calero, Christopher J. Ackerson, Robert L. Whetten, Henrik Grönbeck, and Hannu Häkkinen. "A unified view of ligand-protected gold clusters as superatom complexes." *Proceedings of the National Academy of Sciences* 105, no. 27 (2008): 9157-9162.

59. Hou, Wenbo, Mita Dasog, and Robert WJ Scott. "Probing the relative stability of thiolate-and dithiolate-protected Au monolayer-protected clusters." *Langmuir* 25, no. 22 (2009): 12954-12961.

60. Zhao, Yan, Waleska Pérez-Segarra, Qicun Shi, and Alexander Wei. "Dithiocarbamate assembly on gold." *Journal of the American Chemical Society* 127, no. 20 (2005): 7328-7329.

61. Dreaden, Erik C., Sandra C. Mwakwari, Quaovi H. Sodji, Adegboyega K. Oyelere, and Mostafa A. El-Sayed. "Tamoxifen− poly (ethylene glycol)− thiol gold nanoparticle conjugates: enhanced potency and selective delivery for breast cancer treatment." *Bioconjugate chemistry* 20, no. 12 (2009): 2247-2253.

62. Maeda, Hiroshi. "The enhanced permeability and retention (EPR) effect in tumor vasculature: the key role of tumor-selective macromolecular drug targeting." *Advances in enzyme regulation* 41 (2001): 189-207.

63. Dickerson, Erin B., Erik C. Dreaden, Xiaohua Huang, Ivan H. El-Sayed, Hunghao Chu, Sujatha Pushpanketh, John F. McDonald, and Mostafa A. El-Sayed. "Gold nanorod assisted near-infrared plasmonic photothermal therapy (PPTT) of squamous cell carcinoma in mice." *Cancer letters* 269, no. 1 (2008): 57-66.

64. Hainfeld, J. F., D. N. Slatkin, T. M. Focella, and H. M. Smilowitz. "Gold nanoparticles: a new X-ray contrast agent." *The British journal of radiology* 79, no. 939 (2006): 248-253.

65. Elghanian, Robert, James J. Storhoff, Robert C. Mucic, Robert L. Letsinger, and Chad A. Mirkin. "Selective colorimetric detection of polynucleotides based on the distance-dependent optical properties of gold nanoparticles." *Science* 277, no. 5329 (1997): 1078-1081.

66. Letsinger, R. L., R. Elghanian, G. Viswanadham, and C. A. Mirkin. "Use of a steroid cyclic disulfide anchor in constructing gold nanoparticle− oligonucleotide conjugates." *Bioconjugate chemistry* 11, no. 2 (2000): 289-291.

67. Ghosh, Partha S., Chae-Kyu Kim, Gang Han, Neil S. Forbes, and Vincent M. Rotello. "Efficient gene delivery vectors by tuning the surface charge density of amino acid-functionalized gold nanoparticles." *ACS nano* 2, no. 11 (2008): 2213-2218.

68. Rayavarapu, Raja Gopal, Wilma Petersen, Constantin Ungureanu, Janine N. Post, Ton G. van Leeuwen, and Srirang Manohar. "Synthesis and bioconjugation of gold nanoparticles as potential molecular probes for light-based imaging techniques." *International Journal of biomedical imaging* (2007).

69. Kumar, S., J. Aaron, and K. Sokolov. "Directional conjugation of antibodies to nanoparticles for synthesis of multiplexed optical contrast agents with both delivery and targeting moieties." *Nature protocols* 3, no. 2 (2008): 314-320.

70. Yu, Mi Kyung, Jinho Park, and Sangyong Jon. "Targeting strategies for multifunctional nanoparticles in cancer imaging and therapy." *Theranostics* 2, no. 1 (2012): 3.

71. Jazayeri, Mir Hadi, Hamed Amani, Ali Akbar Pourfatollah, Hamidreza Pazoki-Toroudi, and Bijan Sedighimoghaddam. "Various methods of gold nanoparticles (GNPs) conjugation to antibodies." *Sensing and bio-sensing research* 9 (2016): 17-22.

72. Sperling, Reisa A., and Wolfgang J. Parak. "Surface modification, functionalization and bioconjugation of colloidal inorganic nanoparticles." *Philosophical Transactions of the Royal Society A: Mathematical, Physical and Engineering Sciences* 368, no. 1915 (2010): 1333-1383.

73. Flora, S. J. "Lead exposure: health effects, prevention and treatment." *Journal of environmental biology* 23, no. 1 (2002): 25-41.

74. Liu, Juewen, and Yi Lu. "A colorimetric lead biosensor using DNAzyme-directed assembly of gold nanoparticles." *Journal of the American Chemical Society* 125, no. 22 (2003): 6642-6643.

75. Obare, Sherine O., Rachel E. Hollowell, and Catherine J. Murphy. "Sensing strategy for lithium ion based on gold nanoparticles." *Langmuir* 18, no. 26 (2002): 10407-10410.

76. Li, Huixiang, and Lewis J. Rothberg. "Label-free colorimetric detection of specific sequences in genomic DNA amplified by the polymerase chain reaction." *Journal of the American Chemical Society* 126, no. 35 (2004): 10958-10961.

77. He, Lin, Michael D. Musick, Sheila R. Nicewarner, Frank G. Salinas, Stephen J. Benkovic, Michael J. Natan, and Christine D. Keating. "Colloidal Au-enhanced surface plasmon resonance for ultrasensitive detection of DNA hybridization." *Journal of the American Chemical Society* 122, no. 38 (2000): 9071-9077.

78. Maxwell, Dustin J., Jason R. Taylor, and Shuming Nie. "Self-assembled nanoparticle probes for recognition and detection of biomolecules." *Journal of the American Chemical Society* 124, no. 32 (2002): 9606-9612.

79. Cao, Y. Charles, Rongchao Jin, Jwa-Min Nam, C. Shad Thaxton, and Chad A. Mirkin. "Raman dye-labeled nanoparticle probes for proteins." *Journal of the American Chemical Society* 125, no. 48 (2003): 14676-14677.

80. Shin, Min Hwa, Wonjin Hong, Youngjo Sa, Lei Chen, Yu-Jin Jung, Xu Wang, Bing Zhao, and Young Mee Jung. "Multiple detection of proteins by SERS-based

immunoassay with core shell magnetic gold nanoparticles." *Vibrational Spectroscopy* 72 (2014): 44-49.

81. Chen, Sz-Hau, Yao-Chen Chuang, Yi-Chen Lu, Hsiu-Chao Lin, Yun-Liang Yang, and Chih-Sheng Lin. "A method of layer-by-layer gold nanoparticle hybridization in a quartz crystal microbalance DNA sensing system used to detect dengue virus." *Nanotechnology* 20, no. 21 (2009): 215501.
82. Lee, Ki-Bum, Eun-Young Kim, Chad A. Mirkin, and Steven M. Wolinsky. "The use of nanoarrays for highly sensitive and selective detection of human immunodeficiency virus type 1 in plasma." *Nano Letters* 4, no. 10 (2004): 1869-1872.
83. Bhana S., Wang Y., Huang X. Nanotechnology for enrichment and detection of circulating tumor cells. *Nanomedicine* 10(12), 1973-1990 (2015).
84. Hüsemann Y., Geigl J.B., Schubert F. et al. Systemic spread is an early step in breast cancer. *Cancer Cell* 13(1), 58-68 (2008).
85. Danila D.C., Fleisher M., Scher H.I. Circulating tumor cells as biomarkers in prostate cancer. *Clin. Cancer Res.* 17(12), 3903-3912 (2011).
86. Bhana, S., E. Chaffin, Y. Wang, S.R. Mishra, X. Huang, Capture and detection of cancer cells in whole blood with magnetic-optical nanoovals. *Nanomedicine(Lond)*, 2013. 9(5): p. 593-606.
87. Siegel, R.; Ma, J.; Zou, Z.; Jemal, A. Cancer Statistics 2014. *Ca -Cancer J. Clin.* 2014, 64, 9−29.
88. Geiger, T. R.; Peeper, D. S. Metastasis Mechanisms. *Biochim. Biophys. Acta* 2009, 1796, 293−308.

89. Maheswaran, S.; Haber, D. A. Circulating Tumor Cells: a Window into Cancer Biology and Metastasis. *Curr. Opin. Genet. Dev.* 2010, 20, 96−99.

90. Plaks, V.; Koopman, C. D.; Werb, Z. Circulating Tumor Cells. *Science* 2013, 341, 1186−1188.

91. Fares, J.; Fares, M. Y.; Khachfe, H. H.; Salhab, H. A.; Fares, Y. Molecular Principles of Metastasis: a Hallmark of Cancer Revisited. *Signal Transduction Targeted Ther.* 2020, 5, 28.

92. Paterlini-Brechot, P.; Benali, N. L. Circulating Tumor Cells (CTC) Detection: Clinical Impact and Future Directions. *Canc. Lett.* 2007, 253, 180−204.

93. Budd, G. T. Let Me Do More Than Count The Ways: What Circulating Tumor Cells Can Tell Us About The Biology of Cancer. *Mol. Pharm.* 2009, 6, 1307−1310.

94. Balic, M.; Williams, A.; Lin, H.; Datar, R.; Cote, R. J. Circulating Tumor Cells: from Bench to Bedside. *Annu. Rev.* Med. 2013, 64, 31− 44.

95. Bidard, F.-C.; Fehm, T.; Ignatiadis, M.; Smerage, J. B.; AlixPanabieres, C.; Janni, W.; Messina, C.; Paoletti, C.; Mu ̀ller, V.; Hayes, D. F.; Piccart, M.; Pierga, J.-Y. Clinical Application Of Circulating Tumor Cells in Breast Cancer: Overview of The Current Interventional Trials. *Canc. Metastasis Rev.* 2013, 32, 179−188.

96. Rawal, S.; Yang, Y.-P.; Cote, R.; Agarwal, A. Identification and Quantitation of Circulating Tumor Cells. *Annu. Rev. Anal. Chem.* 2017, 10, 321−343.

97. Banko, P.; Lee, S. Y.; Nagygyo ́rgy, V.; Zrínyi, M.; Chae, C. H.; Cho, D. H.; Telekes, A. Technologies for Circulating Tumor Cell Separation from Whole Blood. *J. Hematol. Oncol.* 2019, 12, 48.

98. Alix-Panabieres, C. EPISPOT Assay: Detection of Viable` DTCs/CTCs in Solid Tumor Patients. *Recent Results Canc. Res.* 2012, 195, 69−76.

99. Riethdorf, S.; Fritsche, H.; Muller, V.; Rau, T.; Schindlbeck, C.; Rack, B.; Janni, W.; Coith, C.; Beck, K.; Janicke, F.; Jackson, S.; Gornet, T.; Cristofanilli, M.; Pantel, K. Detection of Circulating Tumor Cells in Peripheral Blood of Patients with Metastatic Breast Cancer: A Validation Study of The Cellsearch System. *Clin. Cancer Res.* 2007, 13, 920−928.

100. Danila, D. C.; Samoila, A.; Patel, C.; Schreiber, N.; Herkal, A.; Anand, A.; Bastos, D.; Heller, G.; Fleisher, M.; Scher, H. I. Clinical Validity of Detecting Circulating Tumor Cells by Adnatest Assay Compared to Direct Detection of Tumor Mrna in Stabilized Whole Blood, as a Biomarker Predicting Overall Survival for Metastatic Castration-Resistant Prostate Cancer Patients. *Cancer J.* 2016, 22, 315−320.

101. Miller, M. C.; Doyle, G. V.; Terstappen, L. W. M. M. Significance of Circulating Tumor Cells Detected by The Cellsearch Systemin Patients with Metastatic Breast Colorectal and Prostate Cancer. *J. Oncol.* 2010, 2010, 617421.

102. Danova, M.; Torchio, M.; Mazzini, G. Isolation of Rare Circulating Tumor Cells in Cancer Patients: Technical Aspects and Clinical Implications. *Expert Rev. Mol. Diagn* 2011, 11, 473−485.

103. Uhr, J. W.; Huebschman, M. L.; Frenkel, E. P.; Lane, N. L.; Ashfaq, R.; Liu, H.; Rana, D. R.; Cheng, L.; Lin, A. T.; Hughes, G. A.; Zhang, X. J.; Garner, H. R. Molecular Profiling of Individual Tumor Cells by Hyperspectral Microscopic Imaging. *Transl. Res.* 2012, 159, 366−375.

104. Zhao, M.; Wei, B.; Chiu, D. T. Imaging Multiple Biomarkers in Captured Rare Cells by Sequential Immunostaining and Photobleaching. *Method* 2013, 64, 108−113.

105. Park, S.-m.; Wong, D. J.; Ooi, C. C.; Kurtz, D. M.; Vermesh, O.; Aalipour, A.; Suh, S.; Pian, K. L.; Chabon, J. J.; Lee, S. H.; Jamali, M.; Say, C.; Carter, J. N.; Lee, L. P.; Kuschner, W. G.; Schwartz, E. J.; Shrager, J. B.; Neal, J. W.; Wakelee, H. A.; Diehn, M.; Nair, V. S.; Wang, S. X.; Gambhir, S. S. Molecular Profiling of Single Circulating Tumor Cells from Lung Cancer Patients. *Proc. Natl. Acad. Sci. U.S.A.* 2016, 113, E8379−E8386.

106. Katz, R. L.; Zaidi, T. M.; Pujara, D.; Shanbhag, N. D.; Truong, D.; Patil, S.; Mehran, R. J.; El-Zein, R. A.; Shete, S. S.; Kuban, J. D. Identification of Circulating Tumor Cells Using 4-Color Fluorescence In Situ Hybridization: Validation of a Noninvasive Aid for Ruling Out Lung Cancer in Patients with Low-Dose Computed Tomography− Detected Lung Nodules. Cancer *Cytopathol.* 2020, 128, 553−562.

107. Nima, Z. A.; Mahmood, M.; Xu, Y.; Mustafa, T.; Watanabe, F.; Nedosekin, D. A.; Juratli, M. A.; Fahmi, T.; Galanzha, E. I.; Nolan, J. P.; Basnakian, A. G.; Zharov, V. P.; Biris, A. S. Circulating Tumor Cell Identification by Functionalized Silver-Gold Nanorods with Multicolor, Super-Enhanced SERS and Photothermal Resonances. *Sci. Rep.* 2014, 4, 4752.

108. Galanzha, E. I.; Shashkov, E. V.; Kelly, T.; Kim, J.-W.; Yang, L.; Zharov, V. P. In Vivo Magnetic Enrichment and Multiplex Photoacoustic Detection of Circulating Tumour Cells. *Nat. Nanotechnol.* 2009, 4, 855−860.

109. Pamme, N. Magnetism and Microfluidics. *Lab Chip* 2006, 6, 24−38.

110. Pratt, E. D.; Huang, C.; Hawkins, B. G.; Gleghorn, J. P.; Kirby, B. J. Rare Cell Capture in Microfluidic Devices. *Chem. Eng. Sci.* 2011, 66, 1508−1522.

111. Rivet, C.; Lee, H.; Hirsch, A.; Hamilton, S.; Lu, H. Microfluidics for Medical Diagnostics and Biosensors. *Chem. Eng. Sci.* 2011, 66, 1490−1507.

112. Autebert, J.; Coudert, B.; Bidard, F.-C.; Pierga, J.-Y.; Descroix, S.; Malaquin, L.; Viovy, J.-L. Microfluidic: an Innovative Tool for Efficient Cell Sorting. *Methods* 2012, 57, 297−307.

113. Xia, N.; Hunt, T. P.; Mayers, B. T.; Alsberg, E.; Whitesides, G. M.; Westervelt, R. M.; Ingber, D. E. Combined Microfluidic Micromagnetic Separation of Living Cells in Continuous Flow. *Biomed. Microdevices* 2006, 8, 299−308.

114. Adams, J. D.; Thevoz, P.; Bruus, H.; Soh, H. T. Integrated´ Acoustic and Magnetic Separation in Microfluidic Channels. *Appl. Phys. Lett.* 2009, 95, 254103.

115. Modak, N.; Datta, A.; Ganguly, R. Cell Separation in a Microfluidic Channel Using Magnetic Microospheres. Microfluid. *Nanofluidics* 2009, 6, 647−660.

116. Hoshino, K.; Huang, Y.-Y.; Lane, N.; Huebschman, M.; Uhr, J. W.; Frenkel, E. P.; Zhang, X. Microchip-Based Immunomagnetic Detection of Circulating Tumor Cells. *Lab Chip* 2011, 11, 3449− 3457.

117. Hoshino, K.; Chen, P.; Huang, Y.-Y.; Zhang, X. Computational Analysis of Microfluidic Immunomagnetic Rare Cell Separation from a Particulate Blood Flow. *Anal. Chem.* 2012, 84, 4292−4299.

118. Wu, C.-H.; Huang, Y.-Y.; Chen, P.; Hoshino, K.; Liu, H.; Frenkel, E. P.; Zhang, J. X. J.; Sokolov, K. V. Versatile Immunomagnetic Nanocarrier Platform for Capturing Cancer Cells. *ACS Nano* 2013, 7, 8816−8823.

119. Sheridan, C.; Kishimoto, H.; Fuchs, R. K.; Mehrotra, S.; BhatNakshatri, P.; Turner, C. H.; Goulet, R., Jr; Badve, S.; Nakshatri, H. CD44+/CD24-Breast Cancer Cells Exhibit

Enhanced Invasive Properties: an Early Step Necessary for Metastasis. *Breast Canc. Res.* 2006, 8, R59.

120. Subik, K.; Lee, J. F.; Baxter, L.; Strzepek, T.; Costello, D.; Crowley, P.; Xing, L.; Hung, M. C.; Bonfiglio, T.; Hicks, D. G.; Tang, P. The Expression Patterns of ER, PR, HER2, CK5/6, EGFR, Ki-67 and AR by Immunohistochemical Analysis in Breast Cancer Cell Lines. *Breast Canc.* 2010, 4, 35−41.

121. Soysal, S. D.; Muenst, S.; Barbie, T.; Fleming, T.; Gao, F.; Spizzo, G.; Oertli, D.; Viehl, C. T.; Obermann, E. C.; Gillanders, W. E. Epcam Expression Varies Significantly and Is Differentially Associated with Prognosis in The Luminal B HER2ρ, Basal-Like, and HER2 Intrinsic Subtypes of Breast Cancer. *Br. J. Canc.* 2013, 108, 1480−1487.

122. Burstein, H. J. The Distinctive Nature Of HER2-Positive Breast Cancers. *N. Engl. J. Med.* 2005, 353, 1652−1654.

123. Naab, T.; Ricks-Santi, L.; Khan, F. CD44 Expression Associated with Triple Negative Breast Cancers in African American Women without Unfavorable Outcome. *Am. J. Clin. Pathol.* 2016, 146, 295.

124. Arcaro, A. Targeting the Insulin-Like Growth Factor-1 Receptor in Human Cancer. *Front. Pharmacol.* 2013, 4, 30.

125. Kucab, J. E.; Dunn, S. E. Role of IGF-1R in Mediating Breast Cancer Invasion and Metastasis. *Breast Dis.* 2003, 17, 41−47.

126. de Bono, J. S.; Attard, G.; Adjei, A.; Pollak, M. N.; Fong, P. C.; Haluska, P.; Roberts, L.; Melvin, C.; Repollet, M.; Chianese, D.; Connely, M.; Terstappen, L. W. M. M.; Gualberto, A. Potential Applications for Circulating Tumor Cells Expressing the Insulin-Like Growth Factor-I Receptor. *Clin. Cancer Res.* 2007, 13, 3611−3616.

127. Zavaleta, C. L.; Smith, B. R.; Walton, I.; Doering, W.; Davis, G.; Shojaei, B.; Natan, M. J.; Gambhir, S. S. Multiplexed Imaging of Surface Enhanced Raman Scattering Nanotags in Living Mice Using Noninvasive Raman Spectroscopy. *Proc. Natl. Acad. Sci. U.S.A.* 2009, 106, 13511−13516.

128. Link, S., M. A. El-Sayed, Optical properties and ultrafast dynamics of metallic nanocrystals. *Ann. Rev. Phys. Chem.*, 2003. 54: p. 331-366.

129. Jain, P.K., X. Huang, I. H. El-Sayed, M. A. El-Sayed, Review of some surface plasmon resonance-enhanced properties of noble metal nanoparticles and their applications to biosystems. *Plasmonics*, 2007. 2: p. 107-118.

130. Huang, X.H., P. Jain, I. H. El-Sayed, M. A. El-Sayed, Gold nanoparticles: interesting optical properties and recent applications in cancer diagnostics and therapy. *Nanomedicine (Lond.)*, 2007. 2(5): p. 681-693.

131. Lee, S.K., M. A. El-Sayed, Gold and silver nanoparticles in sensing and imaging: sensitivity of plasmon response to size, shape, and metal composition. *J. Phys. Chem. B*, 2006. 110: p. 19220.

132. Yguerabide, J., Yguerabide EE, Light-scattering submicroscopic particles as highly fluorescent analogs and their use as tracer labels in clinical and biological applications. *I. Theory. Anal. Biochem.*, 1998. 262: p. 137-156.

133. Link, S., El-Sayed, M. A., Shape and size dependence of radiative, non-radiative and photothermal properties of gold nanocrystals. *Int. Rev. Phys. Chem.* , 2000. 19(3): p. 409-453.

134. Jain, P.K., X. Huang, I.H. El-Sayed, M.A. El-Sayed, Noble metals on the nanoscale: optical and photothermal properties and applications in imaging, sensing, biology, and medicine. *Acc. Chem. Res.*, 2008. 41: p. 1578-1586.

135. Huang, X., P. K. Jain, I. H. El-Sayed, M.A. El-Sayed, Plasmonic photothermal therapy (PPTT) using gold nanoparticles. *Lasers Med. Sci.*, 2008. 23(9): p. 217-228.

136. Huang, X., M.A. El-Sayed, Gold nanoparticles: optical properties and implementations in cancer diagnosis and photothermal therapy. *J. Adv. Res.*, 2010. 1: p. 13-28.

137. Dreaden, E.C., M.A. Mackey, X. Huang, B. Kangy, M.A. El-Sayed, Beating cancer in multiple ways using nanogold. *Chem. Soc. Rev.*, 2011. 40: p. 3391–3404.

138. Lee, K.S., M.A. El-Sayed., Dependence of the enhanced optical scattering efficiency relative to that of absorption for gold metal nanorods on aspect ratio, size, end-cap shape, and medium refractive Index. *J. Phys. Chem.* B 2005. 109(43): p. 20331.

139. El-Sayed, I.H., X. Huang, M.A. El-Sayed, Surface plasmon resonance scattering and absorption of anti-EGFR antibody conjugated gold nanoparticles in cancer diagnostics: applications in oral cancer. *Nano lett.*, 2005. 5(5): p. 829-834.

140. Chan, Jasper Fuk-Woo, Shuofeng Yuan, Kin-Hang Kok, Kelvin Kai-Wang To, Hin Chu, Jin Yang, Fanfan Xing et al. "A familial cluster of pneumonia associated with the 2019 novel coronavirus indicating person-to-person transmission: a study of a family cluster." *The lancet* 395, no. 10223 (2020): 514-523.

141. Huang, Chaolin, Yeming Wang, Xingwang Li, Lili Ren, Jianping Zhao, Yi Hu, Li Zhang et al. "Clinical features of patients infected with 2019 novel coronavirus in Wuhan, China." *The lancet* 395, no. 10223 (2020): 497-506.

142. Zhu, Na, Dingyu Zhang, Wenling Wang, Xingwang Li, Bo Yang, Jingdong Song, Xiang Zhao et al. "A novel coronavirus from patients with pneumonia in China, 2019." *New England journal of medicine* (2020).

143. Johns Hopkins Coronavirus Resource Center. Accessed October 9, 2021. https://coronavirus.jhu.edu/map.html.

144. Malik, Yasmin A. "Properties of coronavirus and SARS-CoV-2." *The Malaysian journal of pathology* 42, no. 1 (2020): 3-11.

145. Li, Fang. "Structure, function, and evolution of coronavirus spike proteins." *Annual review of virology* 3 (2016): 237-261.

146. Li, Wenhui, Michael J. Moore, Natalya Vasilieva, Jianhua Sui, Swee Kee Wong, Michael A. Berne, Mohan Somasundaran et al. "Angiotensin-converting enzyme 2 is a functional receptor for the SARS coronavirus." *Nature* 426, no. 6965 (2003): 450-454.

147. Woo, Patrick CY, Susanna KP Lau, Beatrice HL Wong, Hoi-wah Tsoi, Ami MY Fung, Richard YT Kao, Kwok-hung Chan, JS Malik Peiris, and Kwok-yung Yuen. "Differential sensitivities of severe acute respiratory syndrome (SARS) coronavirus spike polypeptide enzyme-linked immunosorbent assay (ELISA) and SARS coronavirus nucleocapsid protein ELISA for serodiagnosis of SARS coronavirus pneumonia." *Journal of clinical microbiology* 43, no. 7 (2005): 3054-3058.

148. Zhou, Peng, Xing-Lou Yang, Xian-Guang Wang, Ben Hu, Lei Zhang, Wei Zhang, Hao-Rui Si et al. "A pneumonia outbreak associated with a new coronavirus of probable bat origin." *nature* 579, no. 7798 (2020): 270-273.

149. General Office of National Health Committee, State Administration of Traditional Chinese Medicine. "Notice on the issuance of strategic guidelines for diagnosis and treatment of novel coronavirus (2019-nCoV) infected pneumonia (draft)." (2020).

150. Liu, Wanbing, Lei Liu, Guomei Kou, Yaqiong Zheng, Yinjuan Ding, Wenxu Ni, Qiongshu Wang et al. "Evaluation of nucleocapsid and spike protein-based enzyme-linked immunosorbent assays for detecting antibodies against SARS-CoV-2." *Journal of clinical microbiology* 58, no. 6 (2020): e00461-20.

151. Nguyen, Ngoc Hoang Lan, Sungjoon Kim, Garrett Lindemann, and Vikas Berry. "COVID-19 Spike Protein Induced Phononic Modification in Antibody-Coupled Graphene for Viral Detection Application." *ACS nano* (2021).

152. Paiva, Kimberly J., Ricky D. Grisson, Philip A. Chan, Richard C. Huard, Angela M. Caliendo, John R. Lonks, Ewa King et al. "Validation and performance comparison of three SARS-CoV-2 antibody assays." *Journal of medical virology* 93, no. 2 (2021): 916-923.

153. Ebinger, Joseph E., Justyna Fert-Bober, Ignat Printsev, Min Wu, Nancy Sun, John C. Prostko, Edwin C. Frias et al. "Antibody responses to the BNT162b2 mRNA vaccine in individuals previously infected with SARS-CoV-2." *Nature Medicine* 27, no. 6 (2021): 981-984.

154. Jabal, Kamal Abu, Hila Ben-Amram, Karine Beiruti, Yunis Batheesh, Christian Sussan, Salman Zarka, and Michael Edelstein. "Impact of age, ethnicity, sex and prior infection status on immunogenicity following a single dose of the BNT162b2 mRNA COVID-19 vaccine: real-world evidence from healthcare workers, Israel, December 2020 to January 2021." *Eurosurveillance* 26, no. 6 (2021): 2100096.

155. Zhang, Wei, Rong-Hui Du, Bei Li, Xiao-Shuang Zheng, Xing-Lou Yang, Ben Hu, Yan-Yi Wang et al. "Molecular and serological investigation of 2019-nCoV infected patients: implication of multiple shedding routes." *Emerging microbes & infections* 9, no. 1 (2020): 386-389.

156. Liu, Xuemei, Jing Wang, Xiaolei Xu, Guojian Liao, Yaokai Chen, and Chang-Hua Hu. "Patterns of IgG and IgM antibody response in COVID-19 patients." *Emerging microbes & infections* 9, no. 1 (2020): 1269-1274.

157. Li, Gang, Xuejuan Chen, and Anlong Xu. "Profile of specific antibodies to the SARS-associated coronavirus." *New England Journal of Medicine* 349, no. 5 (2003): 508-509.

158. Greenberger, Lee M., Larry A. Saltzman, Jonathon W. Senefeld, Patrick W. Johnson, Louis J. DeGennaro, and Gwen L. Nichols. "Antibody response to SARS-CoV-2 vaccines in patients with hematologic malignancies." *Cancer Cell* 39, no. 8 (2021): 1031-1033.

159. Van Oekelen, Oliver, Charles R. Gleason, Sarita Agte, Komal Srivastava, Katherine F. Beach, Adolfo Aleman, Katerina Kappes et al. "Highly variable SARS-CoV-2 spike antibody responses to two doses of COVID-19 RNA vaccination in patients with multiple myeloma." *Cancer Cell* 39, no. 8 (2021): 1028-1030.

160. Franek, Milan, Vladimir Kolar, Anping Deng, and Steven Crooks. "Determination of sulphadimidine (sulfamethazine) residues in milk, plasma, urine and edible tissues by sensitive ELISA." *Food and Agricultural Immunology* 11, no. 4 (1999): 339-349.

161. Jia, Chun-Ping, Xiao-Qin Zhong, Bao Hua, Mei-Ying Liu, Feng-Xiang Jing, Xin-Hui Lou, Shi-Hua Yao, Jia-Qing Xiang, Qing-Hui Jin, and Jian-Long Zhao. "Nano-ELISA for

highly sensitive protein detection." *Biosensors and Bioelectronics* 24, no. 9 (2009): 2836-2841.

162. Liu, Dingbin, Jie Yang, He-Fang Wang, Zhongliang Wang, Xinglu Huang, Zhantong Wang, Gang Niu, A. R. Hight Walker, and Xiaoyuan Chen. "Glucose oxidase-catalyzed growth of gold nanoparticles enables quantitative detection of attomolar cancer biomarkers." *Analytical chemistry* 86, no. 12 (2014): 5800-5806.

163. Ambrosi, Adriano, Federico Airo, and Arben Merkoci. "Enhanced gold nanoparticle based ELISA for a breast cancer biomarker." *Analytical chemistry* 82, no. 3 (2010): 1151-1156.

164. Chen, Si, Mikael Svedendahl, Richard P. Van Duyne, and Mikael Käll. "Plasmon-enhanced colorimetric ELISA with single molecule sensitivity." *Nano Letters* 11, no. 4 (2011): 1826-1830.

165. Kamaraj, G., M. Lakshmi Narasu, and V. A. Srinivasan. "Validation of betapropiolactone (BPL) as an inactivant for infectious bovine rhinotracheitis (IBR) virus." *Research in veterinary science* 85, no. 3 (2008): 589-594.

166. Möller, Lars, Livia Schünadel, Andreas Nitsche, Ingeborg Schwebke, Manuela Hanisch, and Michael Laue. "Evaluation of virus inactivation by formaldehyde to enhance biosafety of diagnostic electron microscopy." *Viruses* 7, no. 2 (2015): 666-679.

167. Smith, Donald D., Christopher B. Cohick, and Herbert B. Lindsley. "Optimization of cellular ELISA for assay of surface antigens on human synoviocytes." *BioTechniques* 22, no. 5 (1997): 952-957.

168. Austin, Lauren A., Megan A. Mackey, Erik C. Dreaden, and Mostafa A. El-Sayed. "The optical, photothermal, and facile surface chemical properties of gold and silver

nanoparticles in biodiagnostics, therapy, and drug delivery." *Archives of toxicology* 88, no. 7 (2014): 1391-1417.

APPENDIX A

Table S1. Determination of the number of proteins per IO-Au NPC with Micro BCA protein assay.

Amount IgG added to conjugation (ug)	**Amount bound (ug)**	**Ab/NPC**
5	1.4	4.7
10	9.44	31.8
20	14.21	47.4

Table S2. Examination of the accuracy of multicolor IO-Au SERS nanotags with CLS regression for multiplexed detection.

Mixed Ratio of QSY21:BHQ3: QXL680:IR740	**Experimental**	**Expected**	**δ**	**% Accuracy**
1111	0.236502948	0.25	5.398820723	94.60117928
	0.26588259	0.25	6.353035851	93.64696415
	0.257546386	0.25	3.01855457	96.98144543
	0.247482829	0.25	1.006868461	98.99313154
2111	0.400094125	0.4	0.023531217	99.97646878
	0.185291997	0.2	7.354001352	92.64599865
	0.212525256	0.2	6.262628225	93.73737178
	0.20075023	0.2	0.375115209	99.62488479
1311	0.163686839	0.166666667	1.787896342	98.21210366
	0.490893207	0.5	1.821358626	98.17864137
	0.1846922	0.166666667	10.81532013	89.18467987
	0.178730002	0.166666667	7.238001449	92.76199855
1141	0.154900746	0.142857143	8.430521942	91.56947806
	0.131196028	0.142857143	8.162780345	91.83721966
	0.588325069	0.571428571	2.956887146	97.04311285
	0.157753279	0.142857143	10.42729543	89.57270457
1115	0.137975157	0.125	10.3801257	89.6198743
	0.116596447	0.125	6.722842056	93.27715794
	0.121817743	0.125	2.545805284	97.45419472
	0.619511494	0.625	0.878160947	99.12183905
2345	0.139289609	0.142857143	2.497273372	97.50272663
	0.216368292	0.214285714	0.971869436	99.02813056
	0.282536933	0.285714286	1.112073281	98.88792672
	0.359550751	0.357142857	0.674210415	99.32578959

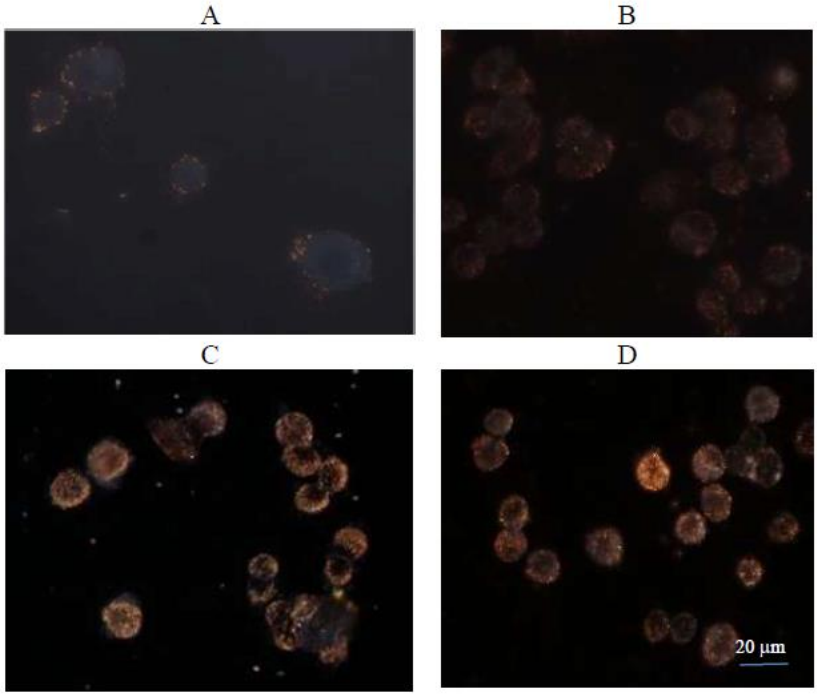

Figure S1. Dark field images of SK-BR-3 cells after incubation with IO-Au core-shell NPCs with different amount of loading antibody. (A) to (D) is 2.5, 5, 10, and 20 uL of 1 mg/mL antibody, respectively, to 0.25 mL of 1 nM IO-Au SERS NPCs.

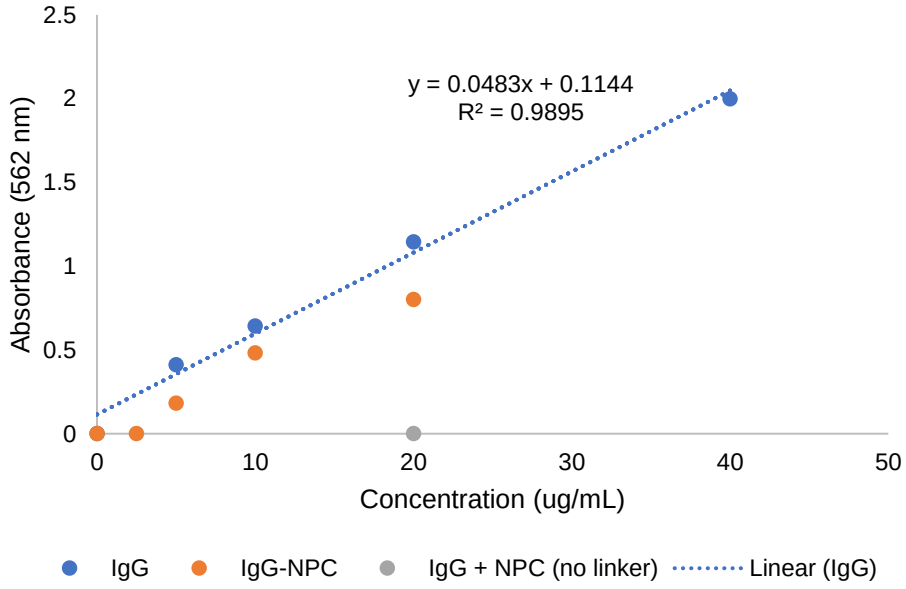

Figure S2. Characterization of the bound proteins on IO-Au NPCs by measuring absorbance at 562 nm in the Micro BCA protein assay. IgG was used as the protein model.

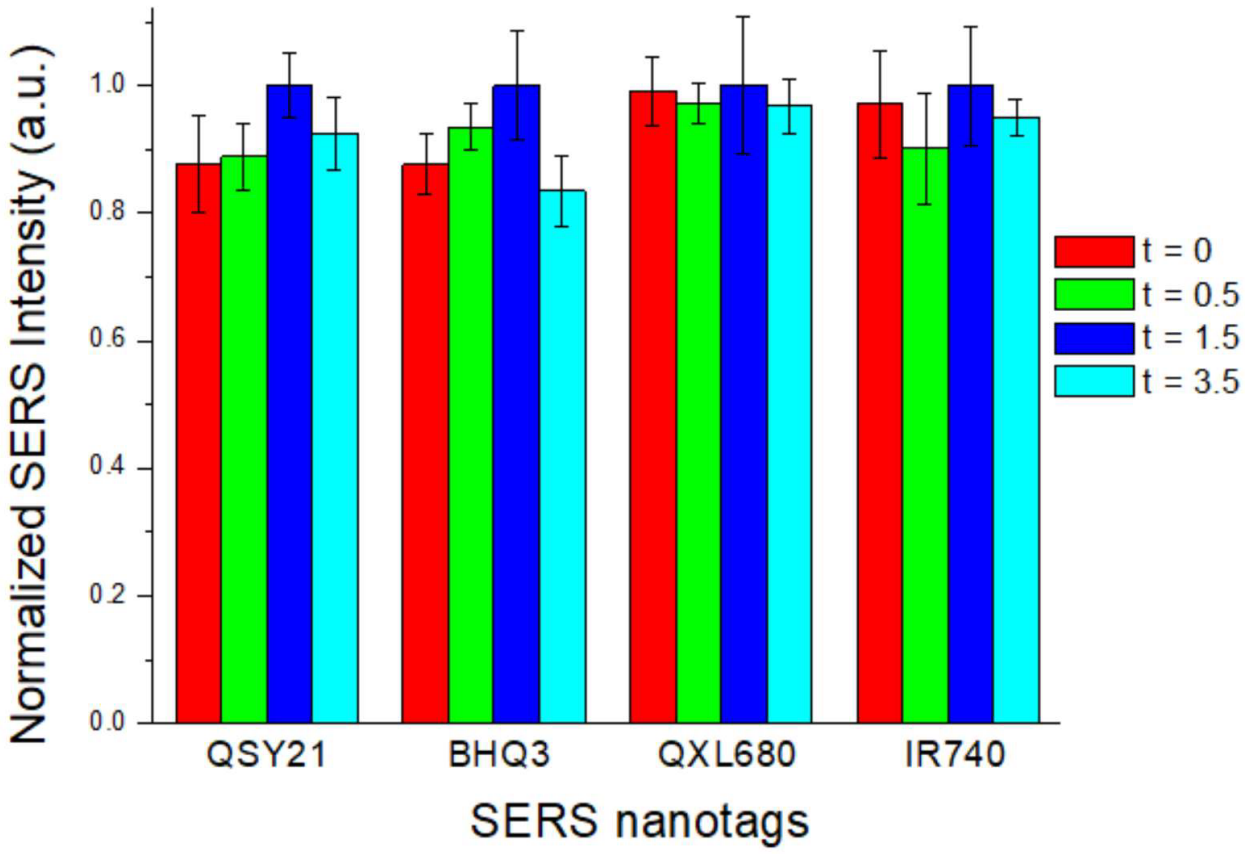

Figure S3. Examination of the stability of SERS nanotags in blood. SERS signal intensities were measured at 1497 cm^{-1} for QSY21, 1092 cm^{-1} for BHQ3, 1139 cm^{-1} for QXL680, and 501 cm^{-1} for IR740. They were normalized to the highest intensity among the groups for each nanotag.

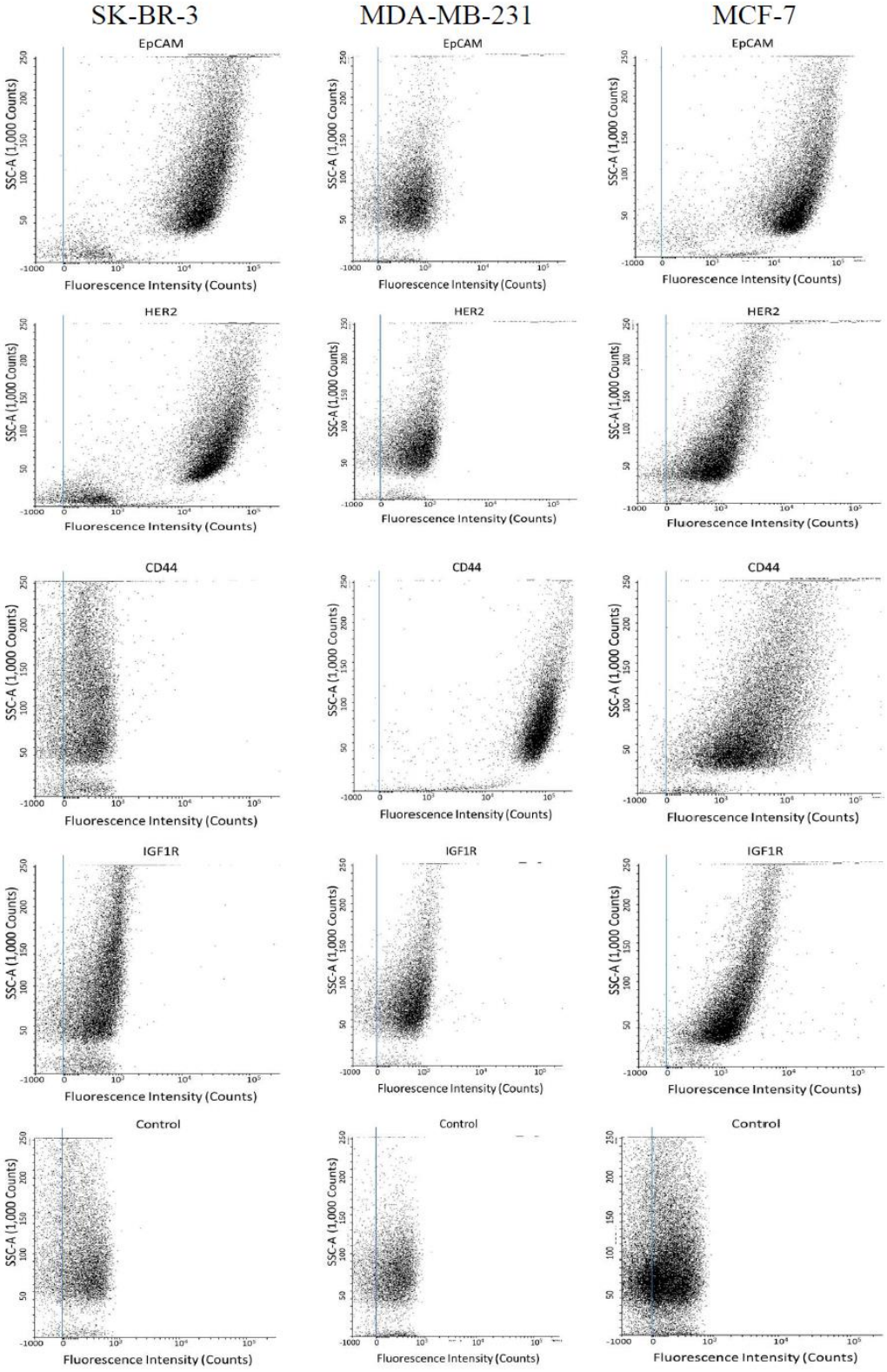

Figure S4. Characterization of EpCAM, HER2, CD44, and IGF1R expressions on SK-BR-3, MDA-MB-231, and MCF-7 cells with flow cytometry.

A

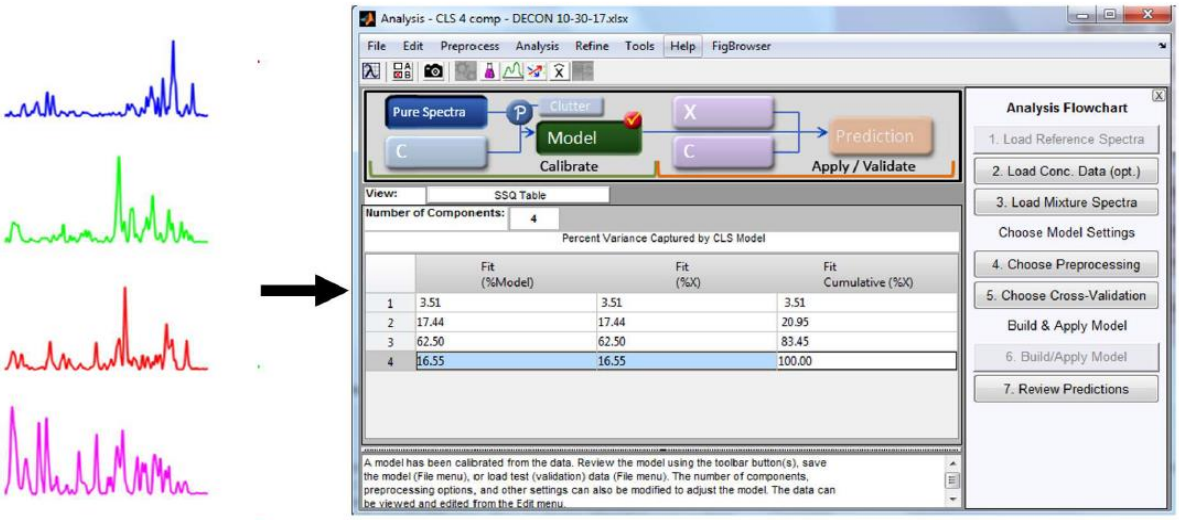

B

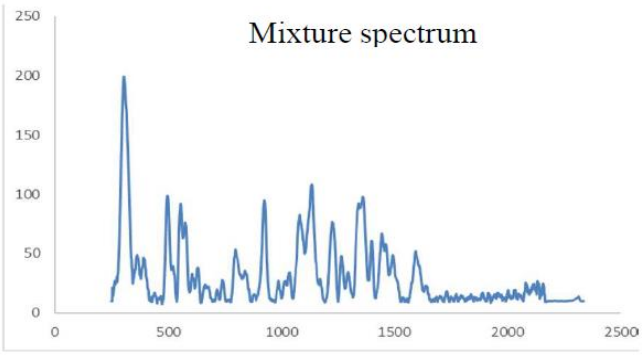

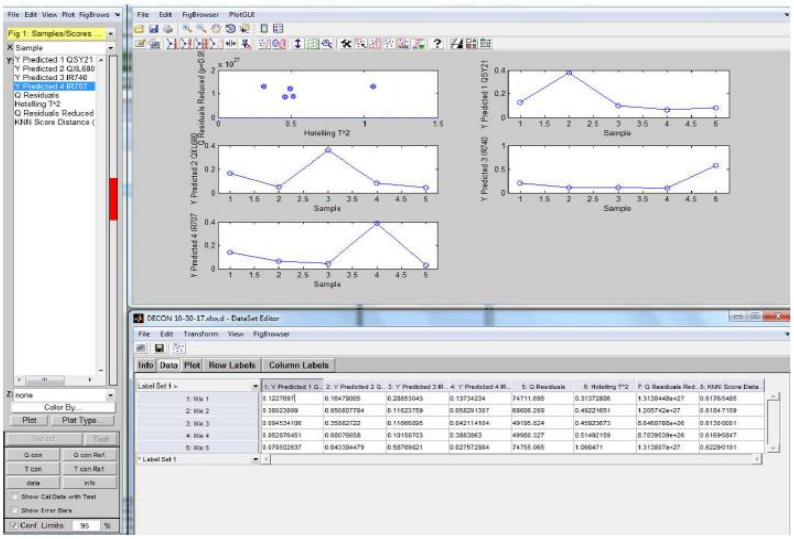

Figure S5. Signal deconvolution with CLS regression. (A) The CLS module showing the step of loading the reference spectra of the 4 color SERS nanotags. (B) The CLS module showing the step of signal deconvolution of each nanotag from the mixed SERS spectrum.